

***Sister Rod
Nondestructive
Examination
Annual Report FY2017***

Spent Fuel and Waste Disposition

***Prepared for
US Department of Energy
Spent Fuel and Waste Science and
Technology***

***Oak Ridge National Laboratory:
Rose Montgomery, Bruce Bevard,
Robert N. Morris, James Goddard, Jr.,
Susan K. Smith, Jianwei Hu***

***Electric Power Research Institute:
John Beale and Byungsik Yoon***

***September 15, 2017
SFWD-SFWST-2017-000003
ORNL/SPR-2017/484***

DISCLAIMER

This information was prepared as an account of work sponsored by an agency of the U.S. Government. Neither the U.S. Government nor any agency thereof, nor any of their employees, makes any warranty, expressed or implied, or assumes any legal liability or responsibility for the accuracy, completeness, or usefulness, of any information, apparatus, product, or process disclosed, or represents that its use would not infringe privately owned rights. References herein to any specific commercial product, process, or service by trade name, trade mark, manufacturer, or otherwise, does not necessarily constitute or imply its endorsement, recommendation, or favoring by the U.S. Government or any agency thereof. The views and opinions of authors expressed herein do not necessarily state or reflect those of the U.S. Government or any agency thereof.

SUMMARY

This report documents work performed under the Spent Fuel and Waste Disposition for the US Department of Energy (DOE) Office of Nuclear Energy (NE) Spent Fuel and Waste Science and Technology program. This work was performed to fulfill the Level 2 Milestone M2SF-17OR010201021, “Documentation of Non-destructive Tests on Sister Pins,” within work package SF-17OR01020102.

The High Burnup Spent Fuel Data Project, sponsored by DOE-NE, is focused on understanding the effects of long-term storage and transportation on high burnup (HBU) (>45 gigawatt days per metric ton uranium) light water reactor fuel. The goals of the project are to “provide confirmatory data for model validation and potential improvement, provide input to future spent nuclear fuel (SNF) dry storage cask design, support license renewals and new licenses for Independent Spent Fuel Storage Installations (ISFSIs), and support transportation licensing for high burnup SNF” [1]. In support of project goals, 25 sister rods were removed from fuel assemblies at the North Anna Power Station. Nine rods were removed from the project assemblies, and 16 rods were removed from similar HBU assemblies. The 25 sister rods were shipped to Oak Ridge National Laboratory (ORNL) Irradiated Fuels Examination Laboratory (IFEL) in early 2016 for detailed nondestructive examination (NDE) and destructive examination (DE). The detailed examinations will provide essential information on the physical state of the HBU rods and the fuel contained in the rods prior to loading, drying, and long-term dry storage [1]. Similar tests will be performed at the end of the long-term storage period to identify any changes in the fuel rods’ properties during the dry storage period [1].

While the planned NDE tasks are delineated in the sister rod test plan [2], this report provides an annual status of the work completed in FY2017. The NDE scope includes visual examinations of the rods’ external surfaces and gross dimensional measurements. In addition to the sister rod program’s NDE scope, two additional radiation scanning projects performed for the National Nuclear Security Administration (NNSA) and completed using the sister rods are also summarized. Also, a specialized eddy current examination for measurement of cladding hydrogen content was performed on 19 of the 25 sister rods by the Electric Power Research Institute (EPRI), and a summary of that exam is provided. The status of the NDE is summarized in Table S-1.

Table S-1. NDE status.

Planned NDE Observation	Status
NDE.01: Visuals of the complete exterior surface of each rod with a digitally created user-viewable montage of the surface, and the location and appearance of any physical abnormalities (e.g., chemical attack, blisters, cracks, heavy or uneven oxide layers, weld failures, or clad distortions)	Complete
NDE.02: Gamma scanning to nondestructively: <ul style="list-style-type: none"> a. obtain relative axial burnup profiles b. identify any gross migration of fission products or large pellet cracks c. identify any pellet stack gaps d. measure the pellet stack height e. identify the location and magnitude of any burnup depressions due to grid spacers 	Complete
NDE.03: Fuel rod overall length measurements	Complete
NDE.04: Eddy current scans to obtain information on clad mechanical macroscopic defects	Planned for October/November 2017
NDE.05: Profilometry measurements providing the rod outer diameter as a function of axial location	Complete
NDE.06: Rod surface temperature measurements	Planned for October/November 2017

Visual examinations of all 25 sister rods were completed in May 2017. The images are available in three user-viewable formats:

- (1) 784 individual, unprocessed photos per sister rod, for a total of 19,600 photos (the source data for the other two image sets),
- (2) 25 compiled user-interactive Shockwave Flash (SWF) collage files (one per sister rod), each containing 784 individual photos per sister rod, with each labeled for searching and observation, and
- (3) 96 flattened 40 mm axial segment collages per sister rod (2,400 total images) obtained by filtering and stitching together the individual azimuthal photos.

The images are only available in digital format and are stored on ORNL's CURIE resource [3] at <https://curie.ornl.gov/content/sister-rod-nde>. Waterside surface features relevant to the specification of future NDE and DE were identified via visual examination and tabulated. No weld failures, obvious cladding breaches, or other significant defects were observed. Rod identification and bar codes are visible on all rods except for F35P17 and F35K13 since bar codes were not used when these two rods were fabricated. A typical striated surface texture appearance which is visible in the images as alternating axial light and dark bands is present to varying degrees in all cases, with the more heavily oxidized rods having the appearance of deeper striations. The visual inspection indicated that shallow grid-to-rod fretting (GTRF) marks are common, and a few rods have deep GTRF marks. Several rods appear to have patches of Chalk River Unidentified Deposits (CRUD) and/or spalling oxide. Peeling oxide was identified on M5 and ZIRLO sister rods. Rod insertion (pre-irradiation) and rod removal from the parent fuel assembly produced long axial scratches on most rods. Interactions with grid springs and dimples may have scraped off CRUD or oxides along the length of the rods during assembly removal at the orthogonal grid spring locations.

Three sets of integrated radiation measurements were completed, including (1) one-dimensional scans using the Advanced Diagnostics and Evaluation Platform (ADEPT) sodium iodide (NaI) detector, (2) high resolution gamma spectroscopy using a high-purity germanium (HPGe) detector, and (3) gamma and neutron measurements using a fission/ionization chamber-based fork detector. The HPGe and fork detector measurements were performed for the DOE NNSA Office of Nonproliferation and Arms Control (NPAC) and are summarized here for completeness. There is very good agreement in the general trends and locations of grid burnup depressions. Differences of up to 7% were observed between the fork gamma counts and the HPGe total gamma counts near the rod bottom, likely due to the fact that a collimator is not used in the fork measurement. There is good agreement between all three detectors in the higher burnup regions of the rod. Radiochemical assay of selected rod locations will provide additional definitive (within measurement uncertainty) burnup measurements. The one-dimensional gamma scans of all 25 sister rods performed specifically for the sister rod project were completed using ADEPT in 2 energy ranges: 400 to 800 keV for examination of the fuel stack, and 1,100 to 1,600 keV for examination of the structural components. The two energy ranges were collected simultaneously. Data were collected in 1 mm increments along the axis of the rod and were indexed to the bottom of the rod. The scan signal exhibited the expected behavior without any sign of fission product accumulation or migration. The axial profile of the rods was as expected, and depressions in burnup were easily observed at the spacer grid locations. Pellet-pellet interface locations were also observable, so an estimate of the number of pellets in each rod could be made. The spring in the plenum region was visible, so an estimate of the length of the plenum region was also made. Some small fuel stack gaps were observed via the gamma scanning. The largest was estimated as 5 mm on sister rod 6U3P16.

The overall length of each sister rod was measured multiple times and was within the expected range.

Profilometry measurements were taken using two pairs of linear variable differential transformers (LVDTs) to measure the fuel rod diameter as a function of axial location. The two sets of measurements are 90° apart and can provide information on the extent to which the rod is out of round (*ovality*). Overall,

within the accuracy of the device and given the actual surface condition of the rods, no significant ovality (0.04 mm) was noted in the rods. In general, the expected diametrical trends were observed. Some rods had very thick oxide with large spalled areas (see Section 3.1). Rods with the thickest oxide layers appear to have some locally erratic diameter measurements. In particular, assemblies 3A1 and F35 show the expected increasing diameter from the bottom to the top of the rod (referenced to the true bottom for the F35 rods), but there is a large amount of point-to-point variation in the higher rod elevations due to the uneven spalling CRUD/oxide layer. A large ($\sim 3/4$ pellet length) reduced diameter (~ 0.5 mm) region was noted in the profilometry scan for rod 6U3P16 that is associated with the ~ 5 mm pellet-pellet gap identified during gamma scanning. Bambooning, which is a small diameter variation with a period of about 10 mm (the pellet length), was observed in all rods.

All sister rods were extensively photographed during the visual examination. The visual camera was also used to photograph the profilometry calibration rod, and the information obtained was used to resolve boundary pixel criteria and to scale the pixel count in each sister rod visual to a rod diameter. The diameter was measured in 40 mm increments along the length of the rod at 0, 45, 90, 135, 180, 225, 270, and 315-degree rotations. The diameter measurements based on the visuals were compared with the LVDT measurements and the features identified by gamma scan. Although these measurements are not considered to be as accurate as the LVDT measurements in total, they are useful in verifying trends, measuring the ends of the rods that cannot be measured with the LVDTs, and for additional observations around the circumference of the rod. Overall, this method gives reasonable agreement with the LVDT data, and the overall accuracy appears to be better than 0.05 mm. Optimization of the optical path and camera optics, along with a fixed reference point for picture-by-picture calibration, could lead to a non-contact fast measurement system.

The sister rod project eddy current measurements and rod surface temperature measurements have not yet been completed. They are scheduled for the September 2017 timeframe. EPRI performed Frequency-Scanning Eddy Current Technique (F-SECT) measurements on the sister rods in the IFEL hot cell. The F-SECT was developed specifically by EPRI to nondestructively estimate cladding hydrogen content. The F-SECT measurement includes point measurements of the combined zirconium oxide and CRUD thickness. It has been tested in both hot cell and poolside environments on zirconium alloys, including channel box, water rod, spacer, and fuel cladding. A total of 19 sister rods were successfully measured over 3 consecutive days. Rods included ZIRLO, M5, Zirc-4, and LT Zirc-4 clad rods. The detailed results will be reported by EPRI and are summarized in this document for information only. To date, only oxide/CRUD thickness data are available; the estimated hydrogen concentration data are expected to be available in November 2017.

This page is intentionally left blank.

ACKNOWLEDGMENTS

Many thanks to our US Department of Energy Office of Nuclear Energy (DOE-NE) sponsor, Ned Larson. The gamma and neutron scanning described in Sections 3.2.2 and 3.2.3 was possible due to the generosity of the International Nuclear Safeguards Technology Program, part of DOE NNSA NPAC. We also appreciate the Electric Power Research Institute's contributions in the area of eddy current examinations. We also wish to acknowledge the ORNL Irradiated Fuels Examination Laboratory for their support and cooperation in the handling and examination of the sister rods.

This page is intentionally left blank.

CONTENTS

SUMMARY	iii
ACKNOWLEDGMENTS	vii
LIST OF FIGURES	xi
LIST OF TABLES	xv
ACRONYMS	xvii
1. INTRODUCTION	1
2. NDE SCOPE	3
3. NDE RESULTS	5
3.1 NDE.01: Visual Examinations	5
3.1.1 General Condition	5
3.1.2 Typical Waterside Cladding Appearance of M5-Clad Rods	19
3.1.3 Typical Waterside Cladding Appearance of ZIRLO-Clad Rods	21
3.1.4 Typical Waterside Cladding Appearance of Zircaloy-4 and LT Zircaloy-4-Clad Rods	24
3.2 NDE.02 Gamma and Neutron Scanning	26
3.2.1 One-dimensional sodium iodide gamma scanning	27
3.2.2 HPGe Detector Scanning	39
3.2.3 Fork Detector Gamma and Neutron Scanning	44
3.3 NDE.03: Fuel Rod Overall Length	49
3.4 NDE.04: Eddy Current Examinations	49
3.4.1 F-SECT Measurements	49
3.4.2 Traditional eddy current measurements	51
3.5 NDE.05: Profilometry Measurements	51
3.5.1 LVDT Measurements	52
3.5.2 Visual Profilometry	53
3.6 NDE.06: Surface Temperature Measurements	53
4. REFERENCES	66
Appendix A	A-1
Appendix B	B-1

This page is intentionally left blank.

LIST OF FIGURES

Figure 1. Example of Visible Rod Labeling and Bar Coding (Partial Shown).....	7
Figure 2. Striated Surface Texture (Alternating Longitudinal Light and Dark Bands) Observed for (a) Highly Oxidized Rods and (b) a Lightly Oxidized M5 Rod.....	7
Figure 3. Typical Appearance of Orthogonal Longitudinal Scratches Consistent with Spacer Grid Spring/Dimple Interaction during Rod Insertion and Withdrawal from the Fuel Assembly.	8
Figure 4. Example of Circumferential Striping at Pellet-Pellet Interfaces (6U3P16).....	8
Figure 5. Typical Appearance of End Cap Welds, M5 Rod 30AE14 (Left) and ZIRLO Rod 6U3L08 (Right).	8
Figure 6. Typical Appearance of ADEPT Handling Marks (Left) and Manipulator Scratches (Right).....	8
Figure 7. Illustration of Visible Features on an M5 Sister Rod using (a) the Unprocessed Individual Photo, (b) the Interactive SWF, and (c) the Flattened and Filtered Collage and a ZIRLO Sister Rod using (d) the Unprocessed Individual Photo, (e) the Interactive SWF, and (f) the Flattened and Filtered Collage.	9
Figure 8. Selected Visual Observations from Assembly 30A.....	19
Figure 9. Selected Visual Observations from Assembly 5K7.....	20
Figure 10. Selected Visual Observations from Assembly 3D8.....	21
Figure 11. Selected Visual Observations from Assembly 6U3.....	22
Figure 12. Selected Visual Observations from Assembly 3F9.	23
Figure 13. Selected Visual Observations from Assembly F35.	24
Figure 14. Selected Visual Observations from Assembly 3A1.....	25
Figure 15. Comparison of Gamma Count Rates Collected by Three Different Detectors for Sister Rod 30AE14: HPGe, fork, and NaI. The Normalized Predicted Average Assembly Axial Fuel Burnup is also Plotted for Reference.	26
Figure 16. Gamma Scans for Sister Rod from Fuel Assembly 30A.	31
Figure 17. Gamma Scans for Sister Rod from Fuel Assembly 5K7.	32
Figure 18. Gamma Scans for Sister Rod from Fuel Assembly F35.....	33
Figure 19. Gamma Scans for Sister Rod from Fuel Assembly 3A1.	34
Figure 20. Gamma Scans for Sister Rod from Fuel Assembly 3F9.....	35
Figure 21. Gamma Scans for Sister Rod from Fuel Assembly 3D8.	36
Figure 22. Gamma Scans for Sister Rod from Fuel Assembly 6U3.....	37
Figure 23. Typical Pellet Ridging on a Fuel Rod Observed Via Gamma Scanning; Scales are Magnified to Show the Detail. The Typical Pellet is Approximately 10mm Long.	38
Figure 24. Diagram of the Measurement Geometry for the HPGe Campaign.....	39
Figure 25. Picture of the HPGe Detector during Spectroscopy Measurements.	40
Figure 26. HPGe Sum Spectrum of Sister Rod 30AD05.....	41

Figure 27. HPGe-derived Axial Scan of Sister Rod 30AD05 Using the Gross Peak Counts from the 661.6 keV Peak of ^{137}Cs	42
Figure 28. Superimposed Spectra of Coaxial Ge, NaI, and LaBr ₃ Detectors.....	43
Figure 29. Comparison of the Cooling Time and Burnup of Rod 3D8B2 by Detector Type.	43
Figure 30. (a) Fork Detector Head, (b) Fission and Ionization Chambers, (c) Rear View of Fork Detector Head (with Back Plate Removed).....	44
Figure 31. Measurement of a Spent Fuel Assembly in a Pool Using a Fork Detector [8].	44
Figure 32. Set Up for Calibrating the Fork Detectors at ORNL's RASCAL Facility.	45
Figure 33. Set Up for Measuring a Full-Length Sister Rod Using a Fork Detector in IFEL Hot Cell.	46
Figure 34. Set Up for Measuring a 5 × 5 Array of 25 Full-Length Spent Fuel Rods Using a Fork Detector at ORNL's IFEL Hot Cell with All Locations Filled with Sister Rods (Left) and with 8 Partially Vacant Locations (Right).	46
Figure 35. Normalized Fork Neutron and Gamma Count Rates along the Length of Fuel Rod 30AE14.....	47
Figure 36. Comparisons between the Fork Gamma and Neutron Count Rates with the Corresponding Calculated Neutron and Gamma Source Intensities in 9 Fuel Rods.	48
Figure 37. The F-SECT Bench Installed in the IFEL Hot Cell.....	50
Figure 38. Representative Sister Rod Lift-Off Data for Each Cladding Type.....	51
Figure 39. Profilometry Scans for Assembly 30A.....	54
Figure 40. Profilometry Scans for Assembly 5K7.....	55
Figure 41. Profilometry Scans for Assembly F35.....	56
Figure 42. Profilometry Scans for Assembly 3A1.....	57
Figure 43. Profilometry Scans for Assembly 3F9.....	58
Figure 44. Profilometry Scans for Assembly 3D8.....	59
Figure 45. Profilometry Scans for Assembly 6U3.....	60
Figure 46. Typical Pellet Ridging on a Fuel Rod via LVDT-Based Profilometry; Scales are Magnified to Show the Detail. The Typical Pellet is Approximately 10mm long.	61
Figure 47 Individual LVDT Measurements for Rod 30AG09 Illustrating the Difference in Measurements for the Two Pairs between 900 and 1,600 mm.	62
Figure 48. Average Diameter Reduction in Rod 6U3P16; This Reduction Nearly Aligns with the Pellet Stack Gap Noted in the Gamma Scan.....	63
Figure 49. Example of LVDT Measurements and Visual Diameter Measurements as Compared with Features Indicated by the Gamma Scans for Rod F35K13.....	64
Figure 50. Observed Sinusoidal Trend in Visual Profilometry Data with Angle of Rod Rotation.....	65
Figure A.1. Rod 3A1B16 LVDT Diameter Measurements.	A-2
Figure A.2. Rod 3A1F05 LVDT Diameter Measurements.....	A-3

Figure A.3. Rod 3D8B02 LVDT Diameter Measurements.	A-4
Figure A.4. Rod 3D8E14 LVDT Diameter Measurements.....	A-5
Figure A.5. Rod 3F9D07 LVDT Diameter Measurements.....	A-6
Figure A.6. Rod 3F9N05 LVDT Diameter Measurements.....	A-7
Figure A.7. Rod 3F9P02 LVDT Diameter Measurements.	A-8
Figure A.8. Rod 5K7C05 LVDT Diameter Measurements.	A-9
Figure A.9. Rod 5K7K09 LVDT Diameter Measurements.	A-10
Figure A.10. Rod 5K7O14 LVDT Diameter Measurements.....	A-11
Figure A.11. Rod 5K7P02 LVDT Diameter Measurements.....	A-12
Figure A.12. Rod 6U3I07 LVDT Diameter Measurements.....	A-13
Figure A.13. Rod 6U3K09 LVDT Diameter Measurements.....	A-14
Figure A.14. Rod 6U3L08 LVDT Diameter Measurements.....	A-15
Figure A.15. Rod 6U3M03 LVDT Diameter Measurements.	A-16
Figure A.16. Rod 6U3M09 LVDT Diameter Measurements.	A-17
Figure A.17. Rod 6U3O05 LVDT Diameter Measurements.....	A-18
Figure A.18. Rod 6U3P16 LVDT Diameter Measurements.....	A-19
Figure A.19. Rod 30AD05 LVDT Diameter Measurements.	A-20
Figure A.20. Rod 30AE14 LVDT Diameter Measurements.....	A-21
Figure A.21. Rod 30AG09 LVDT Diameter Measurements.....	A-22
Figure A.22. Rod 30AK09 LVDT Diameter Measurements.....	A-23
Figure A.23. Rod 30AP02 LVDT Diameter Measurements.....	A-24
Figure A.24. Rod F35K13 LVDT Diameter Measurements.....	A-25
Figure A.25. Rod F35P17 LVDT Diameter Measurements.	A-26
Figure B.1. Rod 3A1B16 LVDT Profilometry, Visual Profilometry, and Gamma Scan Data	B-2
Figure B.2. Rod 3A1F05 LVDT Profilometry, Visual Profilometry, and Gamma Scan Data.	B-3
Figure B.3. Rod 3D8B02 LVDT Profilometry, Visual Profilometry, and Gamma Scan Data	B-4
Figure B.4. Rod 3D8E14 LVDT Profilometry, Visual Profilometry, and Gamma Scan Data.	B-5
Figure B.5. Rod 3F9D07 LVDT Profilometry, Visual Profilometry, and Gamma Scan Data.	B-6
Figure B.6. Rod 3F9N05 LVDT Profilometry, Visual Profilometry, and Gamma Scan Data.	B-7
Figure B.7. Rod 3F9P02 LVDT Profilometry, Visual Profilometry, and Gamma Scan Data.....	B-8
Figure B.8. Rod 5K7C05 LVDT Profilometry, Visual Profilometry, and Gamma Scan Data.....	B-9
Figure B.9. Rod 5K7K09 LVDT Profilometry, Visual Profilometry, and Gamma Scan Data.....	B-10
Figure B.10. Rod 5K7O14 LVDT Profilometry, Visual Profilometry, and Gamma Scan Data.....	B-11
Figure B.11. Rod 5K7P02 LVDT Profilometry, Visual Profilometry, and Gamma Scan Data.	B-12

Figure B.12. Rod 6U3I07 LVDT Profilometry, Visual Profilometry, and Gamma Scan Data. B-13

Figure B.13. Rod 6U3K09 LVDT Profilometry, Visual Profilometry, and Gamma Scan Data. B-14

Figure B.14. Rod 6U3L08 LVDT Profilometry, Visual Profilometry, and Gamma Scan Data. B-15

Figure B.15. Rod 6U3M03 LVDT Profilometry, Visual Profilometry, and Gamma Scan Data. B-16

Figure B.16. Rod 6U3M09 LVDT Profilometry, Visual Profilometry, and Gamma Scan Data. B-17

Figure B.17. Rod 6U3O05 LVDT Profilometry, Visual Profilometry, and Gamma Scan Data. B-18

Figure B.18. Rod 6U3P16 LVDT Profilometry, Visual Profilometry, and Gamma Scan Data. B-19

Figure B.19. Rod 30AD05 LVDT Profilometry, Visual Profilometry, and Gamma Scan Data. B-20

Figure B.20. Rod 30AE14 LVDT Profilometry, Visual Profilometry, and Gamma Scan Data. B-21

Figure B.21. Rod 30AG09 LVDT Profilometry, Visual Profilometry, and Gamma Scan Data. B-22

Figure B.22. Rod 30AK09 LVDT Profilometry, Visual Profilometry, and Gamma Scan Data. B-23

Figure B.23. Rod 30AP02 LVDT Profilometry, Visual Profilometry, and Gamma Scan Data. B-24

Figure B.24. Rod F35K13 LVDT Profilometry, Visual Profilometry, and Gamma Scan Data. B-25

Figure B.25. Rod F35P17 LVDT Profilometry, Visual Profilometry, and Gamma Scan Data. B-26

LIST OF TABLES

Table S-1. NDE status.....	iii
Table 1. Visual observations by sister rod elevation, ZIRLO rods.....	10
Table 2. Visual observations by sister rod elevation, M5 Rods.....	12
Table 3. Visual observations by sister rod elevation, Zirc-4 and LT Zirc-4 Rods.....	16
Table 4. Results of gamma scanning grouped by rod type (± 1.5 mm, except for rod length, ± 0.5 mm).....	29
Table 5. Fuel stack gaps observed through gamma scanning (± 1 mm).	30

This page is intentionally left blank.

ACRONYMS

ADEPT	Advanced Diagnostics and Evaluation Platform
BU	burnup
CRUD	Chalk River Unidentified Deposits
DE	destructive examination
DOE	US Department of Energy
FY	fiscal year
GTRF	grid-to-rod fretting
HBU	high burnup
HPGe	high purity germanium
IAEA	International Atomic Energy Agency
IFEL	Irradiated Fuels Examination Laboratory
ISFSI	Independent Spent Fuel Storage Installation
LT	low tin
LVDT	linear variable differential transformers
MTU	metric ton of uranium
MW	megawatt
NaI	sodium iodide
NE	Office of Nuclear Energy
NDE	nondestructive examination
NNSA	National Nuclear Security Administration
NPAC	Office of Nonproliferation and Arms Control
OD	outer diameter
ORNL	Oak Ridge National Laboratory
PWR	pressurized water reactor
RASCAL	Radiation Standards Calibration
ROI	region of interest
SNF	spent nuclear fuel
SFWD	Spent Fuel and Waste Disposition
SFWST	Spent Fuel and Waste Science and Technology
SWF	Shockwave Flash

This page is intentionally left blank.

SPENT FUEL AND WASTE SCIENCE AND TECHNOLOGY SISTER ROD NONDESTRUCTIVE EXAMINATION ANNUAL REPORT FY2017

1. INTRODUCTION

The High Burnup Spent Fuel Data Project, sponsored by the US Department of Energy (DOE) Office of Nuclear Energy (NE), is focused on understanding the effects of long-term storage and transportation on high burnup (HBU) (>45 gigawatt days per metric ton uranium) light water reactor fuel. The goals of the project are to “provide confirmatory data for model validation and potential improvement, provide input to future SNF dry storage cask design, support license renewals and new licenses for Independent Spent Fuel Storage Installations (ISFSIs), and support transportation licensing for high burnup SNF” [1].

In support of the project goals, 25 sister rods were removed from fuel assemblies at the North Anna Power Station. Nine rods were removed from the project assemblies, and 16 rods were removed from similar HBU assemblies. The 25 sister rods were shipped to Oak Ridge National Laboratory (ORNL) in early 2016 for detailed nondestructive examination (NDE) and destructive examination (DE) in the Irradiated Fuels Examination Laboratory (IFEL). The detailed examinations will provide essential information on the physical state of the HBU rods and the fuel contained in the rods prior to loading, drying, and long-term dry storage [1]. Similar tests will be performed at the end of the long-term storage period to identify any changes in the properties of the fuel rods during the dry storage period [1].

While the planned NDE tasks are delineated in the sister rod test plan [2], this report describes the progress of the NDE and provides a summary of the measurements to date.

This page is intentionally left blank.

2. NDE SCOPE

The sister rod program's NDE scope includes visual examinations of the rods' external surfaces and gross dimensional measurements [2]. Some exams are still ongoing, but at the conclusion of the NDE, all 25 sister rods will have been examined using ORNL's Advanced Diagnostics and Evaluation Platform (ADEPT) for the following:

NDE.01: Visuals of the complete exterior surface of each rod with a digitally created, user-viewable montage of the surface, and the location and appearance of any physical abnormalities (e.g., chemical attack, blisters, cracks, heavy or uneven oxide layers, weld failures, or clad distortions);

NDE.02: Gamma scanning to nondestructively:

- a. obtain relative axial burnup profiles
- b. identify any gross migration of fission products or large pellet cracks
- c. identify any pellet stack gaps
- d. measure the pellet stack height
- e. identify the location and magnitude of any burnup depressions due to grid spacers;

NDE.03: Fuel rod overall length measurements;

NDE.04: Eddy current scans to obtain information on clad mechanical macroscopic defects;

NDE.05: Profilometry measurements providing the rod outer diameter as a function of axial location;

NDE.06: Rod surface temperature measurements.

In addition to the sister rod program's NDE scope, two additional radiation scanning projects performed for the National Nuclear Security Administration (NNSA) were completed and are summarized in Sections 3.2.2 and 3.2.3. Also, a specialized eddy current examination for measurement of cladding hydrogen content was performed on 19 of the 25 sister rods by the Electric Power Research Institute (EPRI), and a summary of that exam is also provided in Section 3.4.1.

This page is intentionally left blank.

3. NDE RESULTS

3.1 NDE.01: Visual Examinations

Visual examinations of all 25 sister rods were completed in May 2017. Three sets of images are available:

- (4) 784 individual unprocessed photos per sister rod, for a total of 19,600 photos (the source data for the other two image sets),
- (5) 25 compiled user-interactive Shockwave Flash (SWF) collage files (one per sister rod) containing 784 individual photos per sister rod, with each labeled for searching and observation, and
- (6) 96 flattened 40 mm axial segment collages per sister rod (2,400 total images) obtained by filtering and stitching together the individual azimuthal photos.

All three sets of images are available in digital format only and stored on ORNL's CURIE.ORNL.gov resource [3]. The file name nomenclature for individual digital photos is:

XXXZZZ-YYYYMMDD01-A###-D---_S***.jpg,

where:

XXX	is the sister rod parent assembly ID,
ZZZ	is the sister rod lattice location in the parent assembly,
YYYY	is the year the image was captured,
MM	is the month the image was captured,
DD	is the day the image was captured,
###	indicates the azimuthal orientation, in degrees, at which the image was captured,
---	indicates the axial elevation at which the image was captured, in mm, from the bottom of the fuel rod, with the exception of rods F35P17 and F35K13, which were loaded into the shipping container and hot cell backwards, so their elevations are from the tops of the rods, and
***	is a tracking number issued by the software.

The file name nomenclature used for the flattened collage sections is:

stitched_XXXZZZ-YYYYMMDD01-Axxx-D---_Sxxx.png, and

the nomenclature used for the interactive SWF files is:

XXXZZZ-Collage_out.swf,

where the variables are those previously defined for the individual photos. The SWF files are opened using a web browser, and appear to work best with Microsoft Internet Explorer.

Figure 8. through Figure 11 provide a collection of general observations ordered by assembly number. The majority of the images presented in this section include white arrows meant to indicate the visual feature discussed in the text. While most images present the full section of the rod in the imaging view in a horizontal axial orientation on the page, some images have been rotated or cropped for space.

3.1.1 General Condition

No weld failures, obvious cladding breaches, or other significant defects were observed. Rod identification and bar codes are visible on the rods (an example is shown in Figure 1), except on F35P17 and F35K13 since bar codes were not used when these two rods were fabricated. The visual inspection indicated that shallow grid-to-rod fretting (GTRF) marks are common, and a few rods have patches of Chalk River Unidentified Deposits (CRUD) and/or spalling oxide. A typical striated surface texture

appearance, visible in the images as alternating axial light and dark bands (Figure 2), is present to varying degrees in all cases, with the more heavily oxidized rods having the appearance of deeper striations.

For the Zircaloy-4 (Zirc-4), low tin (LT) Zirc-4, and ZIRLO fuel rods, when the parent fuel assembly was fabricated, the fuel rods were pulled or pushed through the spacer grids with the springs/dimples engaged. Interaction with the spacer grid springs and dimples during rod insertion can produce long, shallow axial scratches along much of the rod's length at the azimuthal locations of the grid springs/dimples. These are visible on the rod as oxidized scratches, as shown in Figure 3. Likewise, in many cases, interaction with the spacer grid springs and dimples during rod removal created long axial scratches along much of the rod length at orthogonal locations (consistent with the location of the grid springs/dimples), removing surface CRUD and perhaps some oxide. In contrast, the M5 fuel rods were inserted into the assembly using a method called "keying" in which the springs and dimples are depressed to prevent scratching of the cladding during assembly fabrication. Therefore, it is likely that any axial scratches observed on the M5 rods occurred during rod removal.

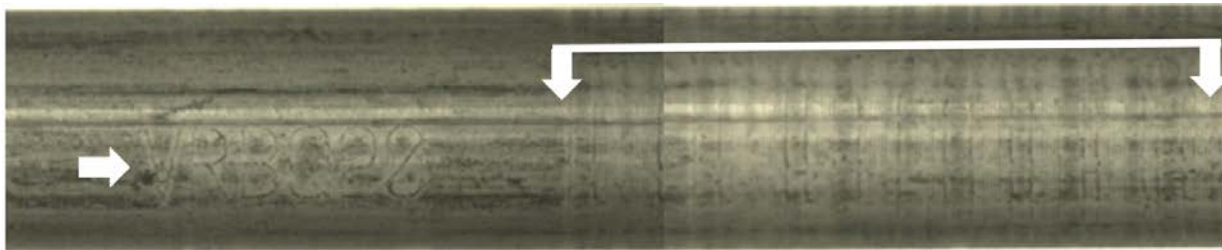
The pellet-pellet interfaces are frequently visible in the images as circumferential dark stripes, as illustrated in Figure 4. During in-reactor operation, the cladding at the pellet-pellet interface is slightly cooler, and hydrogen is known to migrate to these cooler regions. Also, oxidation is slightly lower at the cooler pellet-pellet interfaces. The combination of these two effects creates a band of deeper coloration at the pellet-pellet interfaces. End cap welds are also clearly visible, as illustrated in Figure 5.

During the visual examination, the rods are moved and rotated to the position in front of the camera using the ADEPT system. The large amount of rod handling required for the photos can introduce some rubbing or polishing to the cladding's outer surfaces, resulting in minor visual artifacts that could be confused with pellet-pellet interfaces. Since the pellets are approximately 10 mm long, banding that is spaced at a frequency other than 10 mm is likely a result of clad polishing during handling. Additionally, necessary handling of the rods using the in-cell manipulators can produce scratches, typically visible as bright diagonal marks on the rod's surface, as illustrated in Figure 6. Some additional examples of handling marks are provided in Tables 1 and 4. Finally, the profilometry measurements (see Section 3.5) were completed prior to the visual examinations. These examinations used contact probes that may have removed some CRUD or left some markings on the rod, although no such markings were identified as of this review.

Due to their dark matte black appearance, it is difficult to detect features on the surface of the M5 rods using the interactive images or the raw images. As an illustration, Figure 7(a)(b)(c) shows side by side images of the same rod with an elevation and rotation having a burnishing mark (a very shallow fretting wear mark). The burnishing mark is clearly visible in the flattened and contrast filtered collage, but it is barely discernible in the SWF format. Features on the Zirc-4, LT Zirc-4, and ZIRLO rods are also generally more discernible in the flattened collage format, as well, but some features can become less apparent due to the large format and high contrast filtering used, as illustrated in Figure 7(d)(e)(f).

Tables 1, 2 and 3 provide a summary of the visible features identified using the visual exam data for ZIRLO, M5 and Zirc-4/LT Zirc-4 sister rods, respectively. Typical oxidation patterning is not annotated in the tables, but thicker than expected oxide, oxide spalling, and oxide peeling are noted. The rod insertion/removal scratches are likewise not annotated, as they are present on all rods at almost every elevation. Also, the severity of the feature is not annotated (e.g., fretting is noted, but it is not categorized as shallow, moderate or deep in the tables). In some areas there is an appearance of depth to markings that resembles debris, and this has been noted in the table. However, at this time, no debris indication has been confirmed. As mentioned previously, feature visibility varies depending upon the image set. The majority of the data listed in the tables is based on a survey of the flattened images. The tables are not considered to be an exhaustive listing, but they do provide a good overall summary of the variety of features present for each sister rod.

Sections 3.1.2, 3.1.3, and 3.1.4 provide a general discussion by alloy type and parent fuel assembly.



Two images — 3F9N05-2017050901-A000_D3811_S768.jpg and 3F9N05-2017050901-A000_D3771_S753.jpg — are stitched together. Although these images are from the same rod and are adjacent photos, there is an obvious difference in image contrast (right vs left) due to instantaneous lighting conditions.

Figure 1. Example of Visible Rod Labeling and Bar Coding (Partial Shown).

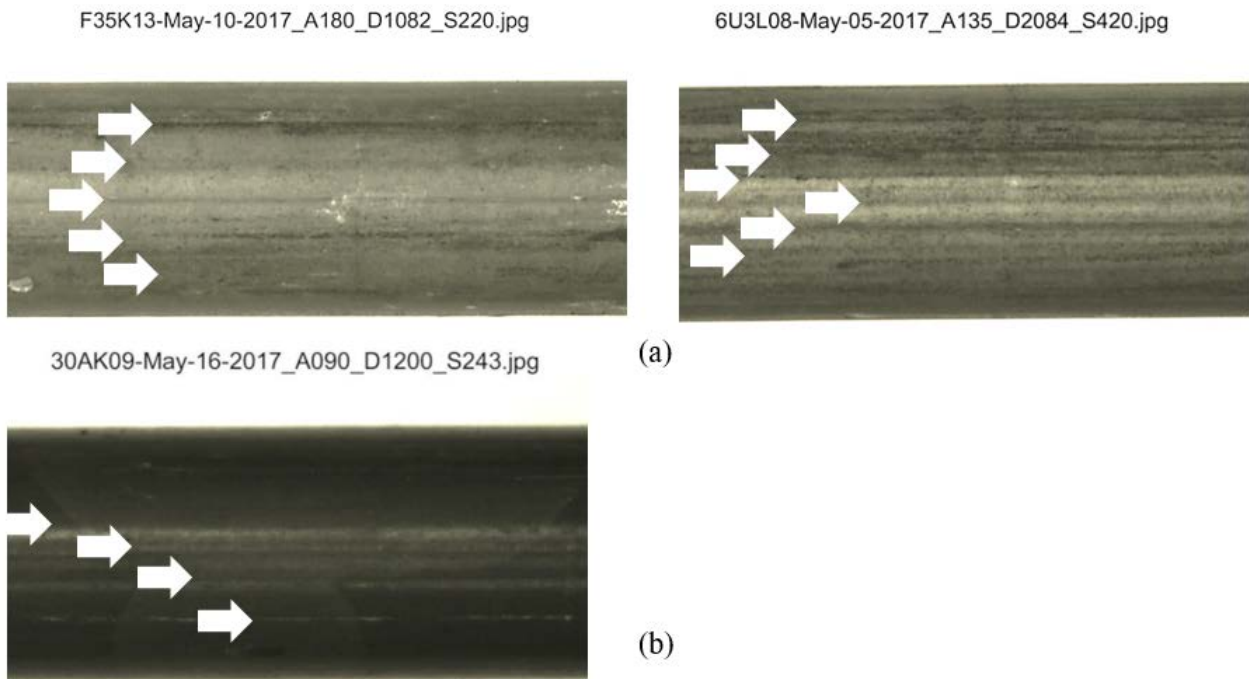


Figure 2. Striated Surface Texture (Alternating Longitudinal Light and Dark Bands) Observed for (a) Highly Oxidized Rods and (b) a Lightly Oxidized M5 Rod.

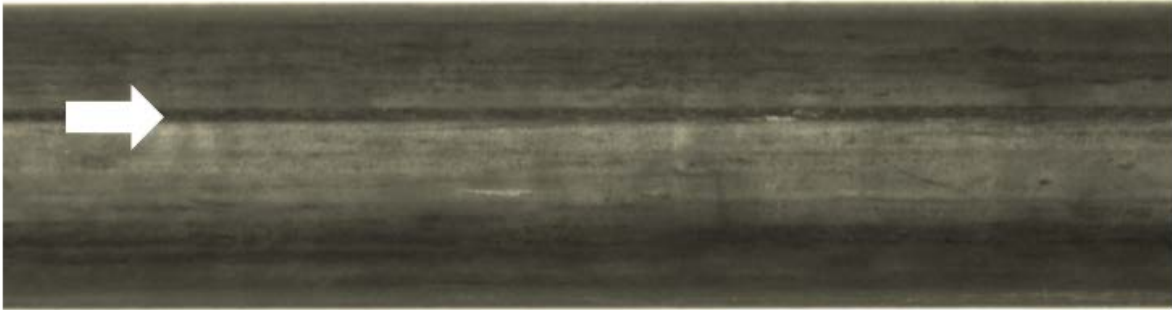


Figure 3. Typical Appearance of Orthogonal Longitudinal Scratches Consistent with Spacer Grid Spring/Dimple Interaction during Rod Insertion and Withdrawal from the Fuel Assembly.

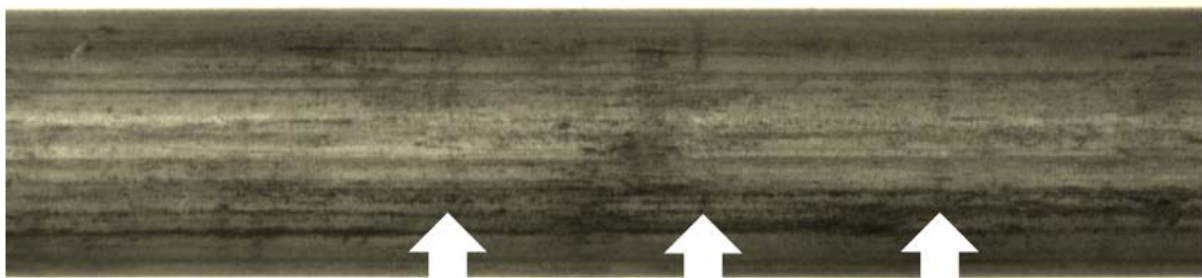


Figure 4. Example of Circumferential Striping at Pellet-Pellet Interfaces (6U3P16).

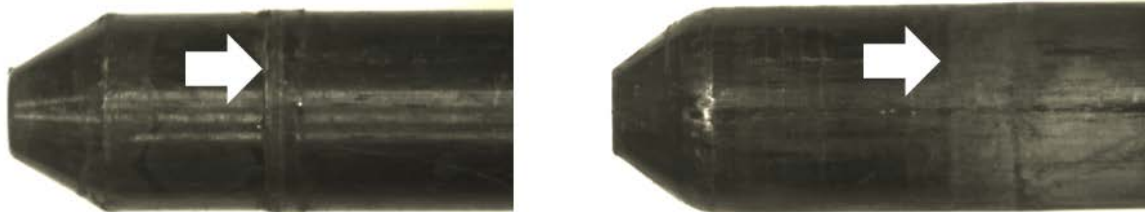


Figure 5. Typical Appearance of End Cap Welds, M5 Rod 30AE14 (Left) and ZIRLO Rod 6U3L08 (Right).

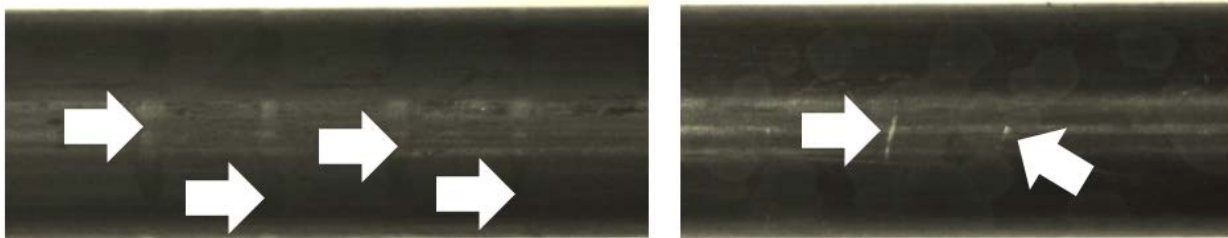
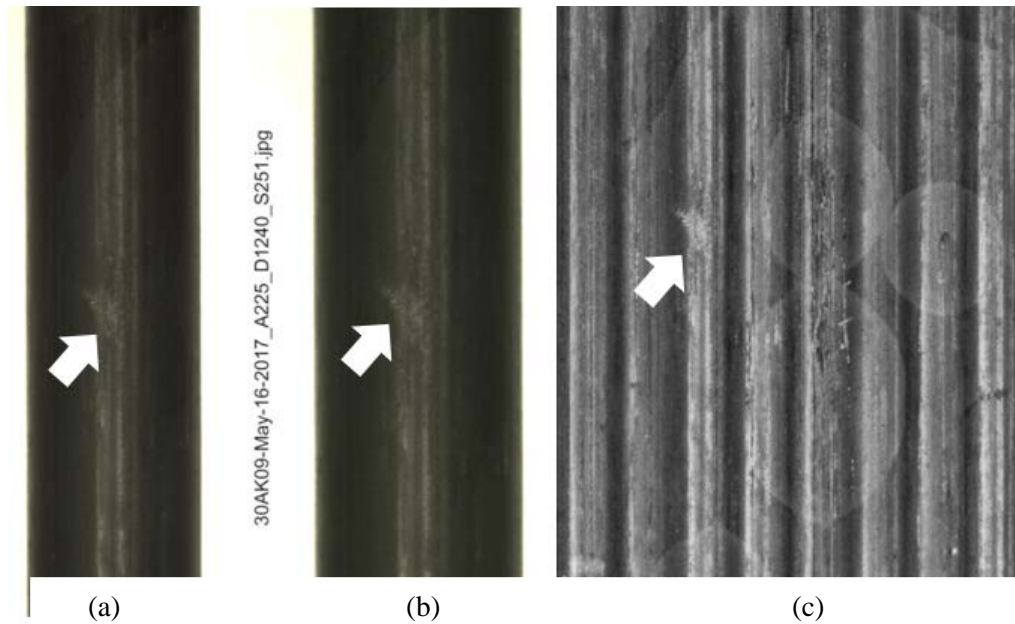
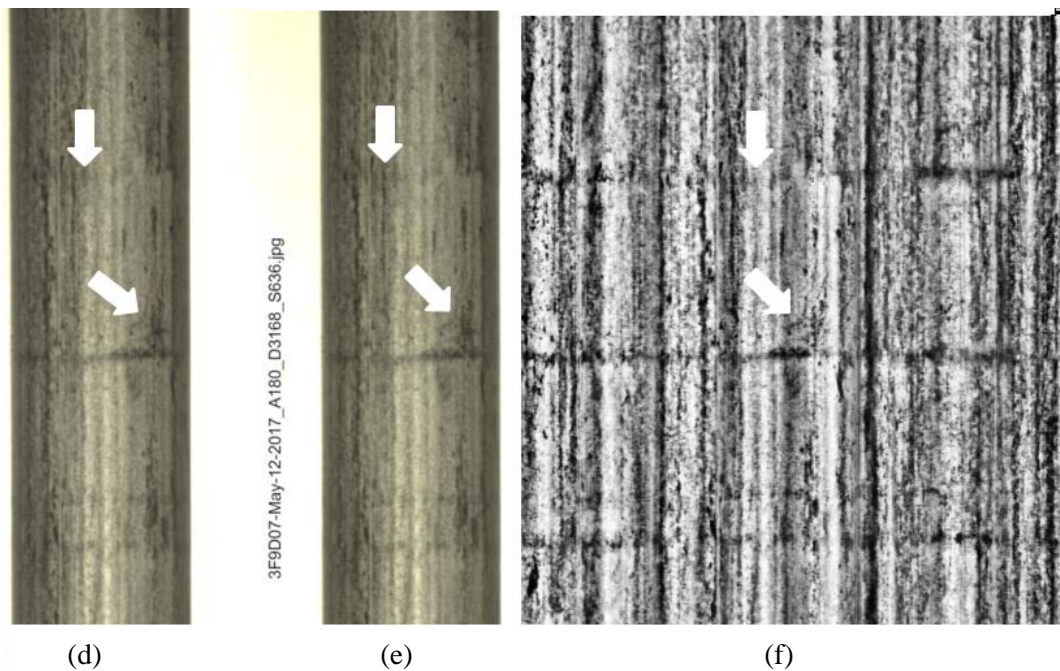


Figure 6. Typical Appearance of ADEPT Handling Marks (Left) and Manipulator Scratches (Right).



On the matte black M5 rods above, features such as the fretting mark (as indicated by the arrow) and the circular patches of oxidation become more visible.



On the shiny grey surfaces of the Zirc-4, LT Zirc-4 and Zirlo rods, the flattened and filtered image can make some features such as the pellet-pellet boundaries more visible, while some features, such as the dark patch highlighted with the arrow, become indistinct.

Figure 7. Illustration of Visible Features on an M5 Sister Rod using (a) the Unprocessed Individual Photo, (b) the Interactive SWF, and (c) the Flattened and Filtered Collage and a ZIRLO Sister Rod using (d) the Unprocessed Individual Photo, (e) the Interactive SWF, and (f) the Flattened and Filtered Collage.

Table 1. Visual observations by sister rod elevation, ZIRLO rods.

Key: F=fretting, FM=flow marking, HS=handling scratches, HM= handling marks, DP=dark patch, LP=light patch, HO=heavy oxide, SO=spalling oxide, PB=pellet banding, FL=flaky appearance, UPC=rod bar code, DB=debris, DS= dark "scratches", OR=peeling oxide rings, BR=burnishing; a question mark (?) is meant to imply uncertainty about the observation immediately preceding it. Typical oxidation patterning is not included. Blank cells mean that no features beyond typical were observed.

Elevation from rod bottom (approx. mm)	6U3I07	6U3K09	6U3L08	6U3M03	6U3M09	6U3O05	6U3P16	3D8B02	3D8E14	3F9D07	3F9N05	3F9P02
0000												
0040	HS, F, LP	HS		HS	HS	HS	HS	HS	HS	HS	HS	HS
0080	LP, HS	HS	HS	HS		HS		HS		HS	HS	HS, LP
0120	LP, HS							HS		HS		HS
0160	LP		HS		HS				F	F, HS	HS	HS
0201	LP, PB				HS				DP		DP, HS	HS
0241	LP, F, HS		HS			HS	HS		FM	DS, DP	FM	FM
0281									LP			
0321			HS						HS	HS	DP	
0361		FM, LP, FL			FM		FM	HS	HS, DP	HS		HS
0401		HS	HS	FM				HS	HS			
0441		HS	HS					HS				
0481	PB		HS, DP		PB		PB		FM			
0521	HS	HS	HS				DS					
0562	F	HS, DP				HS			DP			HS
0602	DS					HS	HS		DP, LP	HS, F		F
0642	DS	F								HS		
0682	HS	F					HS					F
0722		F					HS	HS				LP
0762				FM		HS						
0802							DS		HS, DB			
0842	PB						DS, HS	HS				
0882	PB		PB		HS							
0923	DP, PB	HM						HS			DP	
0963	PB			FM		HS			DP			
1003	PB					HS	HS		DP, LP			PB
1043	PB						DS		DS	DP		PB, DP
1083	PB						DS					
1123	PB	PB					HS					
1163	PB	F	HS				HS					DP
1203	PB	F					F	F	F	F		F, DP
1244	PB	F						HS		F		DP
1284	PB											
1324	PB, DP											
1364	PB		HS									LP, DB?
1404	PB, SO						PB					LP
1444	PB						PB					
1484	PB			FM			PB					
1524	PB					HM	PB					LP, HM
1564	PB					FM						HS
1605						FM		HS		PB, DP		
1645	PB		HS, PB			DS		HS, F				
1685	PB											HS, PB
1725	PB		PB				F					PB
1765			F				HM					

Sister Rod Nondestructive Examination Annual Report FY2017

September 15, 2017

Key: F=fretting, FM=flow marking, HS=handling scratches, HM= handling marks, DP=dark patch, LP=light patch, HO=heavy oxide, SO=spalling oxide, PB=pellet banding, FL=flaky appearance, UPC=rod bar code, DB=debris, DS= dark "scratches", OR=peeling oxide rings, BR=burnishing; a question mark (?) is meant to imply uncertainty about the observation immediately preceding it. Typical oxidation patterning is not included. Blank cells mean that no features beyond typical were observed.

Elevation from rod bottom (approx. mm)	6U3I07	6U3K09	6U3L08	6U3M03	6U3M09	6U3O05	6U3P16	3D8B02	3D8E14	3F9D07	3F9N05	3F9P02
1805	PB									PB		
1845			PB		HS	DS		HS				
1885					HS					Imaging artifact, straight white line?		
1925			PB									
1966	PB		F									
2006			F		PB		PB					LP (HO?)
2046												
2086								HS, DP				
2126	F									DP		
2166						FM						
2206	PB									FM		
2246	F		F							F		F
2286	F	F	PB							F, PB		
2327		PB	PB				FM					
2367	F									DS		
2407			PB, LP									
2447				FM						PB, DP		
2487										PB	F	
2527			HM			FM	DS				PB, HM	
2567			HM							PB	PB	
2607	PB		PB							PB	PB	
2647	PB		HO							PB	PB	
2688		F	PB			F				PB	PB	
2728			HO			DS	DS			PB	PB	
2768			HO				DS			F, FL	PB, F, SO	
2808											PB, F, SO	
2848	F		LP, PB								PB, SO	
2888	HS		PB							PB, HM	PB, SO	
2928						F				PB	PB, SO	
2968	F									PB	PB, SO	DP
3009	F									PB	PB, SO	PB
3049	HS		HM, F							PB	PB, SO	PB
3089	HS									PB	PB, SO	PB
3129						PB			PB	PB	PB, SO	PB
3169						F			PB	PB, HS	PB, SO	PB
3209									PB	PB	PB, SO	PB
3249				FM					PB	PB	PB, SO	PB
3289										PB	PB, SO	PB, LP, F with HO?
3329	HS						HS			PB	PB, SO	PB
3370					HS	FM				PB	PB	PB
3410	FM	FM	FM	FM	HS	FM	FM		PB	PB	PB	F, FM
3450									PB	PB	PB	

Key: F=fretting, FM=flow marking, HS=handling scratches, HM= handling marks, DP=dark patch, LP=light patch, HO=heavy oxide, SO=spalling oxide, PB=pellet banding, FL=flaky appearance, UPC=rod bar code, DB=debris, DS= dark "scratches", OR=peeling oxide rings, BR=burnishing; a question mark (?) is meant to imply uncertainty about the observation immediately preceding it. Typical oxidation patterning is not included. Blank cells mean that no features beyond typical were observed.

Elevation from rod bottom (approx. mm)	6U3I07	6U3K09	6U3L08	6U3M03	6U3M09	6U3O05	6U3P16	3D8B02	3D8E14	3F9D07	3F9N05	3F9P02
3490										PB	PB	
3530									PB	PB	PB	
3570										PB	PB	
3610	PB									PB	PB	DP
3650	FM, HS, HM	FM	FM	FM	FM	FM	FM	FM	FM	PB, FM	F	FM
3690			HM									
3731			HM							HM		
3771	HM	HS	UPC	UPC				UPC	UPC	HM, UPC	UPC	UPC
3811	UPC	UPC	UPC	UPC	UPC	UPC	UPC	UPC	UPC	UPC	UPC	UPC
3851		HS	UPC	UPC	UPC	UPC	UPC	UPC		HM, UPC	UPC	UPC
3891												

Table 2. Visual observations by sister rod elevation, M5 Rods.

Key: F=fretting, FM=flow marking, HS=handling scratches, HM= handling marks, DP=dark patch, LP=light patch, HO=heavy oxide, SO=spalling oxide, PB=pellet banding, FL=flaky appearance, UPC=rod bar code, DB=debris, DS= dark "scratches", OR=peeling oxide rings, BR=burnishing; a question mark (?) is meant to imply uncertainty about the observation immediately preceding it. Typical oxidation patterning is not included. Blank cells mean that no features beyond typical were observed.

Elevation from rod bottom (approx. mm)	5K7C05	5K7K09	5K7O14	5K7P02	30AD05	30AE14	30AG09	30AK09	30AP02
0000									
0040	HS	HS	HS	HS	HS	HS	F, HS	HS	HS
0080	HS	HS	HS	F	HS		HS	HS, F	HS
0120	HS, OR	HS, OR	HS, F		HS	HS		F	F
0160	HS, OR	HS, OR	HS	HS	HS				
0200	HS, OR	OR	HS	HS	HS	OR			
0240	HS, OR		HS	HS		OR			HS
0280	HS, OR		LP	HS					
0320	HS, UPC	UPC	UPC	HS	UPC	UPC	UPC, LP	UPC	UPC
0360	HS, FL	UPC	UPC	UPC	UPC	UPC	UPC, HS	UPC, FL	UPC, HS
0400	FL (CRUD?)	F, Heavy FL (CRUD?)	HS, DP			UPC	HS		
0440	FL (CRUD?)	Heavy FL (CRUD?)	FL						HS
0480	Heavy FL (CRUD?)		Heavy FL (CRUD?)		HS		HS		HS
0520	Heavy FL (CRUD?)		HS	Heavy FL (CRUD?)	HS				HS

Key: F=fretting, FM=flow marking, HS=handling scratches, HM= handling marks, DP=dark patch, LP=light patch, HO=heavy oxide, SO=spalling oxide, PB=pellet banding, FL=flaky appearance, UPC=rod bar code, DB=debris, DS= dark "scratches", OR=peeling oxide rings, BR=burnishing; a question mark (?) is meant to imply uncertainty about the observation immediately preceding it. Typical oxidation patterning is not included. Blank cells mean that no features beyond typical were observed.

Elevation from rod bottom (approx. mm)	5K7C05	5K7K09	5K7O14	5K7P02	30AD05	30AE14	30AG09	30AK09	30AP02
0560	FL (CRUD?)	LP	HS	Heavy FL (CRUD?), F			HS		HS
0600			Heavy FL (CRUD?)	F		HS, DB?	F, deep rod removal scratches	HS	
0640				HS		HS	HS	HS, F	
0681	F	F	F	F	F	HS	HS	F	F
0721		F	F, HS	F	HS, BR	F	HS	F, HS	F
0761	HS		HS	F	HS, BR		HS	HS	
0801			HS, PB	F, HS, PB		HS	HS	HS	
0841			HS	PB			HS		
0881	LP				LP	LP	HS		
0921	LP						HS	F, HS	
0961						LP (wear?)			PB
1001			HS		LP	LP (wear?)	PB		PB
1041			LP				F		PB
1081	HS		PB		HS				
1121					HS, BR	HS, F	deep rod removal scratches	HS	
1161		F				F	HS	BR	
1201	OR, F, DB?		F	F	F	F, HS	HS	F	F
1241	OR, F		F	F	F	LP, HS	F	F	F
1281				F		LP, HS		F	
1321				F	BR				BR
1361	HS					LP	F		HS
1401			HS, LP		BR		F	F	BR
1441			HS, LP						
1481					HS				
1521	PB, DB?, HS	PB	OR	PB, HS		LP, PB	PB	PB	PB
1561	PB	PB, LP	OR, PB	PB, LP, HS, HM		HS, PB	PB	PB	PB
1601	PB	PB, LP	PB	PB, OR		HS, PB	PB	PB, BR	PB
1641	PB	PB, LP				PB	PB	PB	PB, HS
1681		F	PB, F	HS, F		PB, F, HS	PB	PB	BR, PB
1721	F	F	F	F	PB		PB	PB	F, PB
1761		F	HS, F	F, PB	HS, PB	F, HS, PB	PB	PB	F, PB
1801			F	F, PB	PB	PB	PB	PB	
1841	PB			PB	PB	PB	PB	PB	
1881			F	F, PB	PB	PB	PB	PB	

Key: F=fretting, FM=flow marking, HS=handling scratches, HM= handling marks, DP=dark patch, LP=light patch, HO=heavy oxide, SO=spalling oxide, PB=pellet banding, FL=flaky appearance, UPC=rod bar code, DB=debris, DS= dark "scratches", OR=peeling oxide rings, BR=burnishing; a question mark (?) is meant to imply uncertainty about the observation immediately preceding it. Typical oxidation patterning is not included. Blank cells mean that no features beyond typical were observed.

Elevation from rod bottom (approx. mm)	5K7C05	5K7K09	5K7O14	5K7P02	30AD05	30AE14	30AG09	30AK09	30AP02
1921		F	F	F, PB	PB	PB	HB, PB, HS	PB	
1962		Local striping	PB	F, PB	PB	PB	HM	PB	
2002		Local striping	PB	F, PB	PB, F	PB	HM	PB	F
2042	F		PB	PB		PB	HM	PB	
2082		LP	PB	PB		PB	HM	PB	
2122			PB	PB	HM	PB	F, PB, HM	PB	
2162			PB	PB	HM	PB	HM, PB	PB	
2202	LP (DB?)		F	PB	PB	PB	PB	PB, HS	
2242			F	F	PB	PB	PB	PB	F
2282		F		F, PB	PB, F	PB	PB	PB	
2322					PB	PB	F, PB	PB, HS, F, HM	
2362	LP	, HS			PB	PB	F, PB	HM	
2402	LP, HS	PB			PB	PB, HS	PB	HM	
2442		F		HM	PB	HS, F, HM	PB, HM	HM	
2482		F		HM, F	HM	HS, F, HM	PB, HM	HM, BR	
2522	F	LP, PB	F	F, HM	HM	Local striping, PB, HM	PB, HM	HM	
2562			F, PB	F, HM	HM	HM		HM	
2602	HM, HS			HM	HM	HM, FL, PB		HM	
2642	HS	HS		HM	HM	HM, HS		HM	
2682				HM	HM	HM	DP, HM	HM	
2722	HS	F, PB		HM	HM	HM	Heavy HM	HM	
2762	HS	LP		HM	HM	HM, HS, PB, F	Heavy HM	HM	F, HS
2802	BR, F	F		F, HM	HM	F, HM	Heavy HM	HM	HS, F
2842				HM	HM	HM	Heavy HM	HM	HM
2882		LP		HM	HM	HM, PB	Heavy HM	HM	HM
2922		HM		HM	HS, HM	HS	Heavy HM	HM	HM
2962				HM	HM	HM, HS, PBHM, HS	Heavy HM	HM, F	HM

Table 3. Visual observations by sister rod elevation, Zirc-4 and LT Zirc-4 Rods.

Key: F=fretting, FM=flow marking, HS=handling scratches, HM= handling marks, DP=dark patch, LP=light patch, HO=heavy oxide, SO=spalling oxide, PB=pellet banding, FL=flaky appearance, UPC=rod bar code, DB=debris, DS= dark “scratches”, OR=peeling oxide rings; BR=burnishing; a question mark (?) is meant to imply uncertainty about the observation immediately preceding it. Typical oxidation patterning is not included. Blank cells mean that no features beyond typical were observed.

Elevation from rod bottom (approx. mm)	3A1B16	3A1F05	F35K13 (backward)	F35P17 (backward)
0000				
0040		HS, LP	HS	HS
0080		HS, F		DS, HS
0120				HS
0160				
0201				
0241			FM	
0281				
0321		HS		SO, FL
0361				SO, FL
0401				SO, FL
0441			SO	SO, FL
0481	HS	HM, F, HS, FM	SO, FL	SO, FL
0521	HS		SO	SO, FL
0562	HS	HS, DP	SO	SO
0602		HS, F	SO	SO
0642	F	HS, DP, HM	SO	SO, FL
0682		HS, DP	SO	SO, FL
0722		DP, LP	SO	SO, FL
0762	HS	DP, LP		SO, FL
0802		HS, DP	SO	SO, FL
0842		HS	SO	SO, FL
0882			SO	SO, FL
0923		PB	SO, FL	SO, FL
0963			SO	SO, FL
1003			SO, FL	SO, FL
1043	DP		SO, FL	SO, FL
1083			SO	SO
1123		F		SO
1163			SO	SO, FL
1203	F		SO, FL	SO, FL
1244	BR	HS	SO	SO, FL
1284			SO	SO, FL
1324		FM	SO, FL	SO, FL
1364			SO, FL	SO, FL
1404			SO, FL	SO, FL
1444			SO, FL	SO, FL
1484	PB		SO, FL	SO, FL
1524	PB		SO	SO, FL
1564	HS	PB or HM	SO	SO
1605	PB, LP			

Key: F=fretting, FM=flow marking, HS=handling scratches, HM= handling marks, DP=dark patch, LP=light patch, HO=heavy oxide, SO=spalling oxide, PB=pellet banding, FL=flaky appearance, UPC=rod bar code, DB=debris, DS= dark “scratches”, OR=peeling oxide rings; BR=burnishing; a question mark (?) is meant to imply uncertainty about the observation immediately preceding it. Typical oxidation patterning is not included. Blank cells mean that no features beyond typical were observed.

Elevation from rod bottom (approx. mm)	3A1B16	3A1F05	F35K13 (backward)	F35P17 (backward)
1645	PB	PB		
1685	PB	PB	SO	SO
1725	PB	PB	SO	SO, FL
1765	PB, HS	PB	SO	SO, FL
1805	PB	PB	SO	SO, FL
1845	PB	PB	SO	SO, FL
1885	PB	PB	SO	SO, FL
1925	PB	PB	SO	SO, FL
1966	PB	PB		SO, FL
2006	PB	PB		SO
2046	PB	PB		SO
2086	PB	PB		
2126	PB	PB, FL		
2166	PB	PB, FL		HS
2206	PB	PB, FL		
2246	PB, HO			PB
2286				
2327		PB		
2367		PB, FL		
2407		PB, FL		
2447	PB, SO	PB, FL		
2487	PB, SO	PB, FL		
2527	PB, SO, HM	PB, FL	HS	
2567	PB, SO	PB, SO		
2607	PB, SO	PB, SO		
2647	PB, SO, HM, FL	PB, SO		
2688	PB, SO, HM, FL	PB, SO		
2728	PB, SO, HM, FL	PB, SO		
2768		PB, SO	F	HS
2808	PB	PB, SO		PB
2848		PB, SO		
2888	SO, FL	PB, SO		
2928	HO, FL	PB, SO		
2968	HO, FL	PB, SO		
3009	SO, FL	PB, SO		
3049	SO, FL	PB, SO		
3089	HO, FL	PB, SO		
3129		PB, SO		
3169		PB, SO	HS	FM
3209		PB, SO	HS	

Key: F=fretting, FM=flow marking, HS=handling scratches, HM= handling marks, DP=dark patch, LP=light patch, HO=heavy oxide, SO=spalling oxide, PB=pellet banding, FL=flaky appearance, UPC=rod bar code, DB=debris, DS= dark “scratches”, OR=peeling oxide rings; BR=burnishing; a question mark (?) is meant to imply uncertainty about the observation immediately preceding it. Typical oxidation patterning is not included. Blank cells mean that no features beyond typical were observed.

Elevation from rod bottom (approx. mm)	3A1B16	3A1F05	F35K13 (backward)	F35P17 (backward)
3249		PB, SO	HS	
3289		PB, SO	HS, DS	
3329		PB, SO	DS	
3370		HO, FL		HM
3410	FN, SO		FM	FM
3450				
3490			HS	
3530				HS
3570				HS
3610				
3650	FM, HM	FM	FM	FM
3690	HM			
3731	HM			HS
3771	HM, UPC	HM, UPC	HS	
3811	UPC	UPC	HS, HM	
3851	HM, UPC	HM, UPC	HS	HS
3891				

3.1.2 Typical Waterside Cladding Appearance of M5-Clad Rods

Figure 8 and Figure 9 provide a summary of images representative of the M5 visible features. The M5 rods typically exhibited very light waterside oxide visible in the majority of the images as irregular, somewhat circular patches. Some areas also include an interior circular patch that appears to have peeling oxide, as illustrated in Figure 9(i). Some shallow GTRF marks are visible, along with rod removal scratches. Some localized areas of the M5 rods have thin CRUD layers, presenting with the appearance of a peeling thin skin, as shown in Figure 9(a) and (b). Most of the M5 rods have shallow-to-moderate GTRF marks at the axial locations corresponding to the spacer grid elevations. Also, since not all of the spacer grids in the AREVA-designed assemblies are fixed axially, some GTRF marks have an extended length, as shown in Figure 8(e).

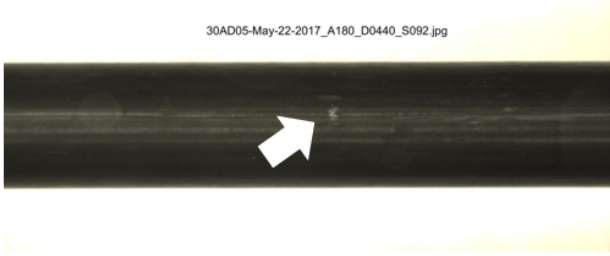

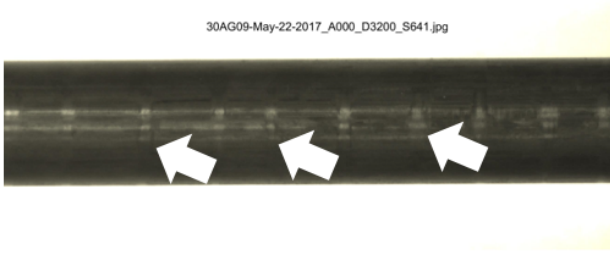
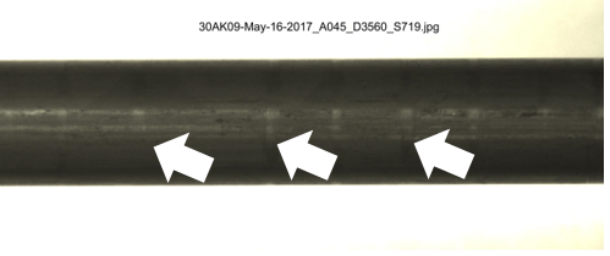
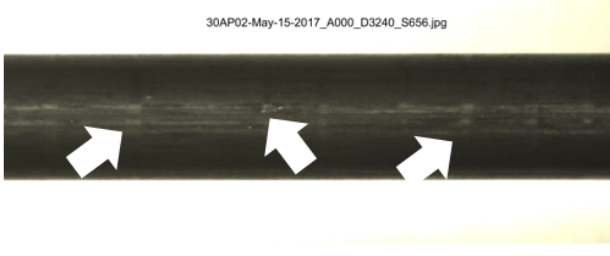
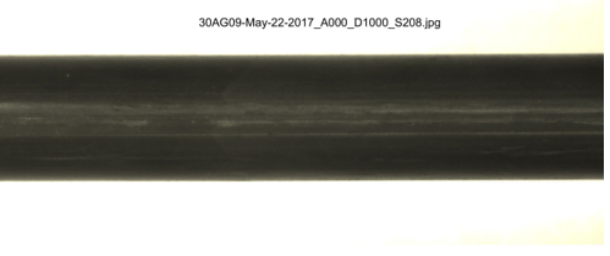
	
(a) Shallow GTRF.	(b) Shallow GTRF.
	
(c) Possible handling marks.	(d) Possible handling marks.
	
(e) Possible handling marks and a shallow GTRF mark.	(f) Region identified in profilometry as having a slightly increased diameter as compared with adjacent sections of the rod; however, no unusual features are visible.

Figure 8. Selected Visual Observations from Assembly 30A.


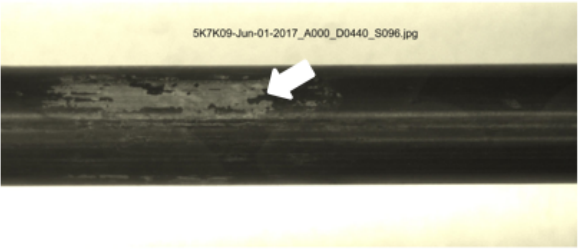
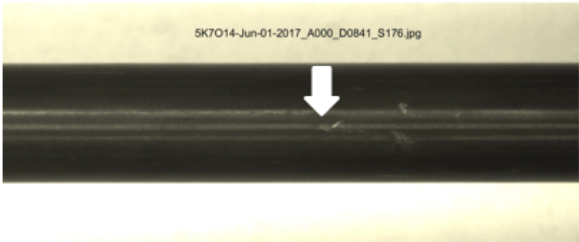


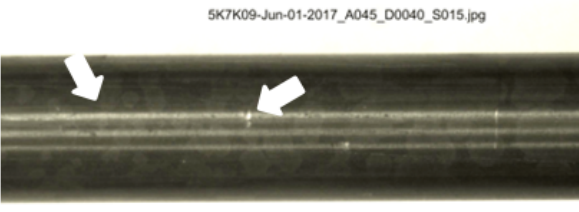
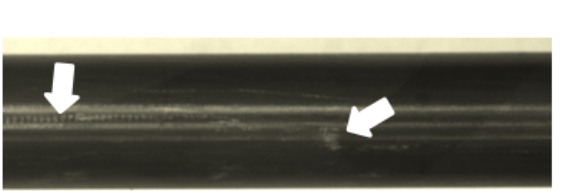
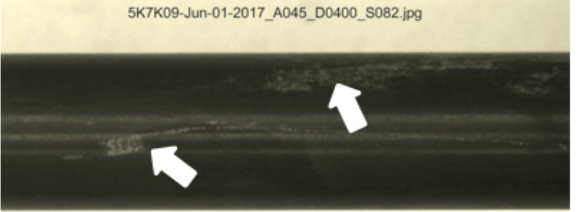
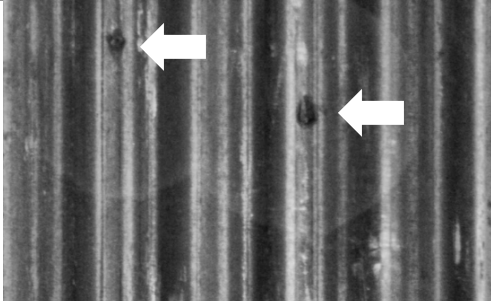
	
<p>(a) Localized CRUD peeling.</p>	<p>(b) Localized CRUD peeling.</p>
	
<p>(c) Shallow GTRF</p>	<p>(d) Shallow GTRF with light oxidation in circular patches.</p>
	
<p>(e) Extended length moderate depth GTRF mark.</p>	<p>(f) Typical light oxidation patches and manipulator scratches.</p>
 <p>A000_D2002</p>	
<p>(g) Typical rod removal scratch and a shallow GTRF mark.</p>	<p>(h) Shallow GTRF with rod removal scratch and peeling CRUD.</p>
	<p>(i) an example of center peeling oxide rings (note the image was extracted from a flattened collage and the axial direction of the rod is oriented perpendicular to the other images shown on this page).</p>

Figure 9. Selected Visual Observations from Assembly 5K7.

3.1.3 Typical Waterside Cladding Appearance of ZIRLO-Clad Rods

The ZIRLO-clad rods have a moderate-to-heavy oxide layer, with some oxide peeling and spalling observed. GTRF marks are present on most rods and range in severity from shallow to deep. Figures 9 to 11 illustrate these details. No visible signs of through-wall cladding damage were observed. Darker regions are present at grid elevations, indicating either CRUD or possibly a thinner oxidation layer (attributed to better heat transfer in those areas due to flow turbulence). A dark band on rod 6U3P16 is clearly a pellet-pellet gap as identified by gamma scan, as noted in Figure 11(h).

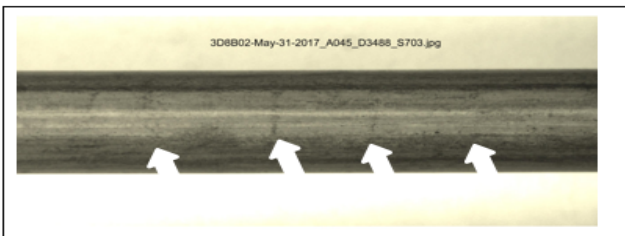


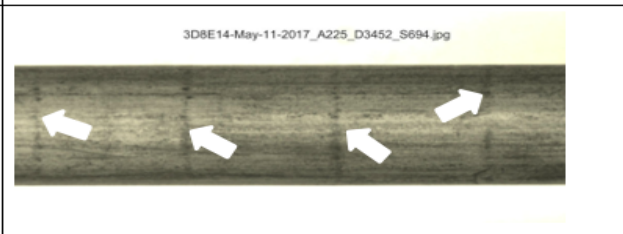

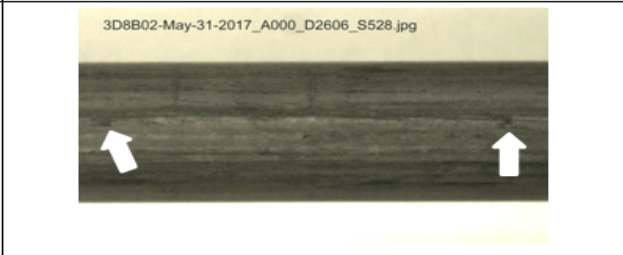
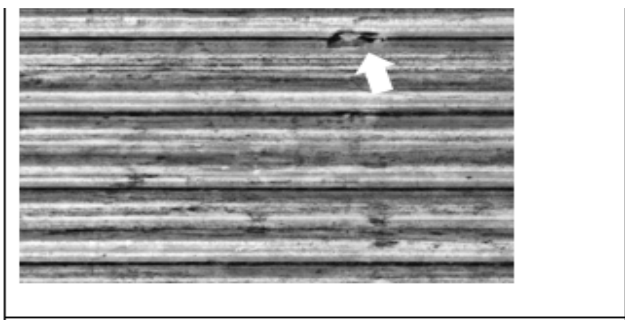
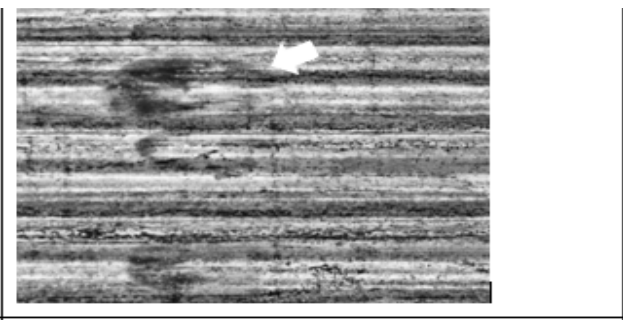
	
<p>(a) Moderate oxide coverage with pellet-pellet interfaces visible.</p>	<p>(b) Possible local corrosion.</p>
	
<p>(c) Pellet-pellet interface near a gamma scan reported axial stack gap.</p>	<p>(d) Typical appearance of pellet-pellet interfaces.</p>
	
<p>(e) Possible rod removal damage with debris.</p>	<p>(f) Shallow GTRF marks.</p>
	
<p>(g) moderate GTRF mark (3D8E14 1204 mm elevation)</p>	<p>(h) Flow markings (3D8B02 3648 mm elevation)</p>

Figure 10. Selected Visual Observations from Assembly 3D8.


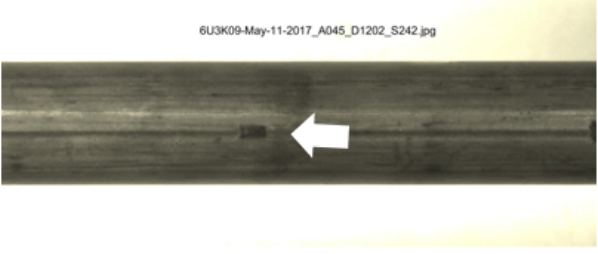
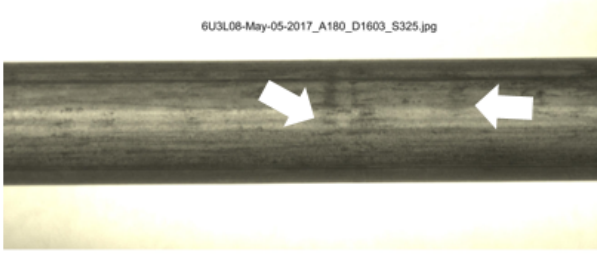



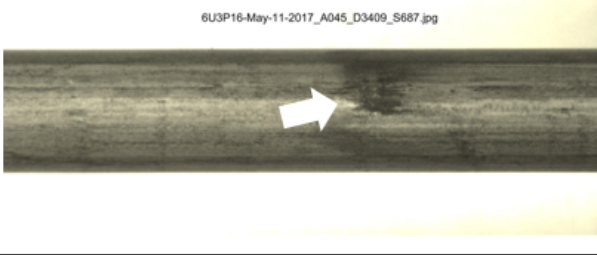
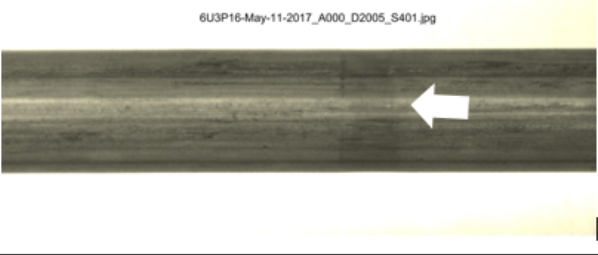
	
(a) Relatively deep GTRF.	(b) Moderate GTRF.
	
(c) Possible handling marks and pellet-pellet interface bands.	(d) Possible handling marks and pellet-pellet interface bands.
	
(e) Rod insertion or removal scratch with shallow GTRF.	(f) Possible handling marks.
	
(g) Flow marking (darker region) associated with turbulent flow around a spacer grid with a shallow GTRF mark.	(h) Banded region is pellet-pellet gap (~5 mm) noted by gamma scan and measured by profilometry.

Figure 11. Selected Visual Observations from Assembly 6U3.

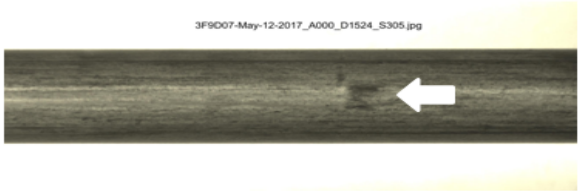
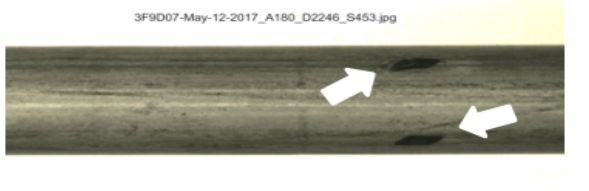
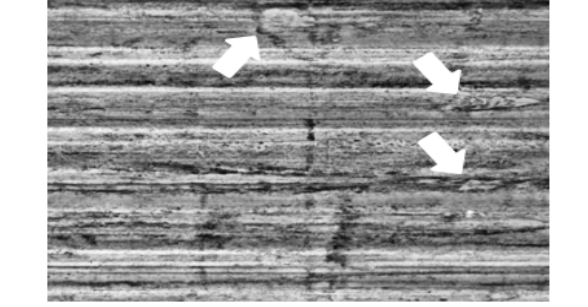
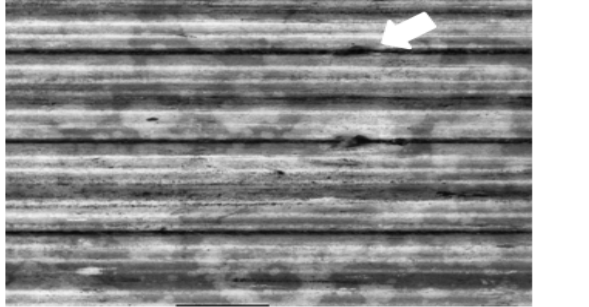
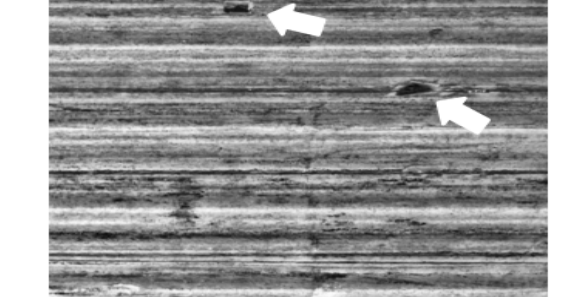
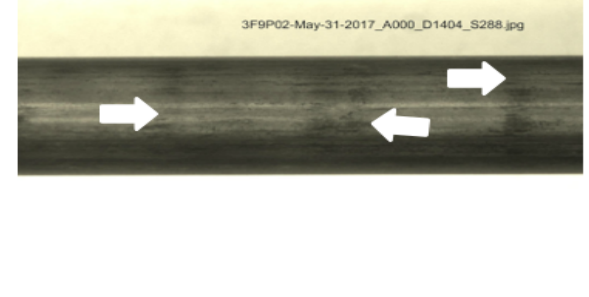

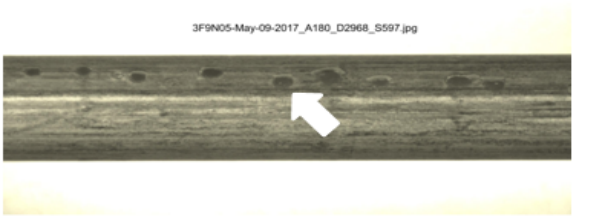

	
<p>(a) Shallow GTRF.</p>	<p>(b) Deep GTRF.</p>
	
<p>(c) Moderate GTRF, completely oxidized, and a patch of locally heavy oxidation.</p>	<p>(d) Moderate GTRF.</p>
	
<p>(e) Moderate GTRF that likely occurred during an early cycle since the mark appears to be partially oxidized.</p>	<p>(f) Typical appearance of pellet-pellet interfaces; this section near a gamma scan-reported axial stack gap (~3 mm).</p>
	
<p>(g) Very shallow apparent GTRF.</p>	<p>(h) Some oxide peeling was noted.</p>
	<p>(i) Unwrapped image (all azimuthal locations at 2246 mm elevation) of 3F9D07, moderate to deep fretting wear.</p>

Figure 12. Selected Visual Observations from Assembly 3F9.

3.1.4 Typical Waterside Cladding Appearance of Zircaloy-4 and LT Zircaloy-4-Clad Rods

Assemblies 3A1 and F35 (Figure 13 and Figure 14) appeared to have the greatest amount of oxide buildup/spalling. No visible signs of through wall damage or large areas of clad degradation were found. A thin layer of CRUD appears to be visible in spalled regions, having the appearance of a black rim around the base of the spalled area, as shown in Figure 13(d). Some areas of significant oxidation have a flake-like appearance, as shown in 14(g) and (h).

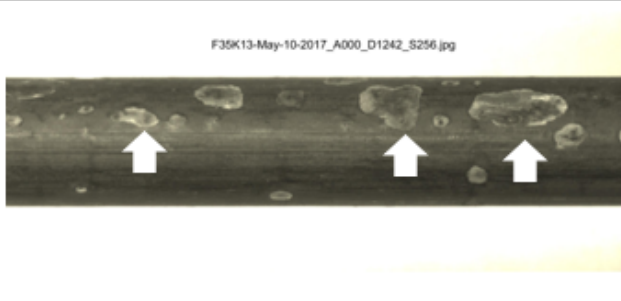
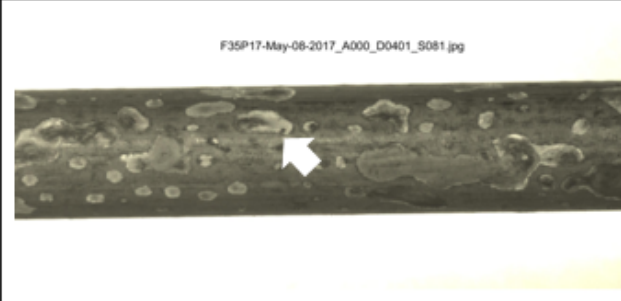

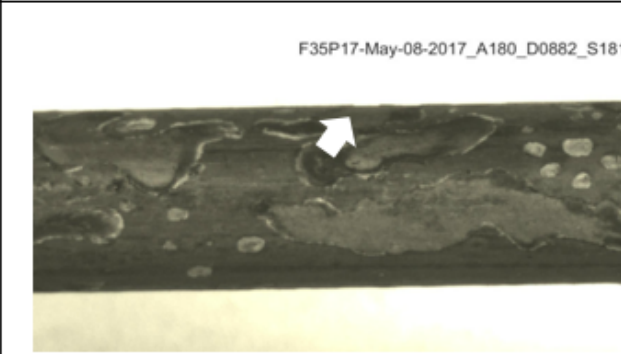

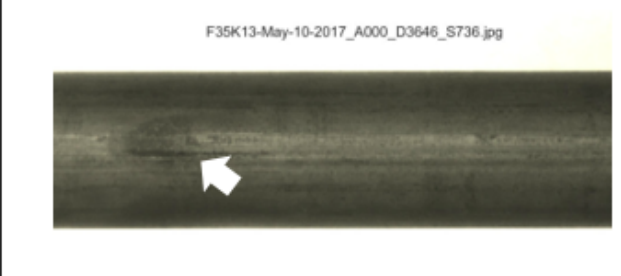
<p>These rods were loaded into the shipping packaging and hot cell backwards and consequently were scanned in the opposite direction from the other sister rods. The distance is measured from the top of the rod rather than the bottom.</p>	
 <p>F35K13-May-10-2017_A000_D1242_S256.jpg</p>	 <p>F35P17-May-08-2017_A000_D0401_S081.jpg</p>
<p>(a) Significant oxide spalling; some pellet-pellet interface bands are visible.</p>	<p>(b) Significant oxide spalling.</p>
 <p>F35P17-May-08-2017_A225_D0602_S123.jpg</p>	 <p>F35P17-May-08-2017_A180_D0882_S181,</p>
<p>(c) Shallow GTRF.</p>	<p>(d) Significant oxide spalling with CRUD; an indication of the oxide thickness is visible at the upper edge of the rod image.</p>
 <p>F35K13-May-10-2017_A090_D2444_S494.jpg</p>	 <p>F35K13-May-10-2017_A000_D3646_S736.jpg</p>
<p>(e) Shallow GTRF.</p>	<p>(f) Flow pattern at a grid elevation.</p>

Figure 13. Selected Visual Observations from Assembly F35.



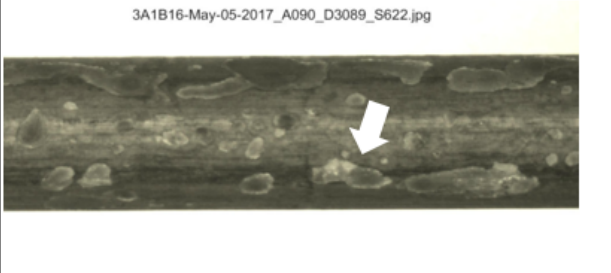
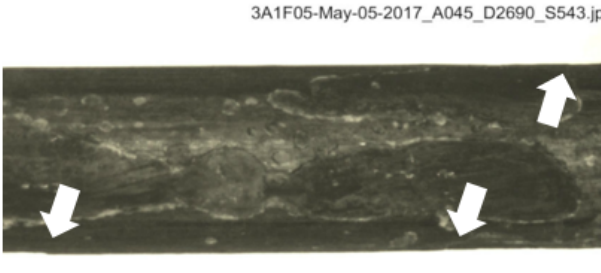

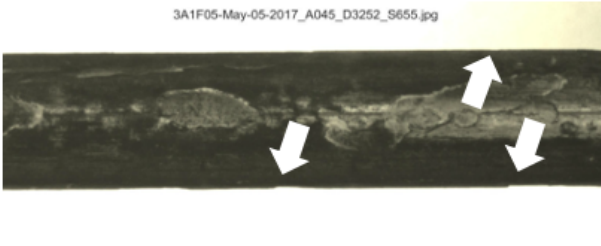

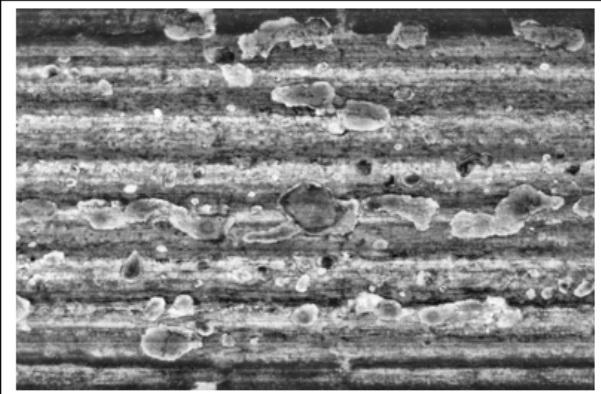
	
<p>(a) Moderate GTRF mark.</p>	<p>(b) Significant oxide spalling with some peeling CRUD.</p>
	
<p>(c) Significant spalling oxide.</p>	<p>(d) Significant oxide spalling with CRUD; an indication of the oxide thickness is visible at the lower and upper edges of the rod image.</p>
	
<p>(e) Flow marking.</p>	<p>(f) Significant oxide spalling with CRUD; an indication of the oxide thickness is visible at the upper and lower edges of the rod image.</p>
	
<p>(g) Unwrapped image (full rod circumference shown at 3252 mm elevation) of 3A1F05, heavy oxide layer with spalling.</p>	<p>(h) Unwrapped image (all azimuthal locations at 3089 mm elevation) of 3A1B16, heavy oxide layer with spalling.</p>

Figure 14. Selected Visual Observations from Assembly 3A1.

3.2 NDE.02 Gamma and Neutron Scanning

Three sets of integrated radiation measurements were completed, including: (1) one-dimensional scans using the ADEPT's sodium iodide (NaI) detector; (2) high resolution gamma spectroscopy using a high-purity germanium (HPGe) detector, and (3) gamma and neutron measurements using a fission/ionization chamber-based fork detector. The HPGe and fork detector measurements were performed for the NNSA, Office of Nonproliferation and Arms Control (NPAC), and are summarized here for completeness.

Figure 15 compares the four normalized gamma count rates data sets for sister rod 30AE14 measured using the three different detectors (the HPGe measurements include two gamma counts, ^{137}Cs and total). For reference, the normalized predicted average assembly axial burnup profile is also plotted. There is very good agreement in the general trends and locations of spacer grid burnup depressions. Up to 7% differences were observed between the fork gamma counts and the HPGe total gamma counts near the rod bottom, likely due to the fact that a collimator is not used in the fork measurement, but even so, there is good agreement between all three detectors in the higher burnup regions of the rod. Radiochemical assay of selected rod locations will provide additional definitive (within measurement uncertainty) burnup measurements.

The following sections describe the results afforded by each gamma/neutron measurement campaign.



Figure 15. Comparison of Gamma Count Rates Collected by Three Different Detectors for Sister Rod 30AE14: HPGe, fork, and NaI. The Normalized Predicted Average Assembly Axial Fuel Burnup is also Plotted for Reference.

3.2.1 One-dimensional sodium iodide gamma scanning

A one-dimensional gamma scan (resolution of ~1mm obtained using a long, adjustable-width collimator) was completed using the ADEPT on all 25 rods in 2 energy ranges: 400 to 800 keV for examination of the fuel stack and 1,100 to 1,600 keV for examination of the structural components. ADEPT's special purpose sodium iodide (NaI) detector is 6 inches long and ½ inch in diameter for maximum detection of the signal from the region of interest. The NaI detector was selected so that ADEPT can maximize the gamma signal at the expense of energy resolution.

The count time used for sister rod measurements was 20s each except for the first rod, which was scanned for only 15s. The signal from this lower scan time was later scaled for comparison with the other rods. The longer scan time was chosen after the results from the first rod were obtained because the facility's operating schedule limited the rod change intervals, and the longer scan time allowed for maximum data collection in the allocated time. During the scan, the rod was translated axially, but it was not rotated. The two energy ranges were collected simultaneously. Data were collected in 1 mm increments along the axis of the rod and were indexed to the bottom of the rod.

The results of the gamma scanning length measurements are summarized in Table 4. The activity signal exhibited the expected behavior without any sign of fission product accumulation or migration. The axial profile of the rods was as expected, and depressions in burnup were easily observed at the spacer grid locations. Figure 16 through Figure 22 provide graphs of the gamma scanning data and summarize the measurement data obtained for the sister rod. The graphs plot the rod activity as a function of axial length, and although the rod burnup cannot be estimated based on the gamma scans, the axial profile is analogous to the axial burnup of the fuel. In addition to the gross gamma counts measured for each sister rod, the graphs also plot the utility-predicted assembly average burnup (where available), normalized and scaled to a corresponding average gamma count, for comparison with the measured axial profiles. As a first order approximation, the gamma total counts tend to trend with the average pin burnup; however, other factors such as cooling time influence the total gamma counts.

The rod length was measured by the ADEPT apparatus during the gamma scanning as a part of the rod indexing. The uncertainty of the overall rod length is determined by the positional accuracy of the ADEPT resolvers, 0.5mm, derived through repeated measurements of the same rod and applicable over the total length of the fuel rod (on the order of 3,900 mm). The uncertainty of the gamma-determined lengths/locations is influenced by both the uncertainty associated with the gamma collimator width (1 mm) and the positional uncertainty of the ADEPT apparatus (0.5 mm). The total uncertainty of gamma-determined lengths/locations is therefore conservatively estimated as the absolute value of the sum of the individual uncertainties, 1.5 mm (the movement uncertainty depends on rod friction with the drive and resolver wheels and is difficult to characterize).

The overall rod length measurement (see Section 3.3) facilitated the measurement of axial rod components that do not produce a gamma signal (e.g., bottom-end plug, top-end plug). Because of the very weak signal, the bottom-end plug's length (location) was determined by the start value of the pellet stack. The top-end plug length (location) was determined by subtracting the end value of the spring location from the rod's length.

Both the fuel stack length and the plenum length (spring) were inferred from the gamma scan data. The plenum region has a much lower gamma signature, since there is no fuel in that region. However, the gamma source provided by the fission gases and activation of the plenum spring allow the plenum region to be differentiated from the top-end plug. Note that none of the sister rods have a lower plenum spring. The top and bottom of the pellet stack produce a gamma scattering effect that is observable as a sharp reduction in the scan count rate.

Since the dish and chamfer regions are large enough to provide a significant drop in gamma source term, the gamma scan allows for differentiation of every pellet in the rod. This is visible in the full-length rod

graphs (Figure 16 through Figure 22) as chatter in the data. Zooming into a specific segment of the rod, as illustrated in Figure 23, provides differentiation of each pellet. An estimate of the number of pellets in each fuel rod was determined by spectral methods in which the gamma scanning data were examined for shallow reductions in the fuel stack gamma count associated with pellet end geometry (chamfers and dishes). The average pellet length was determined by dividing the pellet stack length by the number of pellets counted. Since partial pellets are not used, the fractional estimated number of pellets was rounded off to the nearest integer value.

Because each pellet is visible, axial gaps in the stack (either pellet-pellet gaps or pellet end capping, which is material missing from the ends of the pellet resulting from die or handling issues during manufacture) can also be observed, and the gap length can be estimated. Where the gamma count is significantly lower than observed for normal pellet end effects, the data on each side of the count rate reduction were examined, and the length of the pellet-pellet gap was estimated. The results are summarized in Table 5. The uncertainty of the gap measurements is evaluated as ± 1.5 mm since the observation is a product of both rod length and gamma measurements. However, as discussed previously, the ± 0.5 mm resolver uncertainty is distributed over the entire length of the rod, and the local uncertainty for the gap measurement is nearer to ± 1 mm. Since some of stack gaps reported in Table 5 are 1 mm in length, the uncertainty of ± 1 mm implies that these stack gaps may not exist, or they may be as large as 2 mm. Likewise, for all locations where a gap was not indicated, there is a possibility that a 1 mm gap exists but was not detected.

No serious structural defects were noted in any of the rods because of the gamma scanning; some small fuel stack gaps were observed, and the largest was estimated as 5 mm on sister rod 6U3P16.

Table 4. Results of gamma scanning grouped by rod type (± 1.5 mm, except for rod length, ± 0.5 mm).

Rod	Average pellet length (mm)	Estimated number of pellets in the stack	Average pellet length for type (mm)	Average pellet number for type	Bottom plug length (mm)	Top plug length (mm)	Plenum length (mm)	Average plenum length for type (mm)	Fuel stack length (mm)	Average fuel stack length for type (mm)	Overall Rod Length (mm)	Average rod length for type (mm)
30AE14	10.28	357	10.24	359	14.0	9.4	184	182.2	3,674	3,676.6	3,881.4	3,882.3
30AK09	10.19	361			14.0	9.9	178		3,679		3,880.9	
30AD05	10.26	358			14.0	9.7	185		3,677		3,885.7	
30AG09	10.23	359			13.0	10.1	185		3,674		3,882.1	
30AP02	10.25	359			14.0	9.2	179		3,679		3,881.2	
6U3O05	9.89	372	9.89	372	20.0	12.1	182	178.7	3,676	3,679.1	3,890.1	3,889.8
6U3I07	9.87	373			20.0	13.0	175		3,680		3,888.0	
6U3M03	9.91	372			20.0	11.7	178		3,682		3,891.7	
6U3M09	9.88	372			18.0	13.4	183		3,675		3,889.4	
6U3K09	9.90	372			19.0	11.9	179		3,679		3,888.9	
6U3L08	9.88	373			19.0	12.8	175		3,683		3,889.8	
6U3P16	9.92	371			20.0	12.3	179		3,679		3,890.3	
5K7C05	10.17	362	10.14	363	14.0	9.3	180	180.8	3,680	3,679.3	3,883.3	3,883.4
5K7K09	10.16	362			14.0	9.6	185		3,675		3,883.6	
5K7O14	10.13	364			14.0	9.8	176		3,684		3,883.8	
5K7P02	10.11	364			14.0	8.9	182		3,678		3,882.9	
3A1B16	9.95	370	9.93	371	10.0	9.1	193	191.5	3,680	3,682.0	3,892.1	3,893.2
3A1F05	9.92	371			10.0	10.3	190		3,684		3,894.3	
3F9D07	9.86	374	9.86	374	20.0	11.6	174	176.7	3,684	3,682.0	3,889.6	3,890.6
3F9N05	9.84	374			20.0	12.6	178		3,681		3,891.6	
3F9P02	9.87	373			19.0	12.6	178		3,681		3,890.6	
3D8B02	10.04	367	10.05	367	20.0	12.2	174	174.5	3,683	3,685.0	3,889.2	3,891.3
3D8E14	10.05	367			19.0	12.4	175		3,687		3,893.4	
F35K13	13.74	269	13.67	270	9.5	9.0	178	175.0	3,690	3,694.5	3,886.5	3,888.0
F35P17	13.60	272			10.5	8.0	172		3,699		3,889.5	

Table 5. Fuel stack gaps observed through gamma scanning (± 1 mm).

Rod*	Location from rod bottom (mm)	Estimated gap width (mm)
30AD05	3,635	1
	3,646	2
	3,657	2
	3,667	1
	3,678	2
6U3P16	2,010	5
6U3K09	453	1
5K7P02	448	1
5K7C05	755	2
	948	1
	1,559	2
3F9D07	462	2
3F9P02	1,303	2
	1,313	1
	1,373	2
3D8E14	1,403	3
F35P17	1,655	3

*Rods not listed did not have an observed stack gap (within the stated ± 1 mm uncertainty).



Figure 16. Gamma Scans for Sister Rod from Fuel Assembly 30A.

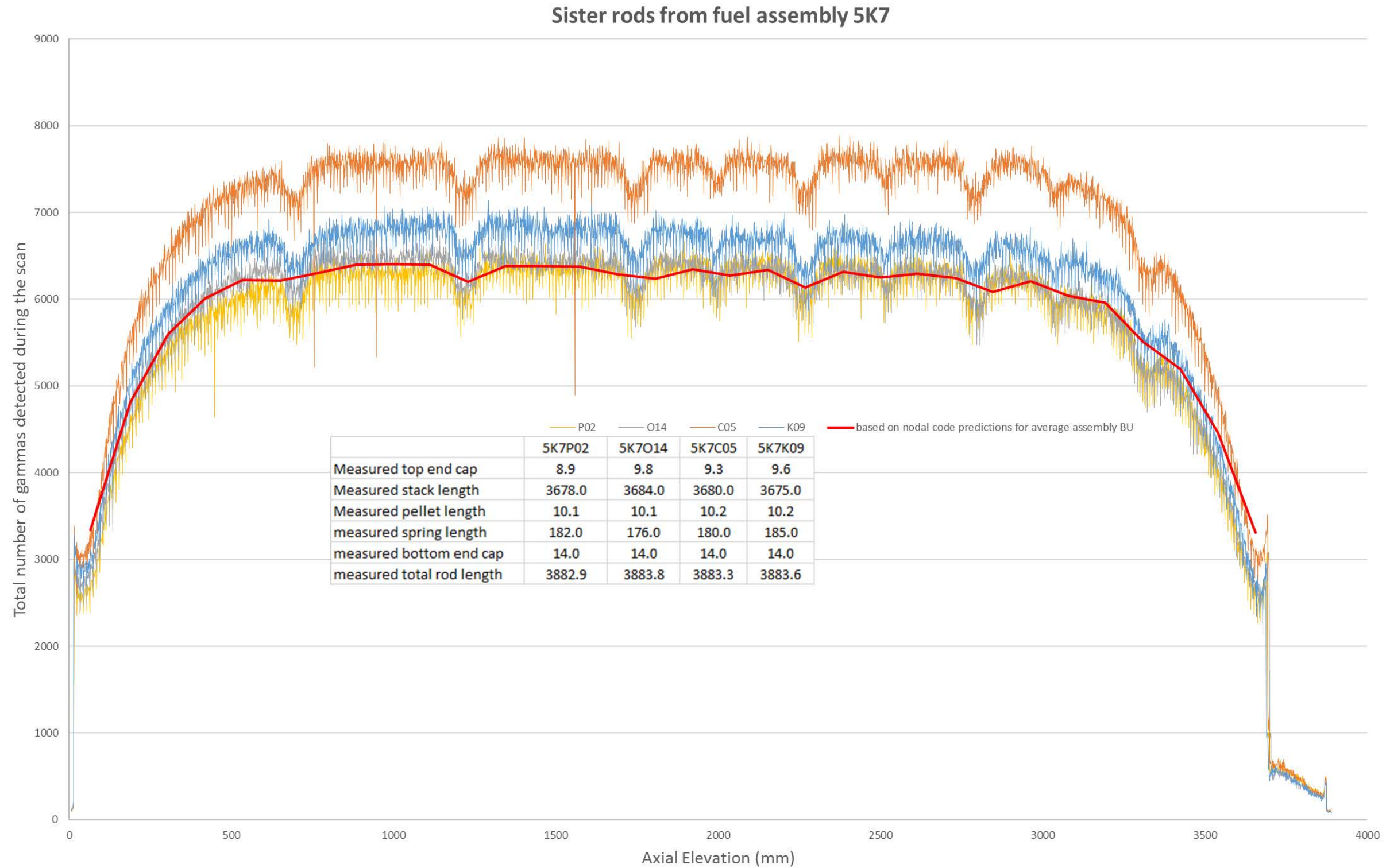


Figure 17. Gamma Scans for Sister Rod from Fuel Assembly 5K7.

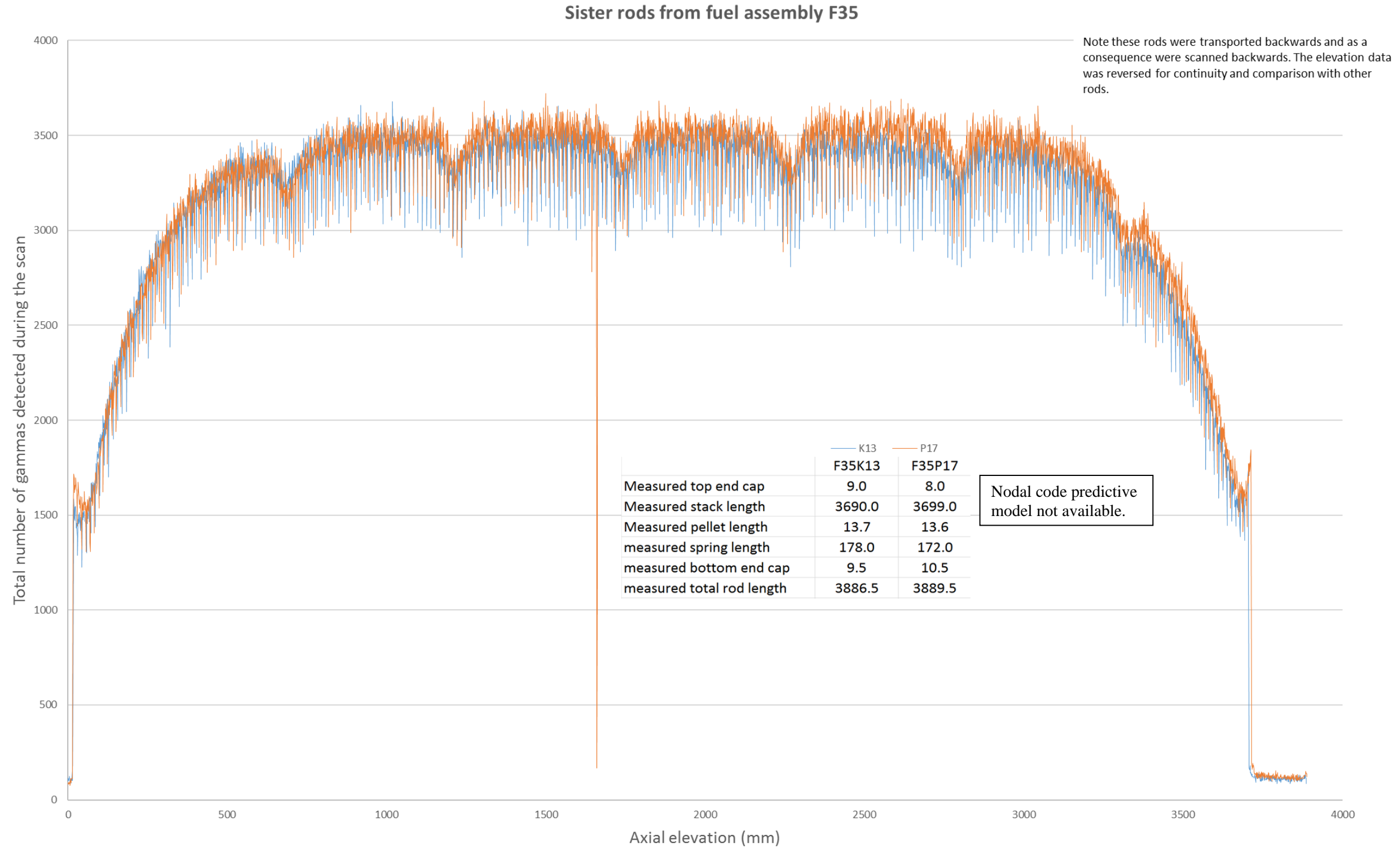


Figure 18. Gamma Scans for Sister Rod from Fuel Assembly F35.

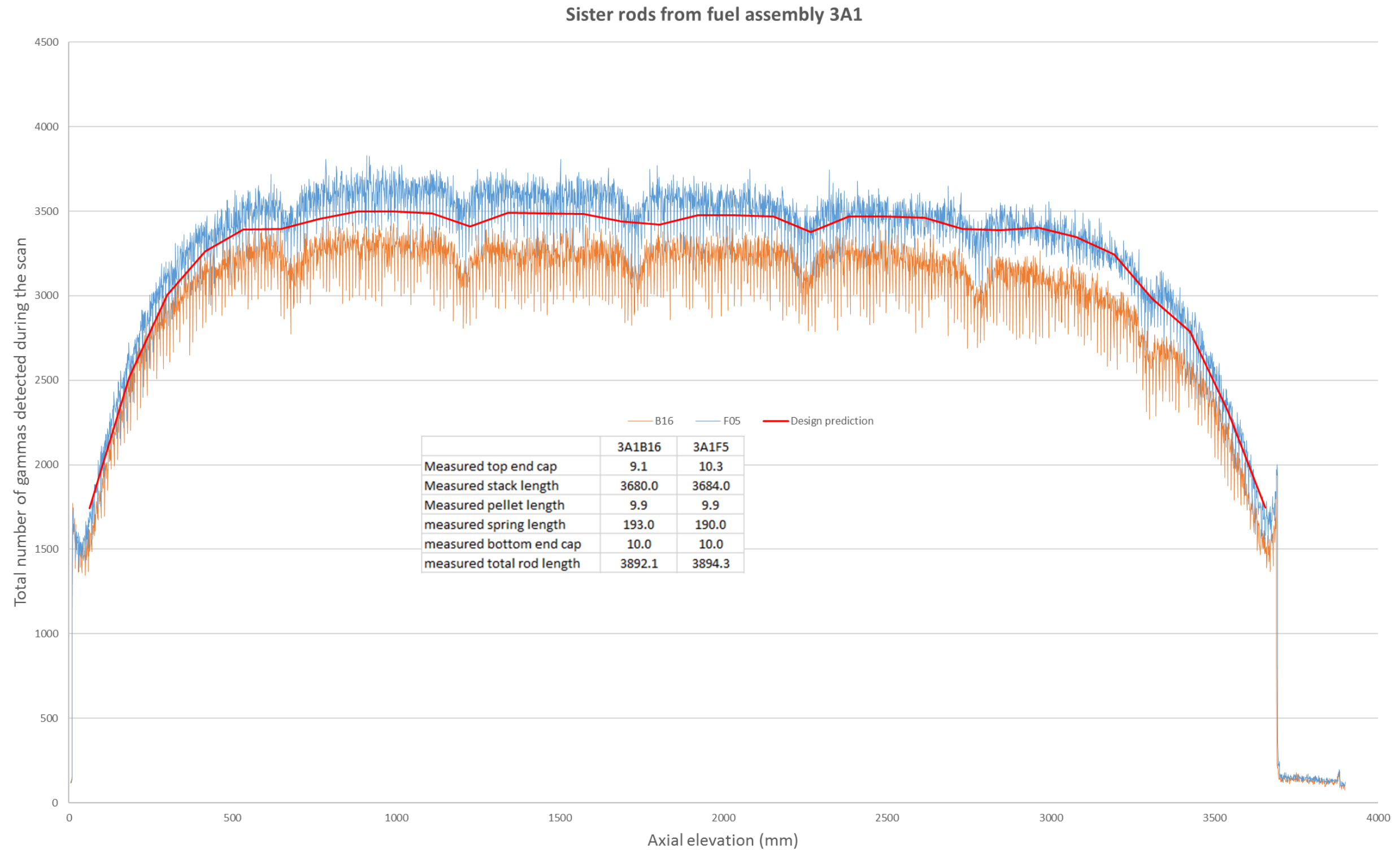


Figure 19. Gamma Scans for Sister Rod from Fuel Assembly 3A1.

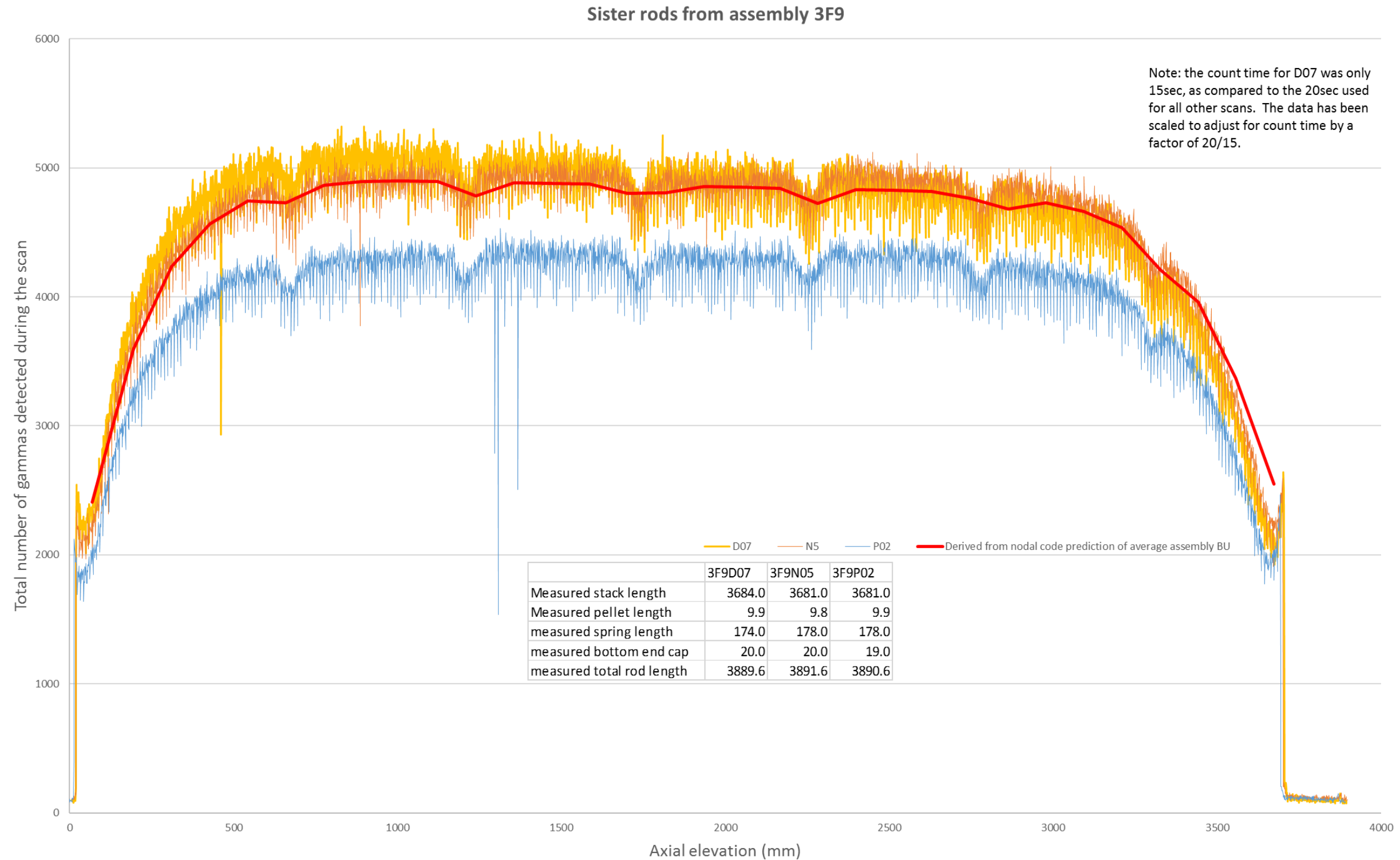


Figure 20. Gamma Scans for Sister Rod from Fuel Assembly 3F9.

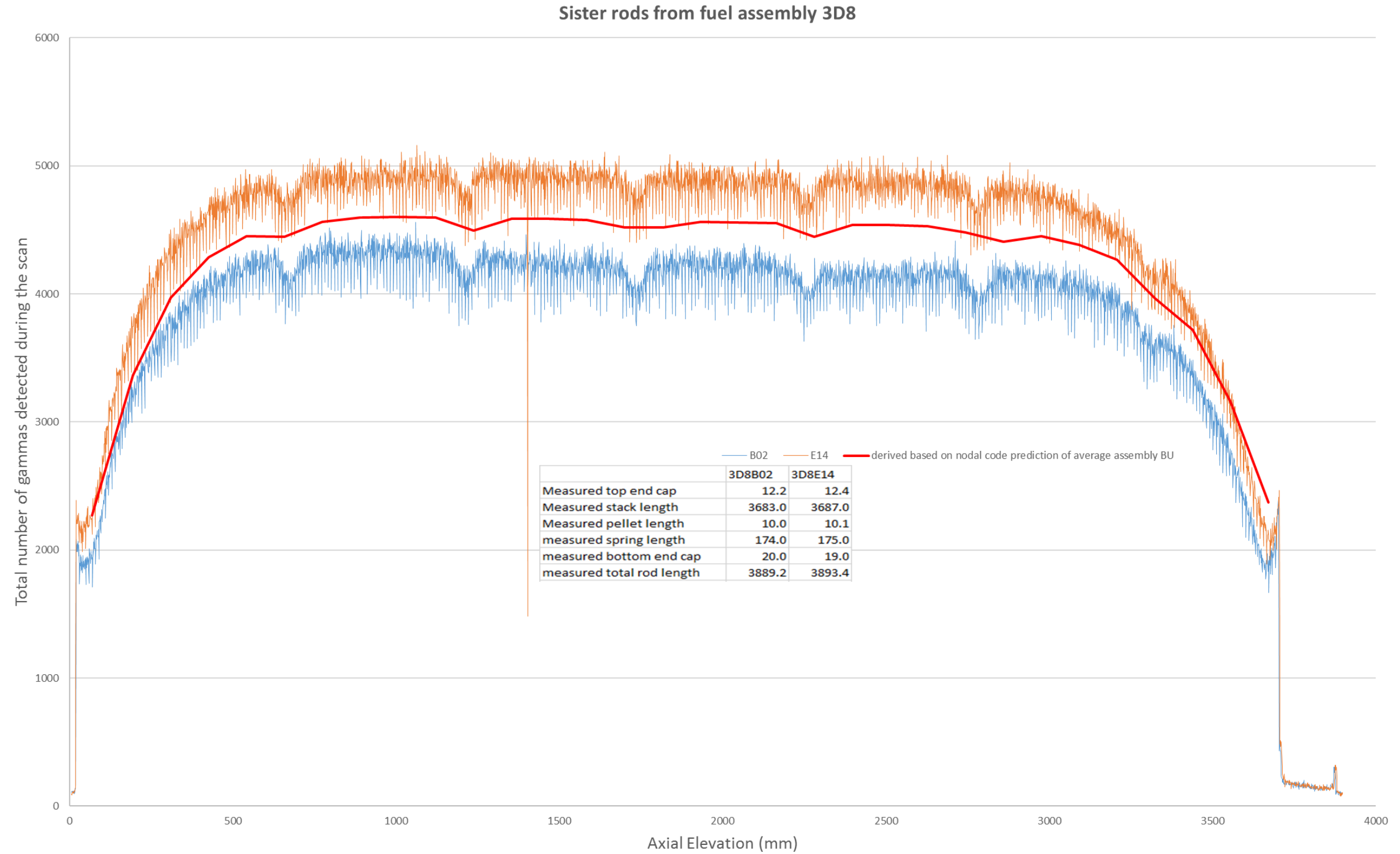


Figure 21. Gamma Scans for Sister Rod from Fuel Assembly 3D8.



Figure 22. Gamma Scans for Sister Rod from Fuel Assembly 6U3.

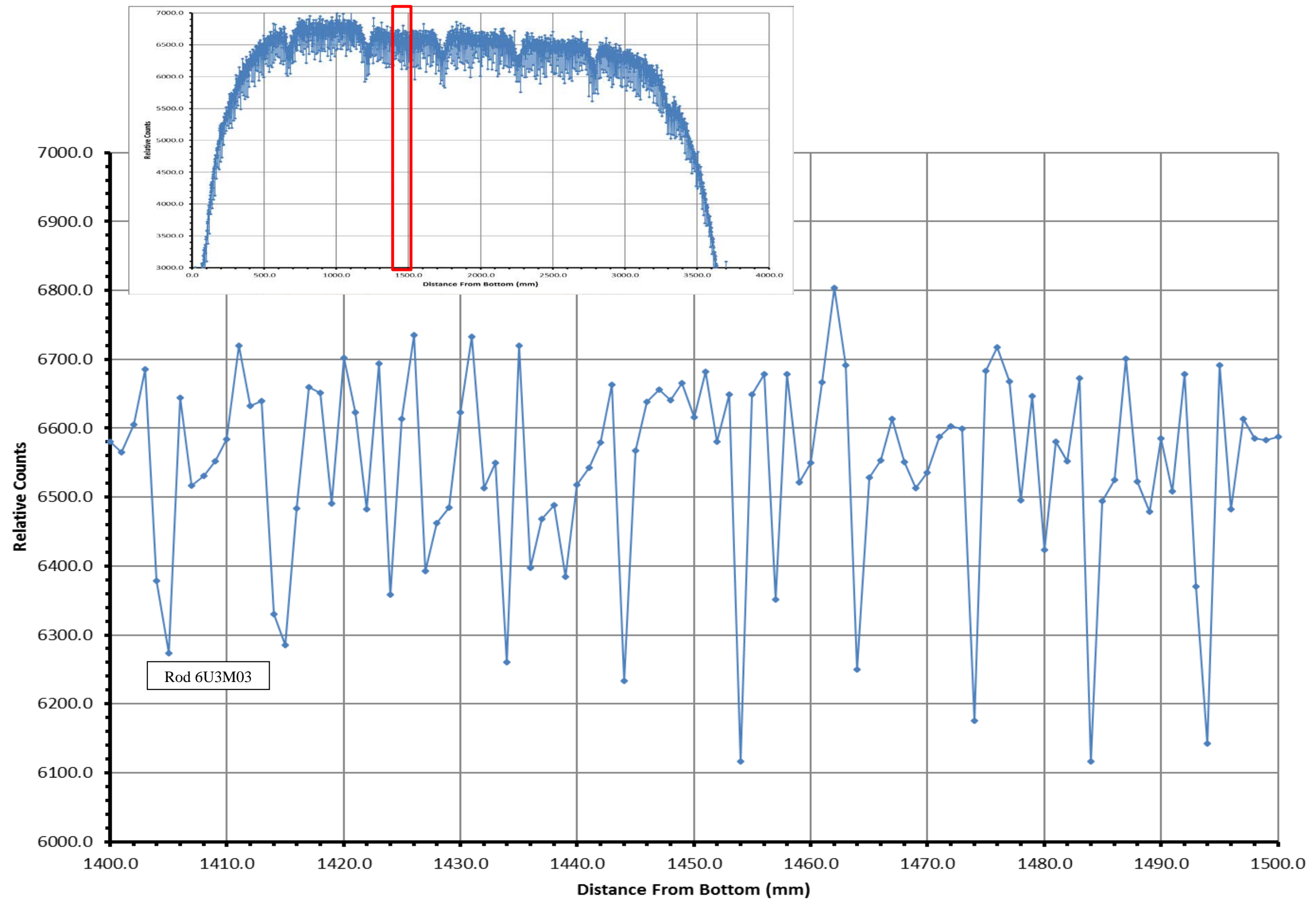


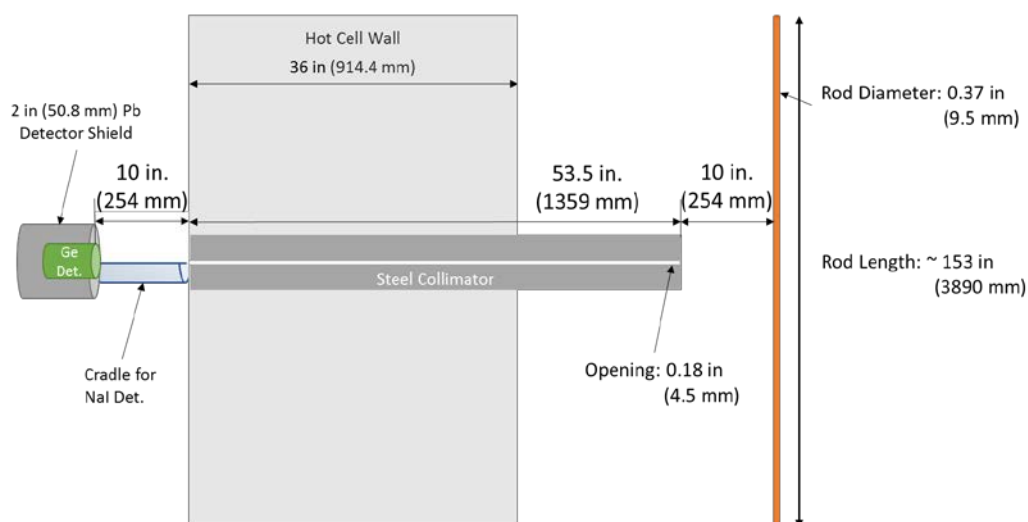
Figure 23. Typical Pellet Ridging on a Fuel Rod Observed Via Gamma Scanning; Scales are Magnified to Show the Detail. The Typical Pellet is Approximately 10mm Long.

3.2.2 HPGe Detector Scanning

International nuclear safeguards use NDE techniques to verify the declared characteristics of SNF assemblies. These characteristics usually include initial fuel enrichment, assembly average burnup, and irradiation history. A recurring requirement for the use of high-resolution gamma spectroscopy as a technique for safeguards verification is the calibration of the gamma-ray peak intensities or areas to the isotopic content of the fuel at discharge. Typically this is accomplished through simulation or measurement of several known SNF assemblies. Two questions are raised by these methods of calibration: (1) to what extent are the simulation codes sufficiently validated against real spectroscopy measurements, and (2) how can the burden of independent SNF calibration measurements taken during a facility inspection be reduced? Measurement of the sister rods using the HPGe detector provides a unique opportunity to begin addressing both calibration concerns. This section describes a preliminary evaluation of the spectra performed thus far. A report on the HPGe scanning with a catalog of the spectra collected can be found in Smith et al. [4].

Over a period of 5 weeks, all 25 sister rods were scanned using a high-resolution HPGe gamma spectrometer. The measurement dwell time was restricted by the working hours of the hot cell facility, and only two rods could be scanned in 24 h, one during the daytime and the second overnight. Scans could not be performed over the weekends, but the time was used to take long background measurements of the hot cell with and without a dummy rod. The purpose of the dummy rod is to get a better estimate of how much background from the hot cell is directly blocked by the SNF rod. Background subtraction is preferred because it reduces the possibility of overestimating the background contributions when doing the spectrum analysis.

Figure 24 and Figure 25 illustrate the detector measurement geometry and configuration for the HPGe measurement campaign. The detector chosen for the measurements is a large p-type semi-planar HPGe manufactured by Canberra Industries (model BE3820), also known as a broad-energy germanium detector (BEGe). The collimator's NaI detector cradle cannot be removed, and because the HPGe detector is larger in diameter than the NaI detector, it does not fit into the NaI cradle. Therefore, it had to be placed 10 in (254 mm) from the face of the collimator. The sliding wedge aperture of the collimator was opened to approximately 0.18 in (4.5 mm) such that the full diameter of the rod was in the field of view.



The steel collimator extends through and beyond the hot cell concrete wall to within 10 in of the fuel rod. A cradle is built onto the end of the collimator for the NaI detector measurements and could not be removed for the HPGe detector measurements.

Figure 24. Diagram of the Measurement Geometry for the HPGe Campaign.

Since the area of the HPGe detector used is much larger than the aperture, it is the collimator that determines the count rate. A two-inch thick modular lead shielding and positioning assembly was used to shield potential room background and improve measurement reproducibility.

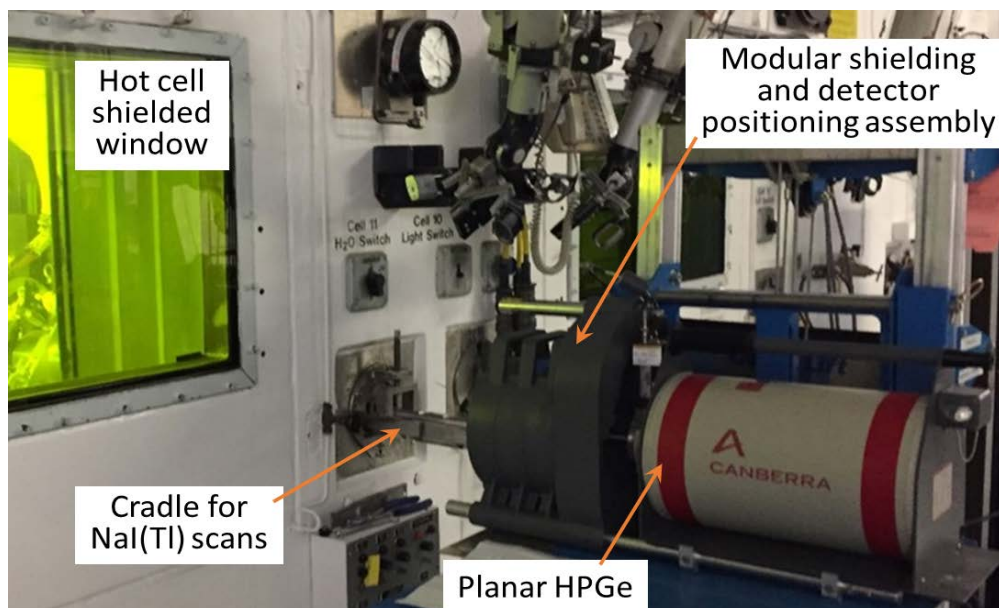


Figure 25. Picture of the HPGe Detector during Spectroscopy Measurements.

The IFEL was equipped with a CANBERRA DSA 2000 multichannel analyzer and CANBERRA Genie 2000 software V3.2.1 to perform the data acquisition. The digital signal processing settings were configured to acquire a spectrum of 8,192 channels and an energy range from 0-3,045 keV. Live time correction was enabled, so a reference pulser/source was not used to correct for dead time.

For the axial scans, 700 spectra were collected in discrete steps of approximately 5.56 mm along the entire length of the fuel rod (3,890 mm). Typically, an 18s live time was used for scans performed during the workday, and a 50s live time was used for scans performed overnight. These settings were selected as a tradeoff between count time and dead time to ensure that two rods could be measured each calendar day. The elapsed exam time was measured in terms of live time, so it varied somewhat with incoming count rate.

The individual spectrum from each measurement point was collected using a user-defined prefix, the date, and the position of the rod during that measurement file naming scheme. The data collected associated with sister rod 30AD05 are discussed in this summary report to illustrate the results obtained. For a complete discussion of the data and results, please see Smith et al. [4].

Assembly 30A has average declared burnup of 52 GWd/MTU and was discharged from the reactor core 6–7 years ago. It was expected that the spectra for 30AD05 would be dominated by the three long-lived fission products that emit gamma rays: ^{134}Cs , ^{137}Cs , and ^{154}Eu . Figure 26 illustrates the energy spectrum of a single point selected from the 700 axial point spectra acquired with the HPGe detector along the length of rod 30AD05 using the PeakEasy Software program [5]. The summed spectrum shown in Figure 26 clearly shows these isotopes. Additionally, the radiation-induced x-rays from uranium are clearly visible. Above the 1,596 keV ^{154}Eu gamma ray, the spectrum is dominated by small peaks from random coincidence summing.

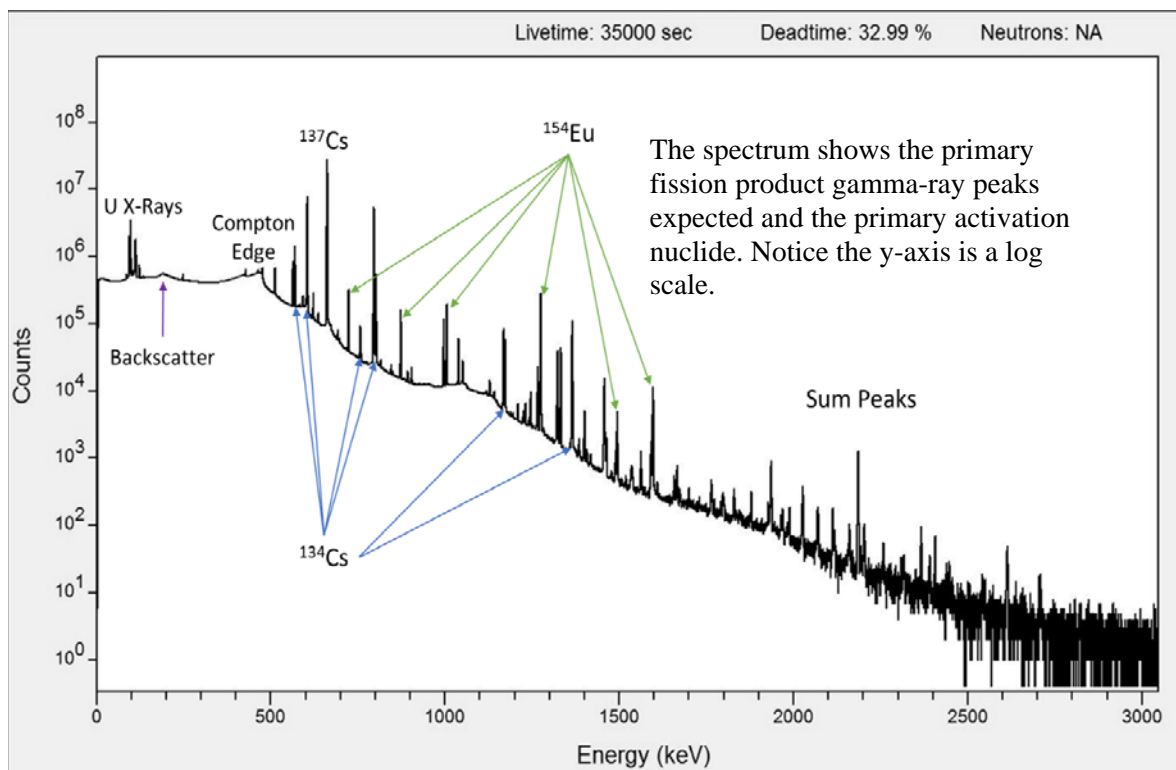


Figure 26. HPGe Sum Spectrum of Sister Rod 30AD05.

From the axially collected 700 point spectra, individual dead time-corrected total counts from an energy region of interest (ROI) can be plotted against the axial rod position where the data were acquired. It is expected that the total count rates will be approximately constant (within statistics) along the central portions of the sister rod that contain fuel (drop off is expected at the ends of the fuel stack), consistent with an efficient in-reactor use of the fuel. The fuel rod plenum region is dominated by ^{60}Co from the irradiation of the spring in the plenum.

Figure 27 shows the axial scan gross counts for sister rod 30AD05 for a ROI around the 661.6 keV peak from ^{137}Cs . Spacer grid depressions in burnup are visible as reductions in the total count rates. The overall burnup profile measured using the HPGe detector agreed very well with the results achieved using the NaI detector. However, the sliding wedge aperture of the collimator was only opened to 0.04 in (1 mm) for the NaI scans. Because of the narrow width of the collimator used with the NaI detector, count rate reductions could be seen in the data corresponding to the transition between individual fuel pellets (see Section 3.2.1). Because the HPGe detector has a lower efficiency and required a much larger aperture opening, this granularity was not achieved.

With the support of the NNSA's Office of Global Material Security, additional measurements were performed to determine if scintillator detectors could be used for burnup calculation. A coaxial HPGe detector, a 2×2 -inch NaI detector, and a lanthanum bromide (LaBr_3) detector were used to measure sister rod 3D8B02 at a single location (2,000 mm from the bottom) using essentially identical detector positions. The coaxial HPGe and BEGe detectors were in the same position as the BEGe for the previously described measurements. The NaI and LaBr_3 were placed in the cradle at respective distances of $2\frac{1}{8}$ inches and 2 inches from the steel collimator. The rod was measured with each detector for a live time of 30 minutes.

Figure 28 shows the difference in the spectra produced by each detector as analyzed using PeakEasy [5]. The peaks from ^{134}Cs and ^{154}Eu could not be distinguished with the NaI spectra, so quantitative analysis of that spectrum was not possible.

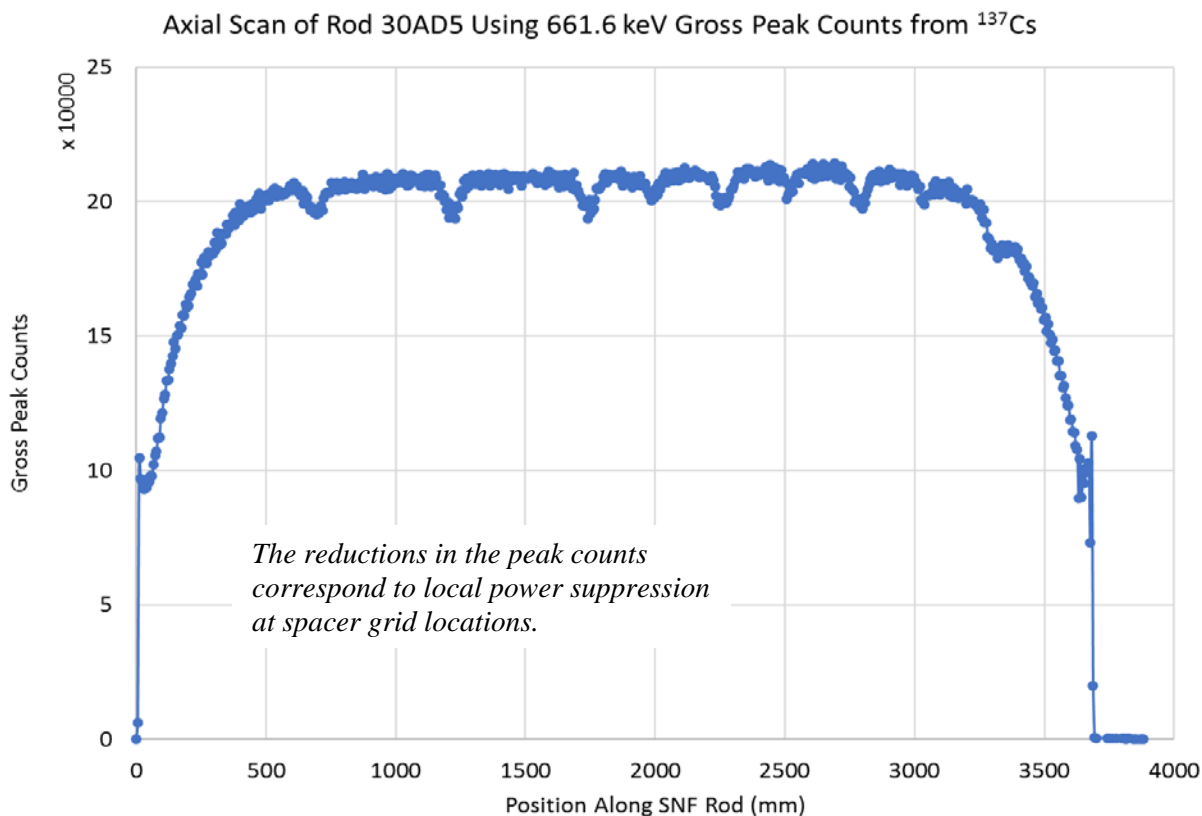


Figure 27. HPGe-derived Axial Scan of Sister Rod 30AD05 Using the Gross Peak Counts from the 661.6 keV Peak of ^{137}Cs .

A preliminary quantitative analysis of the 30-minute spectra obtained from the BEGe, the coaxial HPGe, the LaBr_3 detectors, and the summed spectrum from the full-length axial scan of 3D8B02 was completed. The mass ratios calculated from the spectra were run through simulations in INDEPTH [6] at a constant power of 40 MW/MTU to generate a calculated burnup and cooling time. The mass ratios used in the INDEPTH simulations were calculated from the average activity ratios of ^{154}Eu and ^{134}Cs with respect to ^{137}Cs . The net count rate was determined using the ROI fit analysis in PeakEasy and the branching ratios from the TORI [7] database.

A comparison of the simulation results from INDEPTH using the HPGe 30-minute measurement as the reference is shown in Figure 29. The results from the LaBr_3 detector were not consistent with the results from the HPGe detectors. In particular, the cooling time calculated from the LaBr_3 detector differed by about 50%. The results from the HPGe detectors were consistent, with only a 3% difference for the predicted cooling times and a 9% difference in predicted burnup. A comparison to the known characteristics of the rod will be completed at a later date.

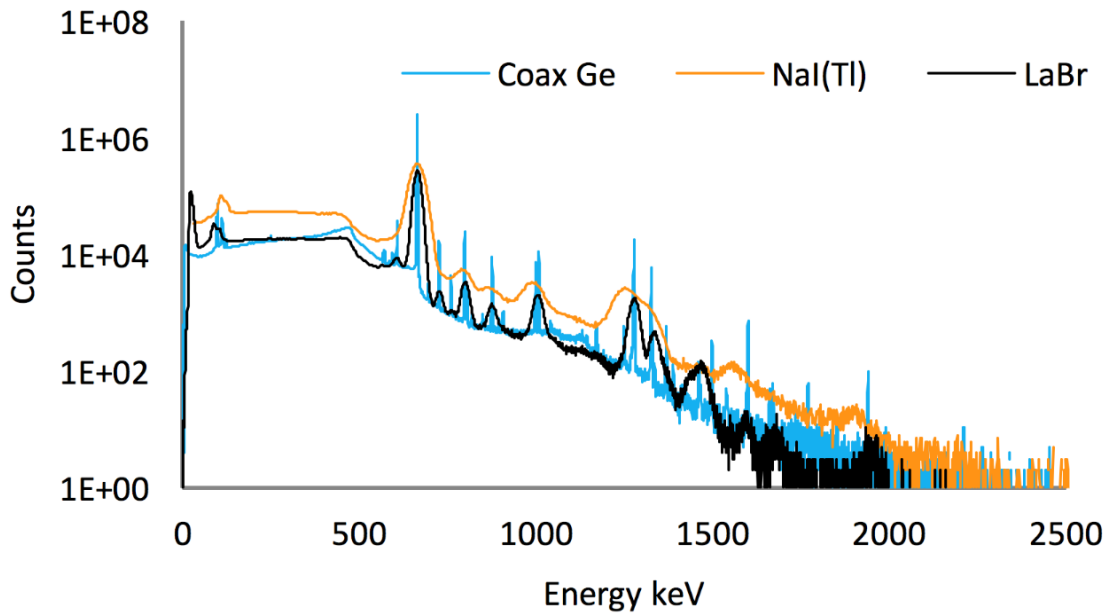
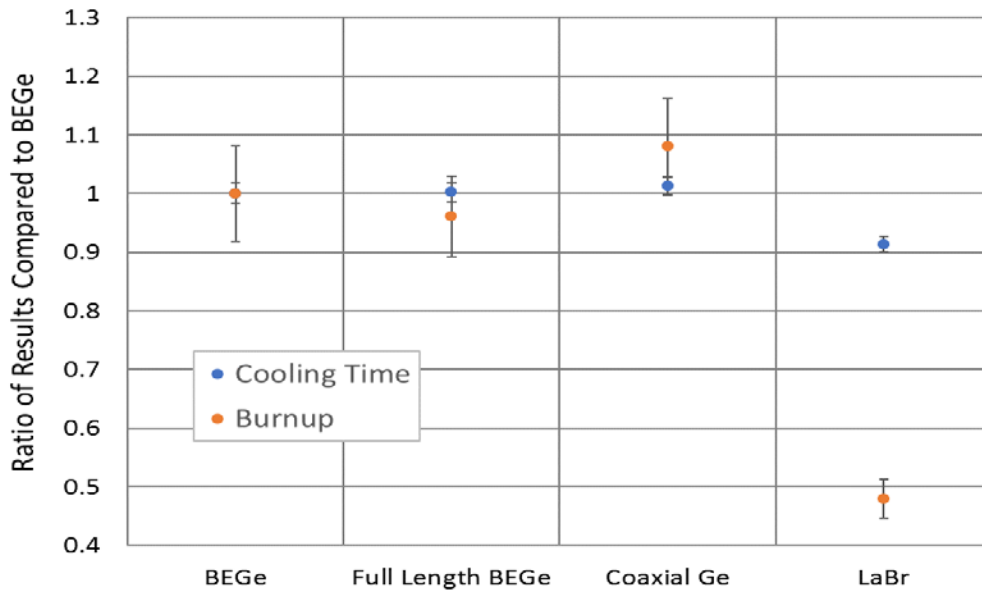


Figure 28. Superimposed Spectra of Coaxial Ge, NaI, and LaBr₃ Detectors.



INDEPTH [6] simulation used flat power of 40MW/MTU and mass ratios were calculated from the gamma spectra.

Figure 29. Comparison of the Cooling Time and Burnup of Rod 3D8B2 by Detector Type.

3.2.3 Fork Detector Gamma and Neutron Scanning

The fork detector is one of two primary instruments routinely used for spent fuel safeguards inspections by international safeguards authorities, including the International Atomic Energy Agency (IAEA) and Euratom [8]. Two fork detectors, (1) a standard fork detector and (2) a modified fork detector with alternate neutron and gamma detectors, were used to perform measurements. The fork detector can be used to verify fuel assembly burnup and cooling time and to check for removal or substitution of fuel rods from a subject fuel assembly.

Figure 30. depicts the fork detector, and Figure 31 illustrates the detector measuring a spent fuel assembly in a utility spent fuel pool. Each of the two tines of the fork detector includes two fission chambers and one ionization chamber. The signals from the four fission chambers (two in each tine) are combined to measure two neutron energy groups: one designed for measuring fast neutrons, and the other for measuring thermal neutrons. Similarly, the two ionization chambers (one in each tine) are combined to form one gamma measurement. The number of neutrons emitted by a spent fuel assembly is proportional to approximately the 4th power of the assembly average burnup, and the gamma emission is highly dependent on the fuel's cooling time.

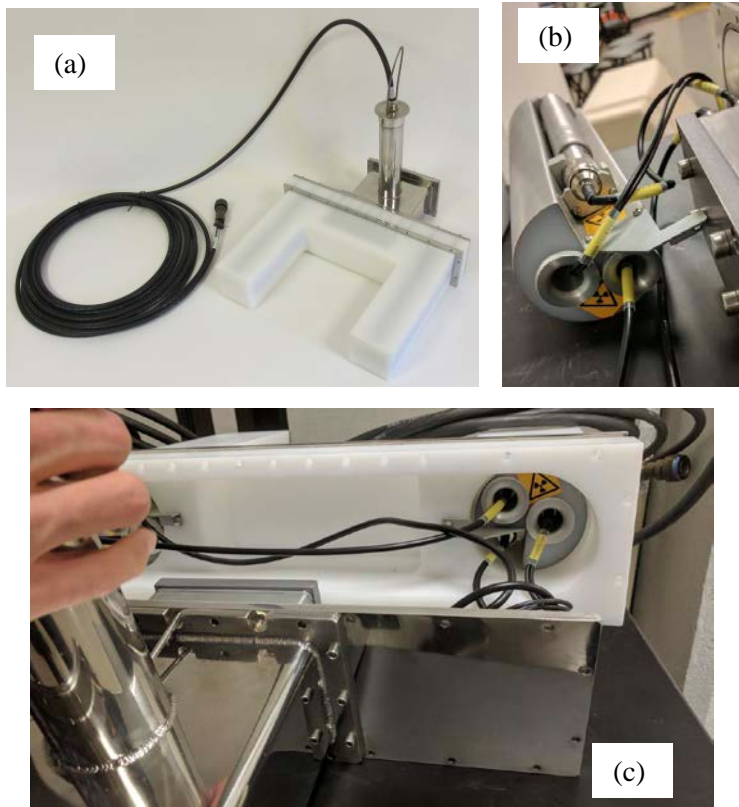


Figure 30. (a) Fork Detector Head, (b) Fission and Ionization Chambers, (c) Rear View of Fork Detector Head (with Back Plate Removed).



Figure 31. Measurement of a Spent Fuel Assembly in a Pool Using a Fork Detector [8].

Before the fork detectors were loaded into the hot cell, they were tested and calibrated in ORNL's Radiation Standards Calibration (RASCAL) facility (Figure 32) using a strong ^{252}Cf neutron source ($\sim 3.0\text{E}8$ neutrons/s) and ^{137}Cs gamma source ($\sim 1,000$ curies and $\sim 3.2\text{E}13$ photons/s).

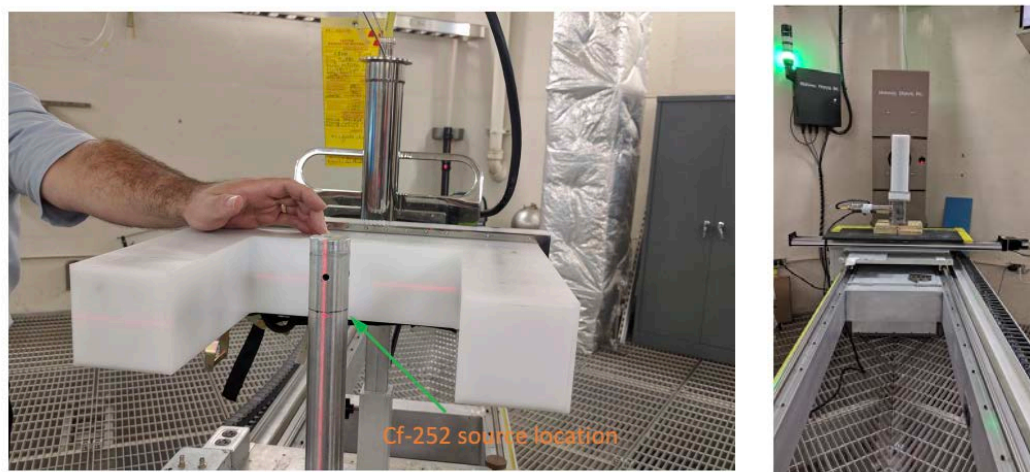
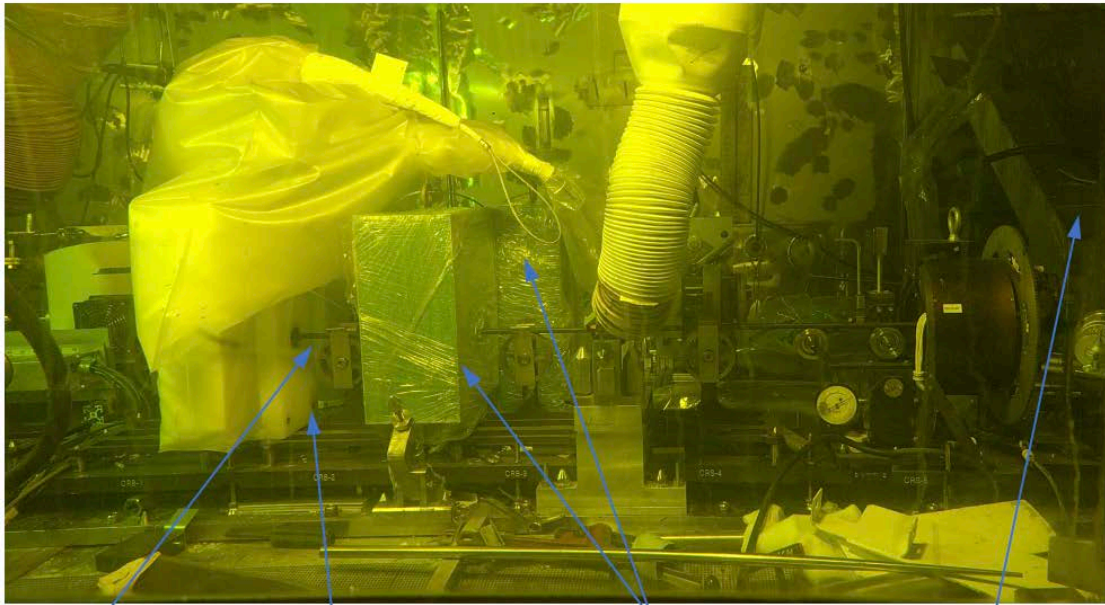


Figure 32. Set Up for Calibrating the Fork Detectors at ORNL's RASCAL Facility.

After the calibration, the fork detectors were loaded into ORNL's IFEL hot cell to measure the sister rods. The fork detectors were first used to measure the individual fuel rods (~ 13 feet long) in both moderated and unmoderated conditions. Figure 33 shows the measurement of a single fuel rod in the moderated configuration. Polyethylene (poly) blocks were used as moderating material. Aluminum liners were used to prevent transfer of the poly to the fuel rods. For most rods, measurements were taken at 12 locations along the rod length to capture the variations of the axial burnup profile. ORNL's ADEPT system was used for rod positioning. The specific location of the rod relative to the fork detector was always known. No collimator was used in this measurement, so neutron and gamma signals from other parts of the fuel rod cannot be ignored. Such effects can be accounted for using simulations.

After single rod measurements were completed, the sister rods were placed into several different arrays to mimic the neutron and gamma interactions between the rods in a fuel assembly, including 2×2 , 3×3 , and 5×5 arrays. For the 5×5 array, two partial defect scenarios were created and tested. Figure 34 (left) shows the fork measurement of the 5×5 rod array. Four sets of aluminum support structures were specially designed and manufactured to assemble the rods into arrays. Great care was taken to avoid any potential damage to the fuel rods during assembly. The movement of each rod was carefully tracked and recorded, and each sister rod was tagged when used in the arrays.

To create the partial defect scenarios, stainless steel rods were used in place of the fuel rods in the 5×5 array. Measurements were performed with this array at 6 axial locations along the length. Measurements were taken with 4 stainless steel rod substitutions and with 8 stainless steel rod substitutions. Figure 34 (right) shows the 5×5 array from the north end with eight fuel rods missing from view. Short stainless-steel rods (4.5 feet long instead of 13 feet long) were used in this work for easier maneuvering in the hot cell. The short rods also accommodated measurement of an additional configuration in which part of the array had fuel rods missing without substitutions. Measurements were performed at 6 locations along the length of the array.



A spent fuel
rod

Poly block for moderation

Borated poly blocks with
Cd liner for shielding

Near end of the fuel rod
storage casks

The fork detector was enclosed in two layers of poly bags to reduce contamination. A poly block (white) was placed around the fuel rod to provide neutron moderation. Two borated poly blocks with cadmium liners were placed beside the detector to block neutrons emitted from other sister rods stored in the hot cell.

Figure 33. Set Up for Measuring a Full-Length Sister Rod Using a Fork Detector in IFEL Hot Cell.

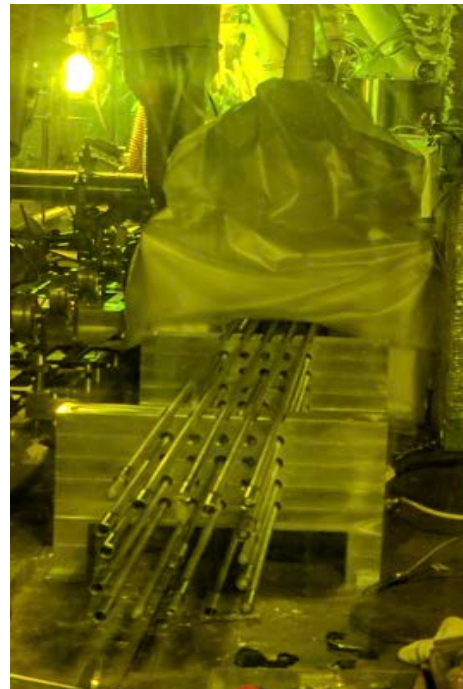


Figure 34. Set Up for Measuring a 5×5 Array of 25 Full-Length Spent Fuel Rods Using a Fork Detector at ORNL's IFEL Hot Cell with All Locations Filled with Sister Rods (Left) and with 8 Partially Vacant Locations (Right).

Figure 35 depicts the normalized fork neutron and gamma count rates (with background subtracted) along the length of sister rod 30AE14. The axial burnup profile derived from the average assembly burnup prediction for rod 30AE14's parent assembly was also included for comparison. The axial fuel rod burnup profile is not available. Both the neutron and gamma count rates followed the expected trends, increasing from the bottom of the fuel rod to the center section. Due to space restrictions in the hot cell, the fork detector was not able to reach the upper end of the fuel rod.

There is good agreement between the gamma measurement and the axial burnup in the middle of the fuel rod. Similar trends were observed in other fuel rods. As mentioned previously, SNF neutron emissions trend with the 4th power of the burnup, while gamma emissions are somewhat linear with burnup. This is evident in the steeper neutron slope shown in Figure 35. In theory, there should be a very close agreement between the fork detector gamma count rates and the predicted axial burnup profile. Different factors can contribute to the discrepancies observed, for example: (1) the predicted assembly average axial burnup plotted in Figure 35 is somewhat different from the sister rod burnup and doesn't capture localized neutron spectra differences; and (2) a collimator was not used for the fork measurements, allowing gammas from other sections of the fuel rod to contribute to the signal. During safeguards inspections, fork measurements are usually performed only at the middle of a fuel assembly, without using any collimator.

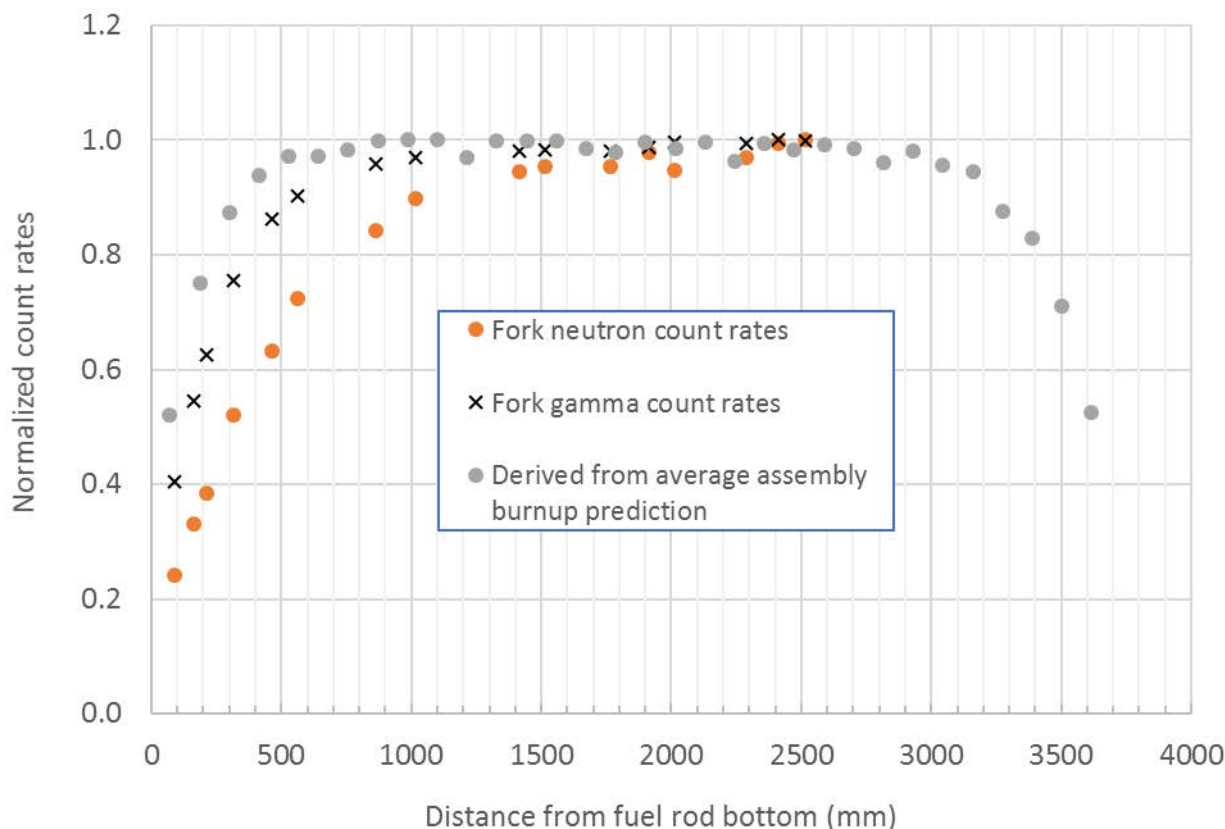


Figure 35. Normalized Fork Neutron and Gamma Count Rates along the Length of Fuel Rod 30AE14.

Figure 36 compares the fork count rates and the corresponding calculated neutron and gamma source intensities (not presented here) based on the fuel design data and operating histories of the 9 sister rods. The measured count rates are based on the fork measurement at the 1500 mm position near the axial

center of the rod. The measured count rates are expected to be linear with the calculated source intensities for all sister rods because the measurement geometry was kept the same for all fuel rods. As seen in Figure 36, the measured fork neutron and gamma count rates trend very well with the corresponding calculated source intensities. The calculations were performed based on the reported fuel burnup and cooling time. These results demonstrate that the fork detector was able to verify fuel burnup and cooling time.

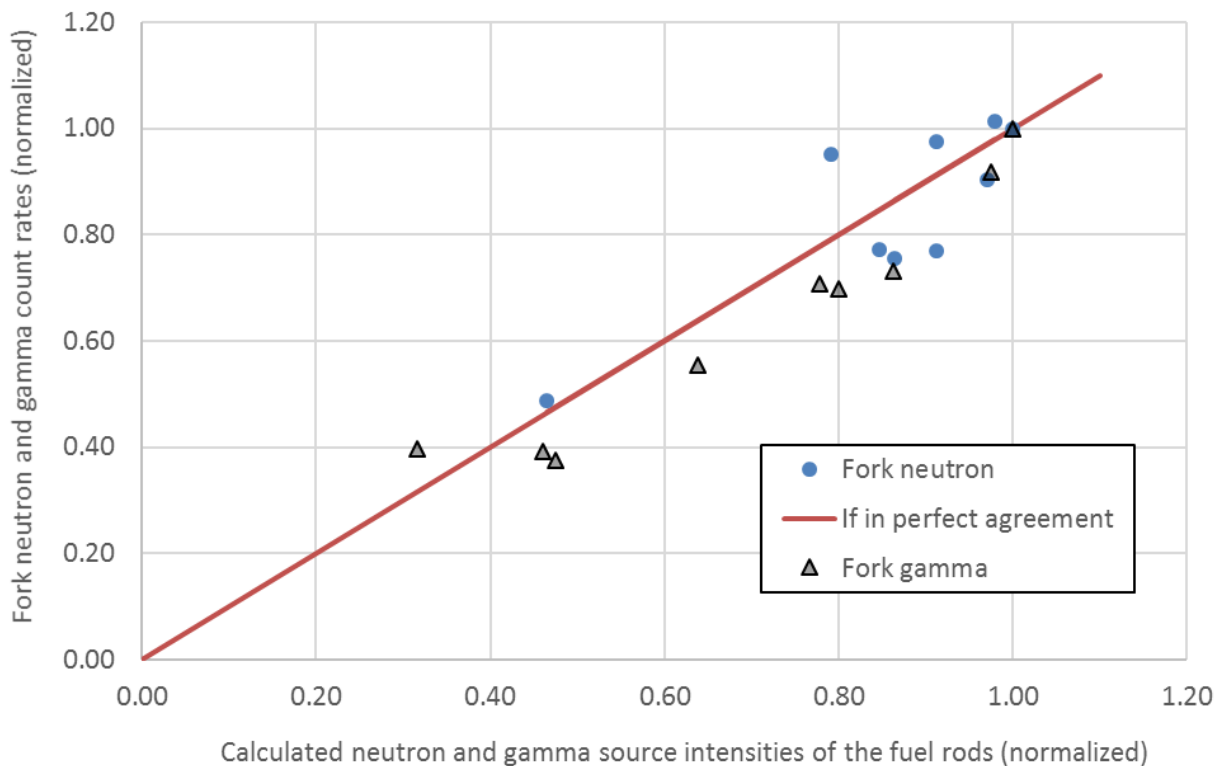


Figure 36. Comparisons between the Fork Gamma and Neutron Count Rates with the Corresponding Calculated Neutron and Gamma Source Intensities in 9 Fuel Rods.

For measurements in which stainless steel rods were substituted for four fuel rods, an 8–14% reduction in the neutron count rate and a 13–16% reduction in the gamma count rate were observed as compared to the rates of the full 5×5 array, depending on the axial locations where the array measurement was performed. When eight fuel rods were replaced with stainless steel rods, the reduction in the neutron count rate was 19–28%, and the reduction in the gamma count rate was 31–34%. It should be noted that the fuel rods that were replaced with steel rods had shorter cooling times than the majority of the rods in the array.

In-air spent fuel fork detector measurements present unique challenges. The sister rods provided a unique opportunity to test the fork detector's in-air measurement performance and to validate ORNL software for use by IAEA and Euratom to predict fork neutron and gamma count rates in real time. The initial results show that the fork detector performs well in air, its gamma count rates are consistent with other data sets, it can verify reported burnup and cooling time of the fuel, and it is sensitive to the quantity of fuel material. A separate report documenting fork results and applications should be available in the near future.

3.3 NDE.03: Fuel Rod Overall Length

Before each gamma scan, the length of each sister rod was measured as needed for machine indexing. A calibration rod was measured before and after each scan, along with two measurements of the rod length. The average measured overall lengths for the 25 sister rods are reported in Table 4.

Because ADEPT is indexed using the overall rod length, each rod is measured every time it is placed on ADEPT. The table value represents an average of the rod measurements. At least two measurements were made of each rod, one before and one after gamma scanning. The average measurement was used to calculate the locations of the rod's internals. As more measurements are taken, they will be considered in the reported rod length and uncertainty, and the results will be updated as needed.

3.4 NDE.04: Eddy Current Examinations

Two eddy current examinations are planned: (1) a campaign using traditional eddy current methods to measure oxide/CRUD thickness and remaining cladding thickness and to identify flaws, and (2) a campaign to measure the hydrogen content of the cladding. The first of these is scheduled for the October 2017 timeframe, and the second was completed late in July 2017. Some preliminary data are provided in Section 3.4.1.

3.4.1 F-SECT Measurements

EPRI performed Frequency-Scanning Eddy Current Technique (F-SECT) measurements on the sister rods in the IFEL hot cell. Due to industry expectations for higher fuel reliability and the emphasis on determining fuel reliability margins, EPRI has advanced development of NDE characterization techniques capable of quantifying hydrogen content, zirconium alloys' residual wall thickness, and oxide/CRUD thickness. These techniques could be deployed poolside at a nuclear power plants. The F-SECT has been developed specifically to nondestructively estimate cladding hydrogen content using refined eddy current techniques based on point measurements of electrical conductivity. It has been tested in hot cell and poolside environments on zirconium alloys, including channel box, water rod, spacer, and fuel cladding.

The F-SECT system measures eddy current impedance over a range of frequencies which provides data at different penetration depths into the cladding. The probe must stay in contact with the surface of the rod at the measurement location for approximately 2 seconds to allow for the completion of the 24-frequency sequence and acquisition of the electrical impedance versus frequency spectrum. The presence of ferromagnetic CRUD can influence the measured electric conductivity, and as a consequence, it influences the measured lift-off and estimated hydrogen content. Therefore, EPRI has also developed a magnetic saturation technique to compensate for the effects of ferromagnetic CRUD. Usually PWR fuel does not have a substantial amount of ferromagnetic CRUD, and the sister rods in particular are not expected to have ferromagnetic CRUD.

The objective of the F-SECT measurement campaign was to locally measure the electrical conductivity of the sister rod cladding to estimate the local cladding hydrogen concentration. At the same time, the F-SECT measurement includes point measurements of the combined zirconium oxide and CRUD thickness (the *lift-off*). An F-SECT measurement bench was designed and installed in the IFEL hot cell to accommodate the work. The bench included an integral magnetic loop coil and an F-SECT probe mounted on a swing arm to allow the fuel rod to be freely moved as shown in Figure 37.

A total of 19 sister rods were successfully measured over 3 consecutive days, including ZIRLO, M5, Zirc-4, and LT Zirc-4 clad rods. The detailed results will be reported by EPRI and are summarized here for information only. At this writing, only oxide/CRUD thickness data are available; the estimated hydrogen concentration data are expected to be available in November 2017.

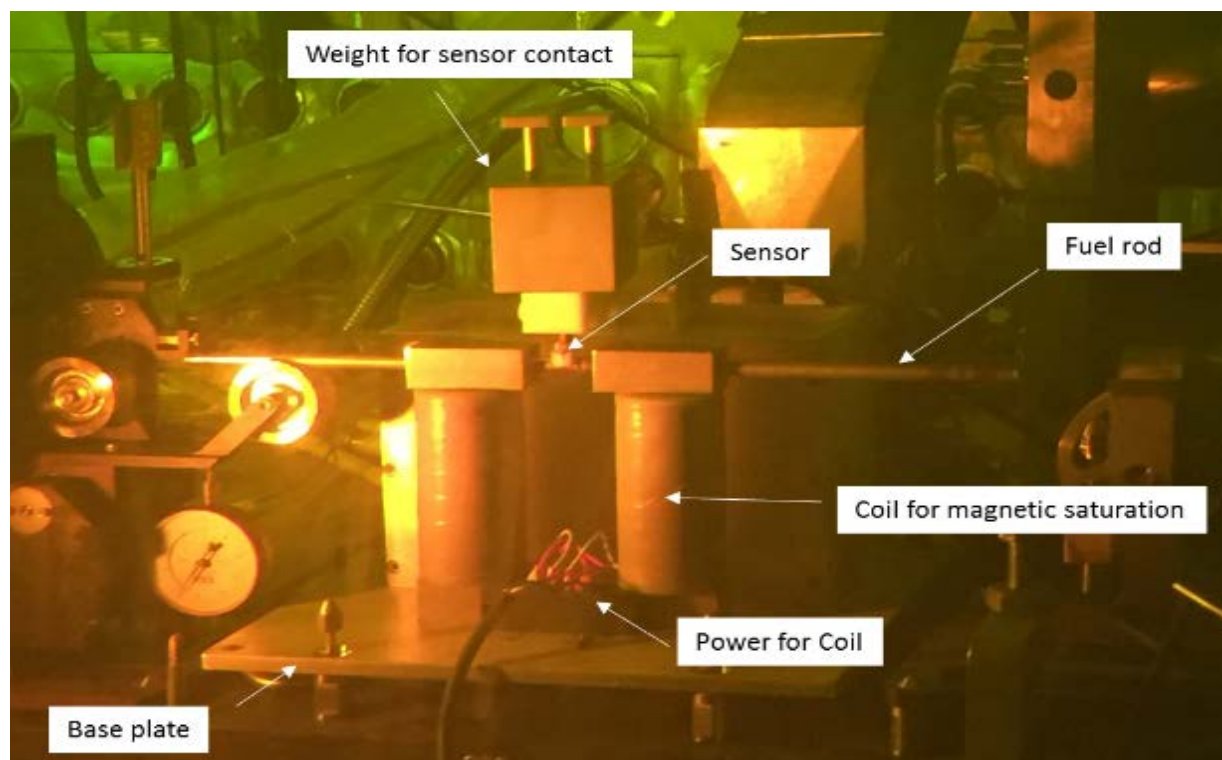


Figure 37. The F-SECT Bench Installed in the IFEL Hot Cell.

Measurements were conducted every 200 mm along the rods. Most rods were measured from lower to higher elevation. At one end of each rod, mostly the lower elevation of the rods, a 500 mm region from the rod end was unable to be measured due to ADEPT limitations. Since F-SECT measurements are point scans, the peak lift-off location can be missed. To reduce this possibility, additional measurements were performed for most rods in higher measured lift-off regions and included both additional axial and azimuthal data. Each position was typically measured twice to check for magnetic CRUD components—once with the magnetic saturation coil off and once with it on. No substantial magnetic component to the CRUD was found.

Representative lift-off data for each cladding type are shown in Figure 38. As expected, based on previously published industry data, lift-off varies as a function of cladding material. When the CRUD contains magnetic components, the thickness of the CRUD alone can be estimated. However, for the sister rods, where no magnetic CRUD components were found, the CRUD thickness cannot be separated from the zirconium oxide thickness. The highest lift-off observed was between rod elevations of ~3,100 and ~3200 mm for all clad four types. The Zirc-4 clad sister rods had the highest oxide thickness overall.

The F-SECT system requires rigorous and frequent calibration to ensure data accuracy. The calibration typically uses a sample of the cladding alloy being measured with an applied nonconductive spacer material in three known thicknesses. Also, a known lower conductivity nickel alloy is used as an independent standard. For the sister rods, unirradiated base cladding samples of ZIRLO, Zirc-4, and M5

were used as calibration standards. The Zirc-4 standard was used when measuring LT Zirc-4. The stability of the F-SECT requires periodic calibration checks to sustain data quality due to the potential for drift in the electronics resulting from factors such as temperature changes. Calibrations were performed before and after each sister rod was measured. The system was predominantly stable during the sister rod examinations.

Data analysis and evaluation of all measured data points are ongoing using F-SECT inversion models, and further results are expected to be reported in the final NDE report.

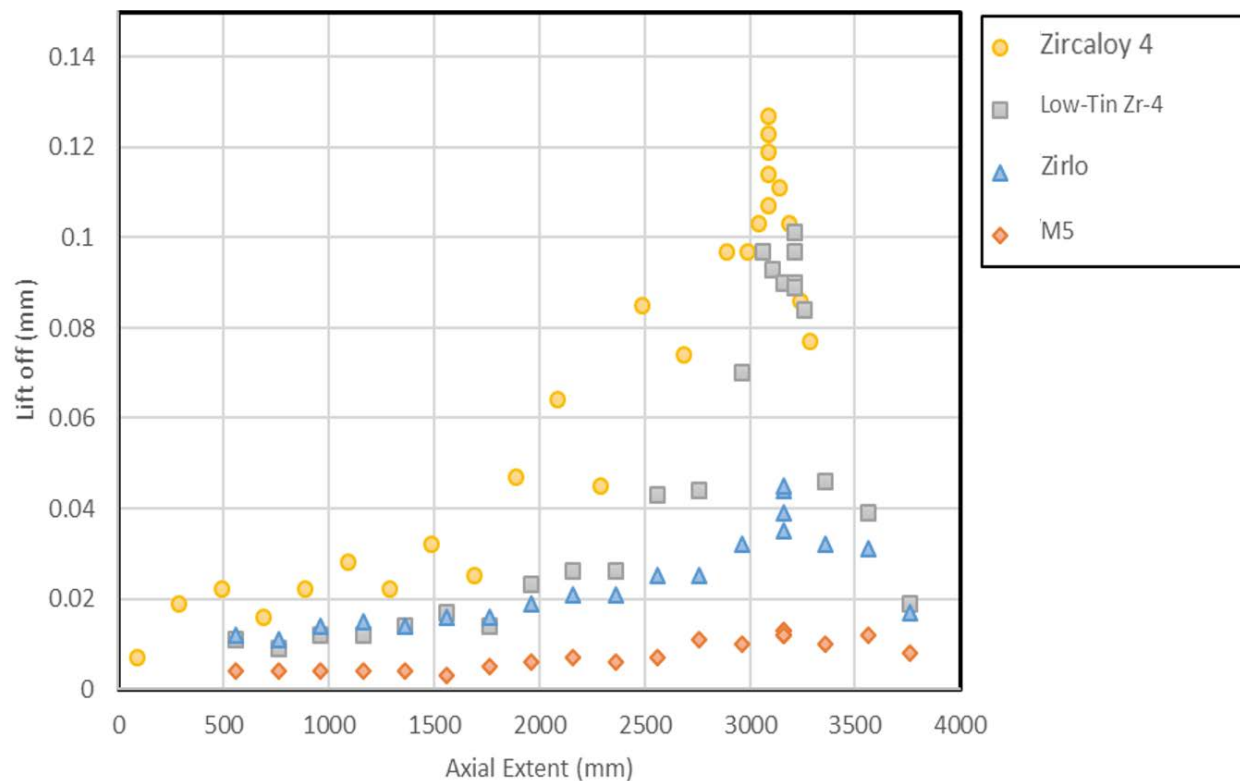


Figure 38. Representative Sister Rod Lift-Off Data for Each Cladding Type.

3.4.2 Traditional eddy current measurements

Traditional eddy current measurements using ADEPT are planned to begin in October 2017.

3.5 NDE.05: Profilometry Measurements

The diameter of the fuel rods was measured at two orthogonal points along their lengths using two sets of linear variable differential transformers (LVDTs). Since numerous photographs were available of each rod, the visual information was also processed to obtain diameter measurements. Section 3.5.1 describes the LVDT measurements taken, and Section 3.5.2 describes the diameter measurements derived from the photos.

3.5.1 LVDT Measurements

LVDT profilometry measurements were completed in April 2017. Two pairs of LVDTs are used: LVDT-1 and LVDT-2 measure 45 degrees off the horizontal plane, and LVDT-3 and LVDT-4 measure 45 degrees off the vertical plane. The two sets of measurements are 90° apart and can provide information on the extent to which the rod is out of round (*ovality*). The LVDT pairs are slightly offset axially for clearance. Using the LVDTs, the rods can only be measured to within about 200 mm of the end caps due to limitations of the rod-guiding mechanics. The 0.02 mm target accuracy of the LVDT apparatus was achieved. Calibration rods were used to calibrate the LVDTs and to check accuracy. For the sister rod measurements, it was found that one pair of LVDTs (3 and 4) consistently read slightly low, so a correction was applied post-measurement.

Figure 39 through Figure 45 provide the average measured rod diameter as a function of axial rod location grouped by assembly. Overall, within the accuracy of the device and given the actual surface condition of the rods, none of the rods were found to be significantly out of round (0.04 mm). Generally, the average is sufficient to identify significant diametrical changes, but the measurements from the two pairs of LVDTs can be slightly out of phase, and averaging can eliminate the peaks and valleys associated with the pellet ridging. Localized features such as spalling depth, surface dents, and pellet ridging can be identified using (1) individual LVDT traces, which occur only at 2 orthogonal locations along the length, (2) gamma scans, which provide a cross sectional indication only, and (3) visual profilometry, which can have limited resolution capability. A combination of these measurements can also be used. The traces for both pairs of LVDTs are provided in Appendix A.

There were no indications of significant rod swelling or clad major defects. In general, the expected diametrical trends were observed: the rod's diameter is larger in higher burnup regions and smaller in lower burnup regions. However, given the higher burnup of these rods, it is surprising that not many expanded beyond the as-fabricated rod's outer diameter (OD). Only the Zirc-4 and LT Zirc-4 rods appear to have positive diametrical strains on the order of 1%. Several of the M5 and ZIRLO rods never regained their preirradiation OD. As expected, the diameter of the rod in the plenum region is very near the as-fabricated cladding OD. Although they could not be measured with the LVDTs, the top- and bottom-end cap diameters are also near the as-fabricated end cap diameters (measured using the visual diameter analysis, see Section 3.5.2 and Appendix B).

Some rods had very thick oxide layers with large spalled areas (see Section 3.1). Rods with the thickest oxide layers appear to have erratic diameter measurements. In particular, Assemblies 3A1 and F35 show the expected increasing diameter from the bottom to the top of the rod (referenced to the true bottom for the F35 rods), but there is a large amount of point-to-point variation in the higher rod elevations due to the uneven spalling oxide layer.

Bambooning, which is a small diameter variation with a period of about 10 mm (the pellet length), was observed in all rods. Figure 46 shows a portion of the bottom region of rod 6U3P16, illustrating bambooning caused by pellet-cladding interaction during operation.

The average LVDT-measured rod diameter for rod 30AG09 displayed a region of increased diameter near 1,000 mm; the visual exam showed nothing unusual in this region. Upon examination of the individual LVDT data shown in Figure 47, it is evident that the spike in diameter was only measured by the LVDT-1/LVDT-2 pair. Inspection of the diametrical data obtained with the visuals (see Section 3.5.2) does not indicate an increased diameter in any direction, but the difference in diameter between the two sets of LVDTs was only about 0.03 mm, which is only marginally larger than the expected accuracy of the pairs. This difference may have come from some small debris that was carried along by the LVDT, momentary sticking of the LVDT, or a larger-than-expected off-center shift of the rod as it went through the LVDTs that moved the rod out of the optimal measuring range. Thus, this particular local diameter increase is considered a spurious measurement.

Finally, a fairly large ($\sim\frac{3}{4}$ pellet length) reduced diameter (~ 0.5 mm) region was noted in the profilometry scan for rod 6U3P16, as shown in Figure 48. The reduction was measured by both pairs of LVDTs, but it is not observable in the visual profilometry. This is likely due to the visual method's lower axial resolution, which only has measurements every 40 mm. This reduced diameter region aligns well with the reported gamma scan pellet gap (see Table 5) and is likely the same feature.

3.5.2 Visual Profilometry

All of the sister rods were extensively photographed. The camera used was fixed in location, and the rods in the ADEPT were at a constant distance with respect to the camera. While rod bow and ADEPT handling features can induce some small off-axis movements, the distance from the rod to the camera can only vary an estimated $\frac{1}{8}$ inch in an approximately 85-inch optical path. The visual camera was also used to photograph the profilometry calibration rod which has a known nominal diameter of 0.3752 ± 0.0001 inches, although the axial variation of this diameter is unknown. It is likely 1–5 ten-thousandths of an inch. The photographs of the calibration rod (diameter) were used to determine the length-to-pixel ratio for the images. This information was used to resolve boundary pixel criteria (edge of rod versus background) and to scale the pixel count to diameters. The diameter was measured in 1 mm increments along the length of the rod at 0, 45, 90, 135, 180, 225, 270, and 315-degree rotations. An average diameter was calculated at 40 mm intervals by (1) averaging the 1 mm measurements contained within the interval for each rotation angle and (2) averaging all rotations at that elevation. This provided 97 average diameter measurements along the length of the sister rod. An example of the measurements is provided in Figure 49 as compared with the LVDT measurements and features identified by gamma scan.

Although these measurements are not considered to be as accurate as the LVDT measurements in total, they are useful in verifying trends, measuring the ends of the rods that cannot be measured with the LVDTs, and for additional observations around the circumference of the rod. For example, the discrepancy in the local measurement of rod 30AG09 (mentioned above) was verified using the visual data. However, there appears to be a measurement effect related to the angle of view, as the data tend to exhibit a sinusoidal trend with the rod rotation angle, as shown in Figure 50. The effect, roughly ± 0.05 mm, could be related to a lens distortion, or it is more likely due to an ADEPT off-center rotational effect combined with uneven lighting/background making the edge determination inconsistent. However, it seems that calibration with the imaging must be completed for each angle of rotation to ensure better accuracy, and work beyond the scope of this program would be required to process these data. The averaging mentioned above eliminates some of this effect.

Appendix B presents the visual profilometry plots compared with the average LVDT profilometry measurements and features from the gamma scanning data for all sister rods. Overall, this method gives reasonable agreement with the LVDT data, and the overall accuracy appears to be generally much better than the identified 0.05 mm. Optimization of the optical path and camera optics, along with a fixed reference point for picture-by-picture calibration, could lead to a non-contact fast measurement system.

3.6 NDE.06: Surface Temperature Measurements

Surface temperature measurements have not yet been completed. They are scheduled for the September 2017 timeframe concurrent with eddy current measurements

Assembly 30A Average Profilometry

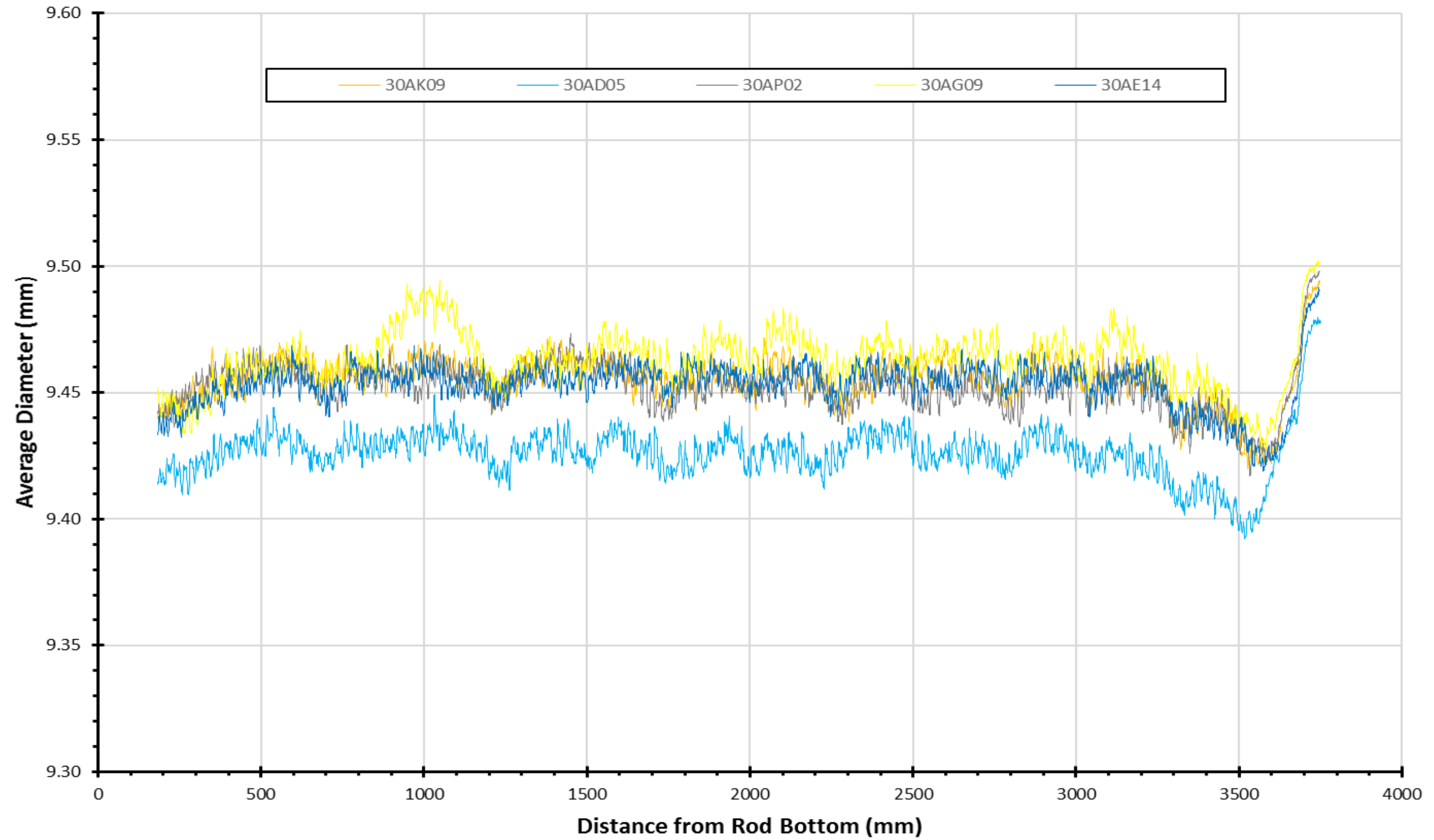


Figure 39. Profilometry Scans for Assembly 30A.

Assembly 5K7 Average Profilometry

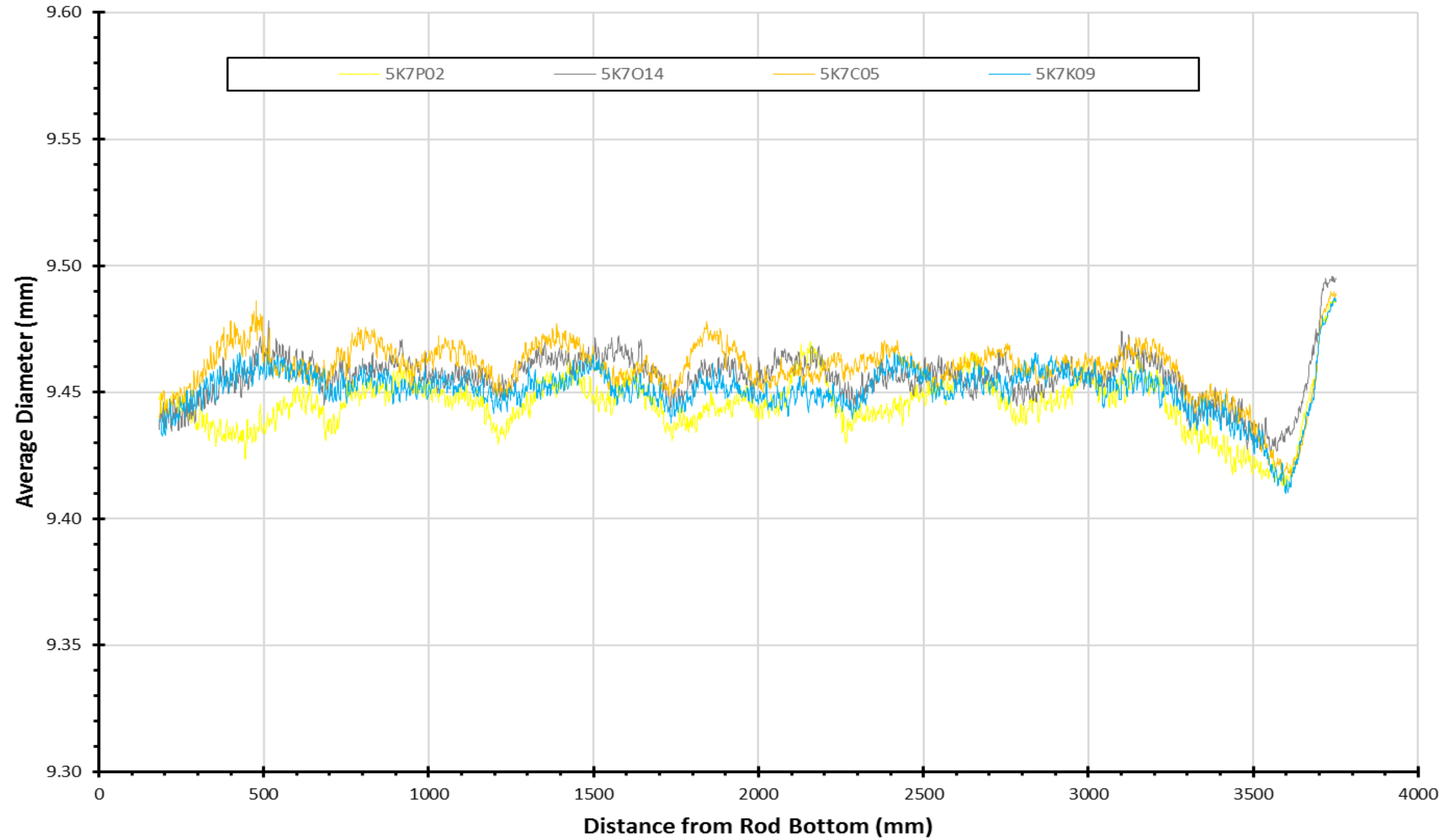


Figure 40. Profilometry Scans for Assembly 5K7.

Assembly F35 Average Profilometry

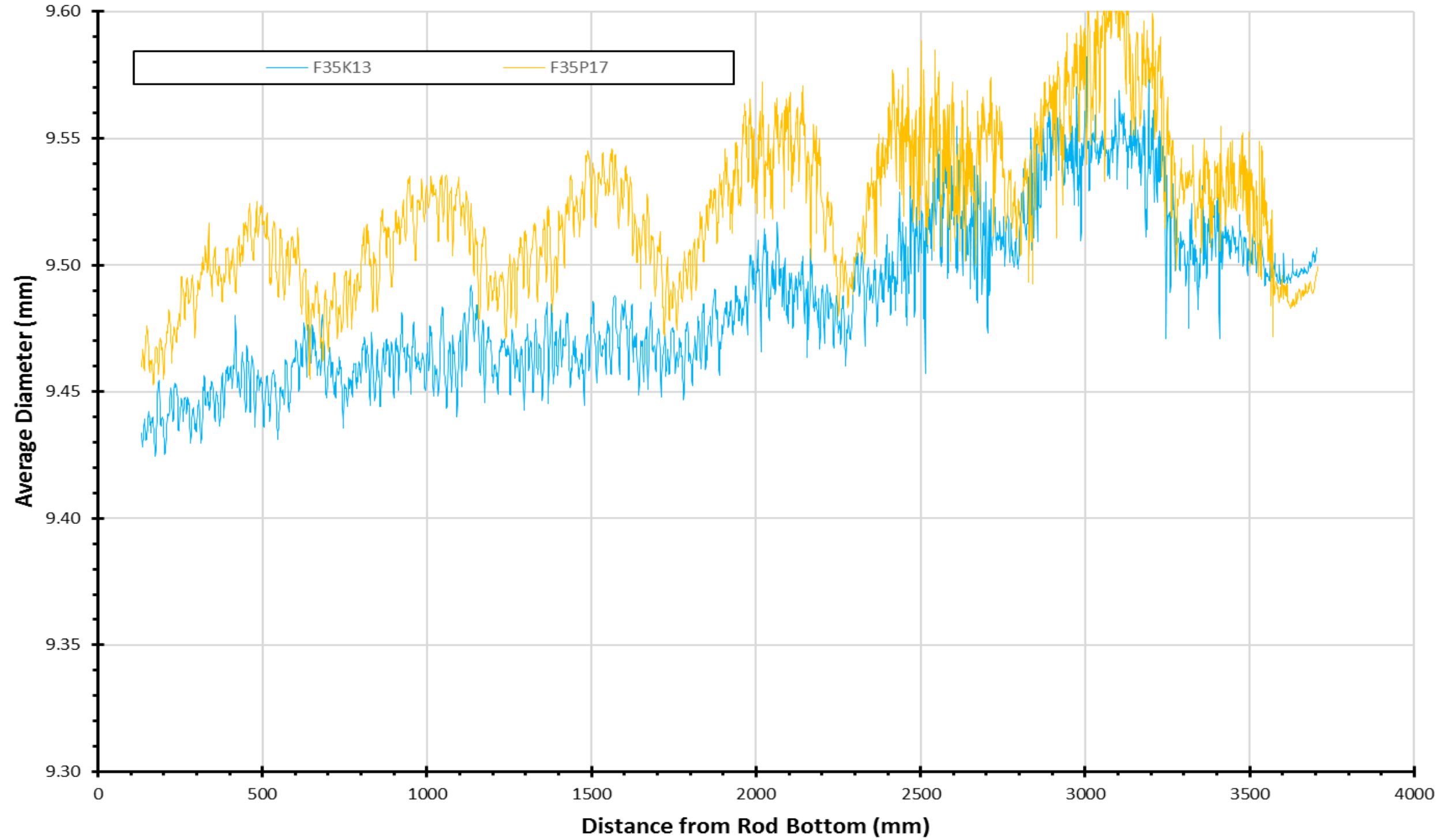


Figure 41. Profilometry Scans for Assembly F35.

Assembly 3A1 Average Profilometry

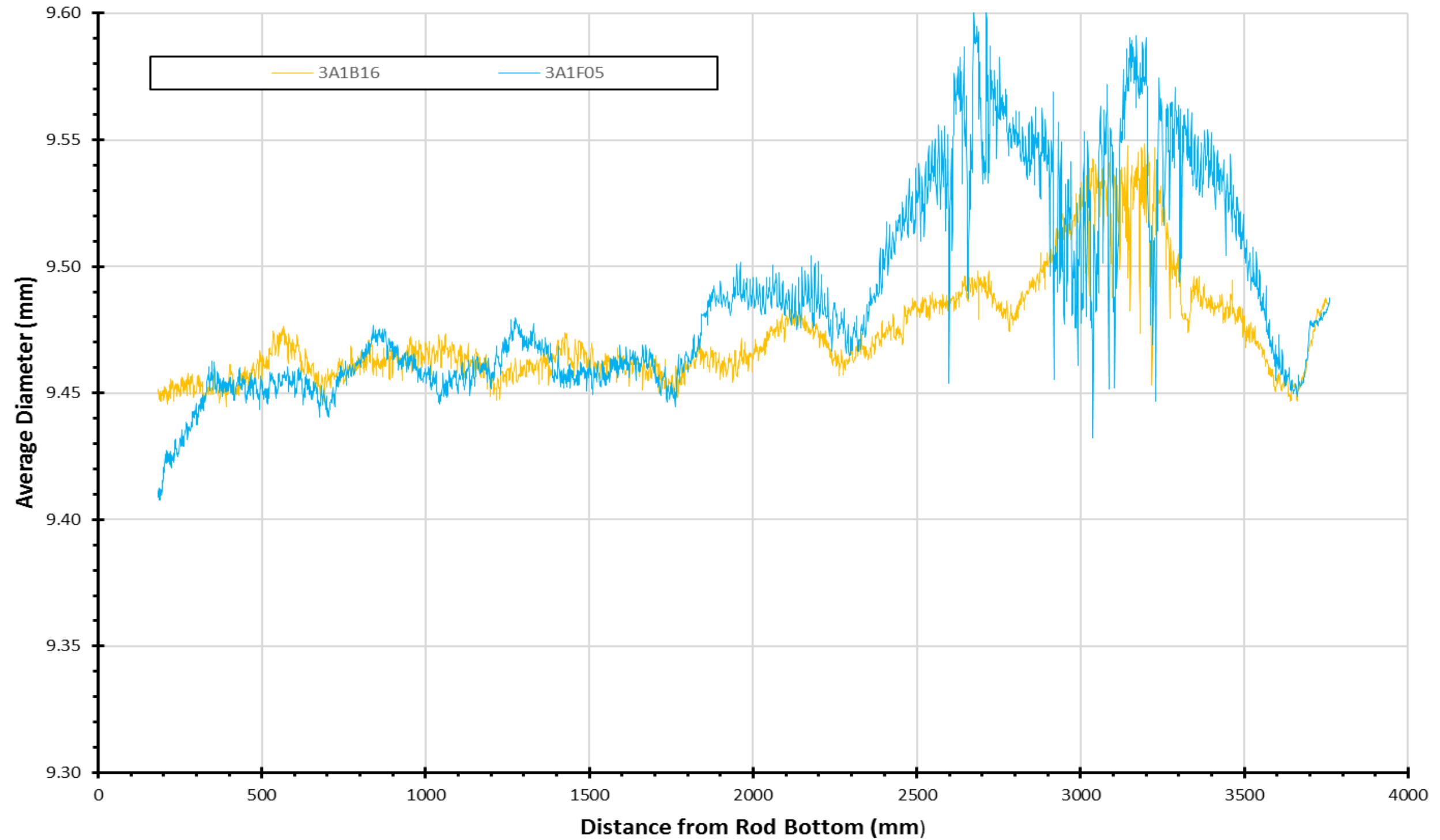


Figure 42. Profilometry Scans for Assembly 3A1.

Assembly 3F9 Average Profilometry

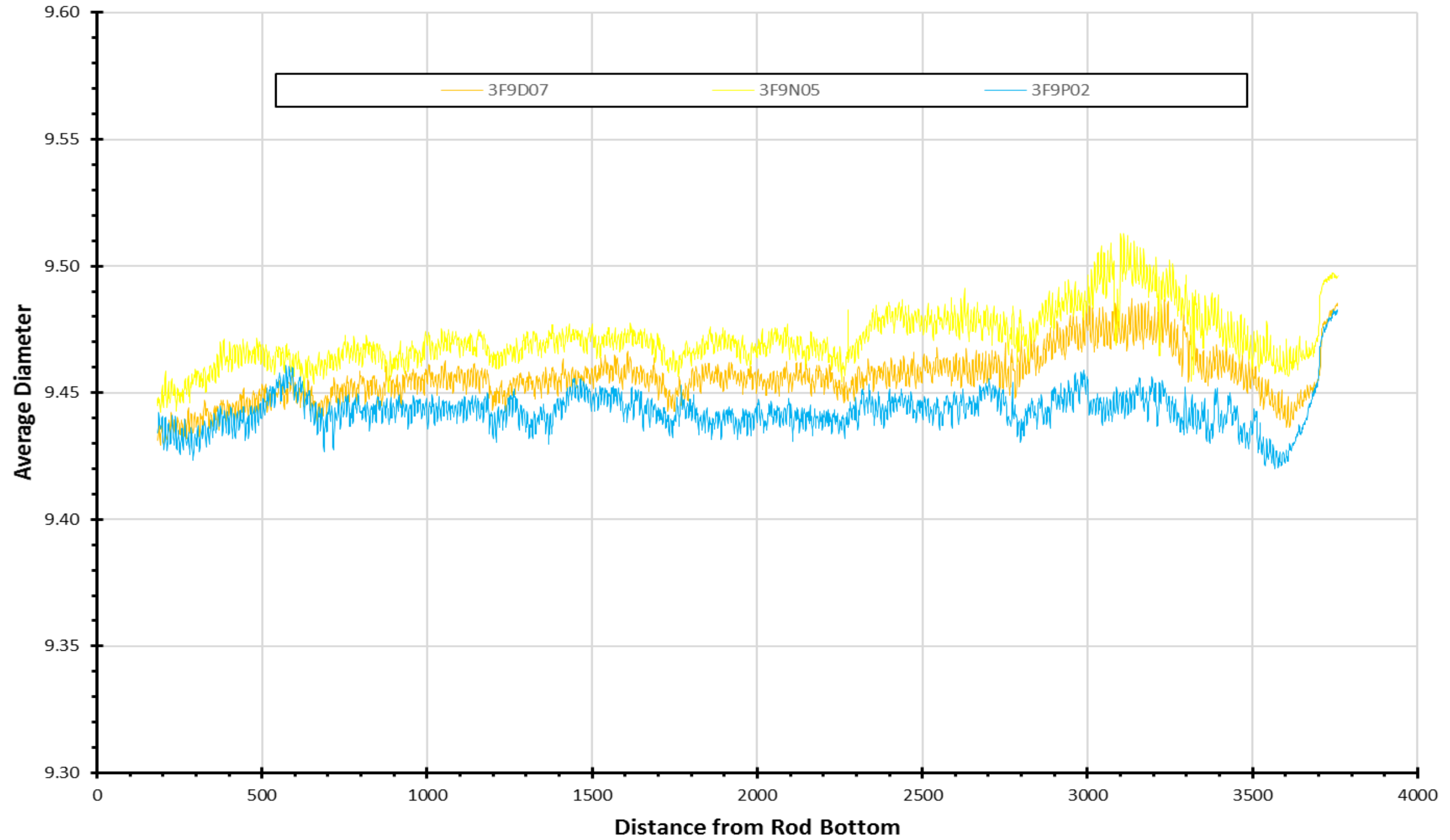


Figure 43. Profilometry Scans for Assembly 3F9.

Assembly 3D8 Average Profilometry

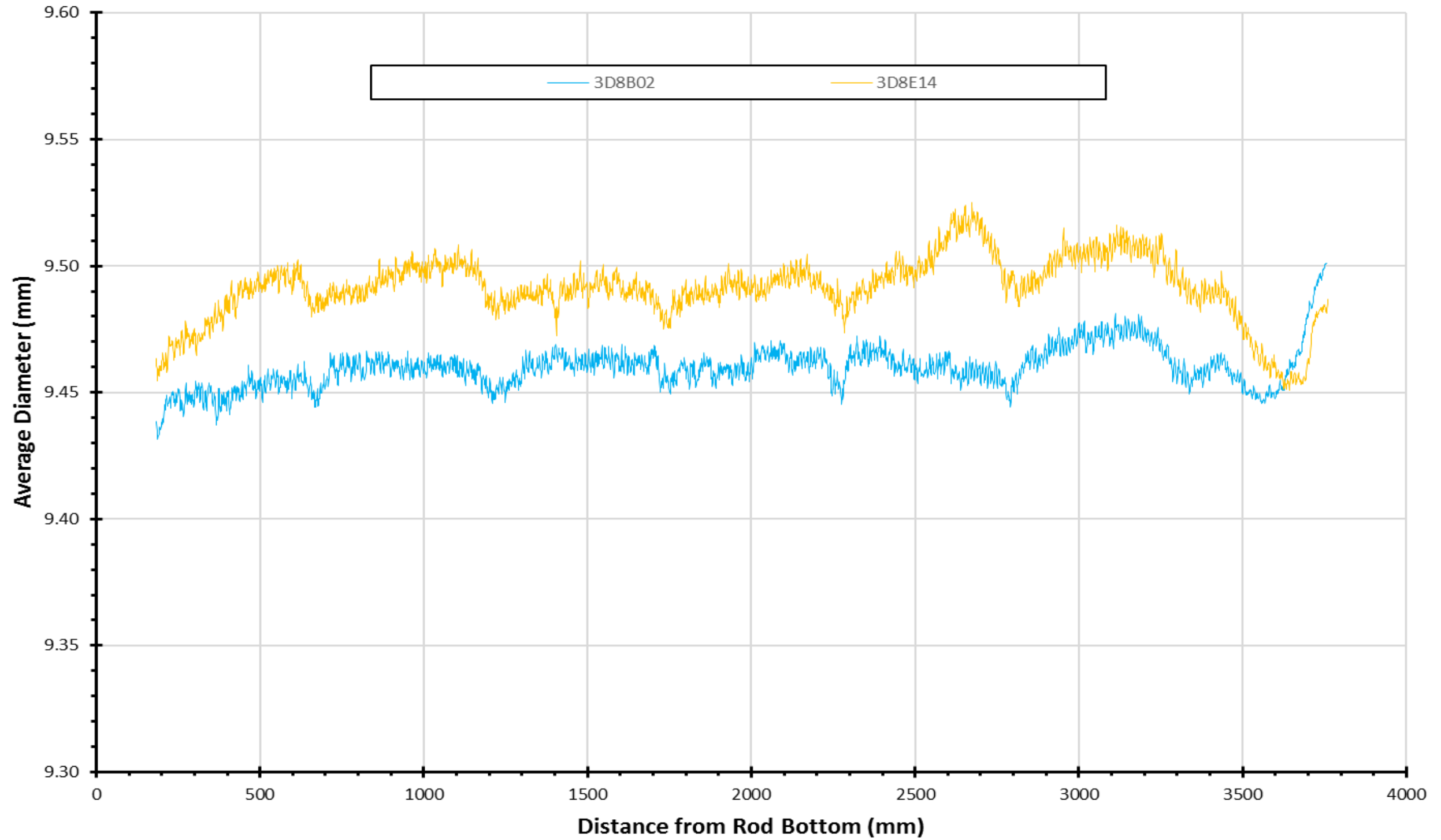


Figure 44. Profilometry Scans for Assembly 3D8.

Assembly 6U3 Average Profilometry

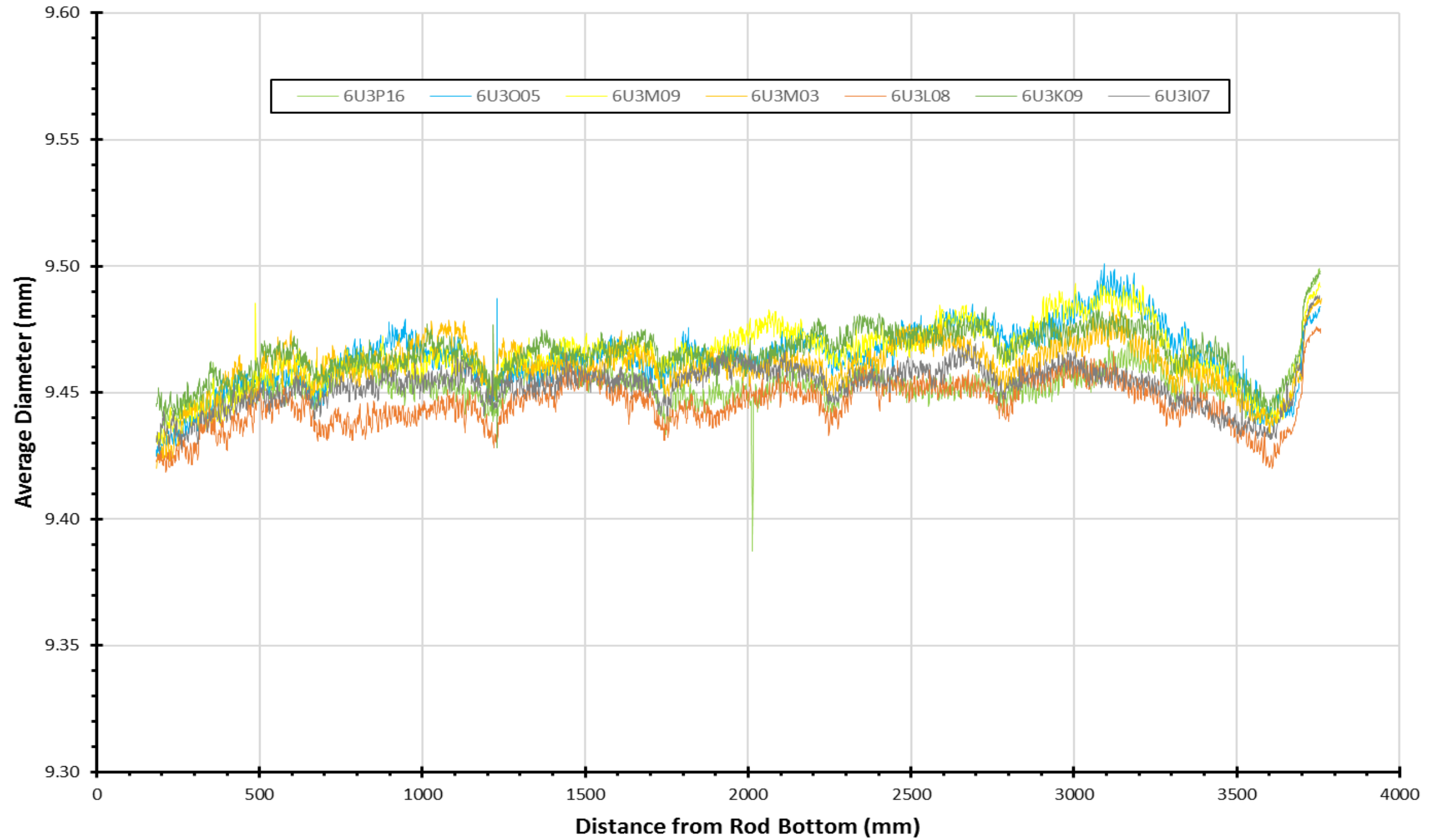


Figure 45. Profilometry Scans for Assembly 6U3.

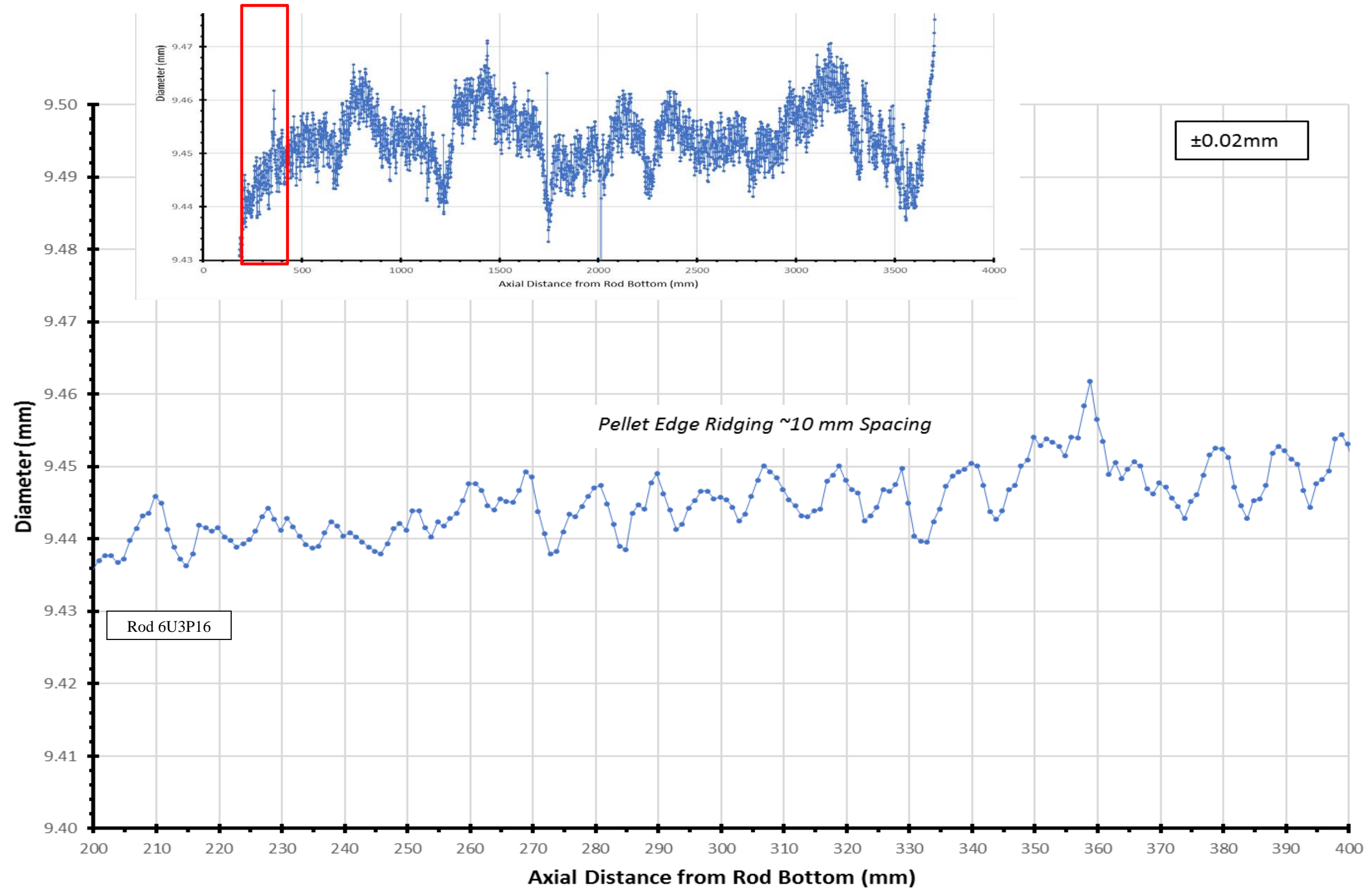


Figure 46. Typical Pellet Ridging on a Fuel Rod via LVDT-Based Profilometry; Scales are Magnified to Show the Detail. The Typical Pellet is Approximately 10mm long.

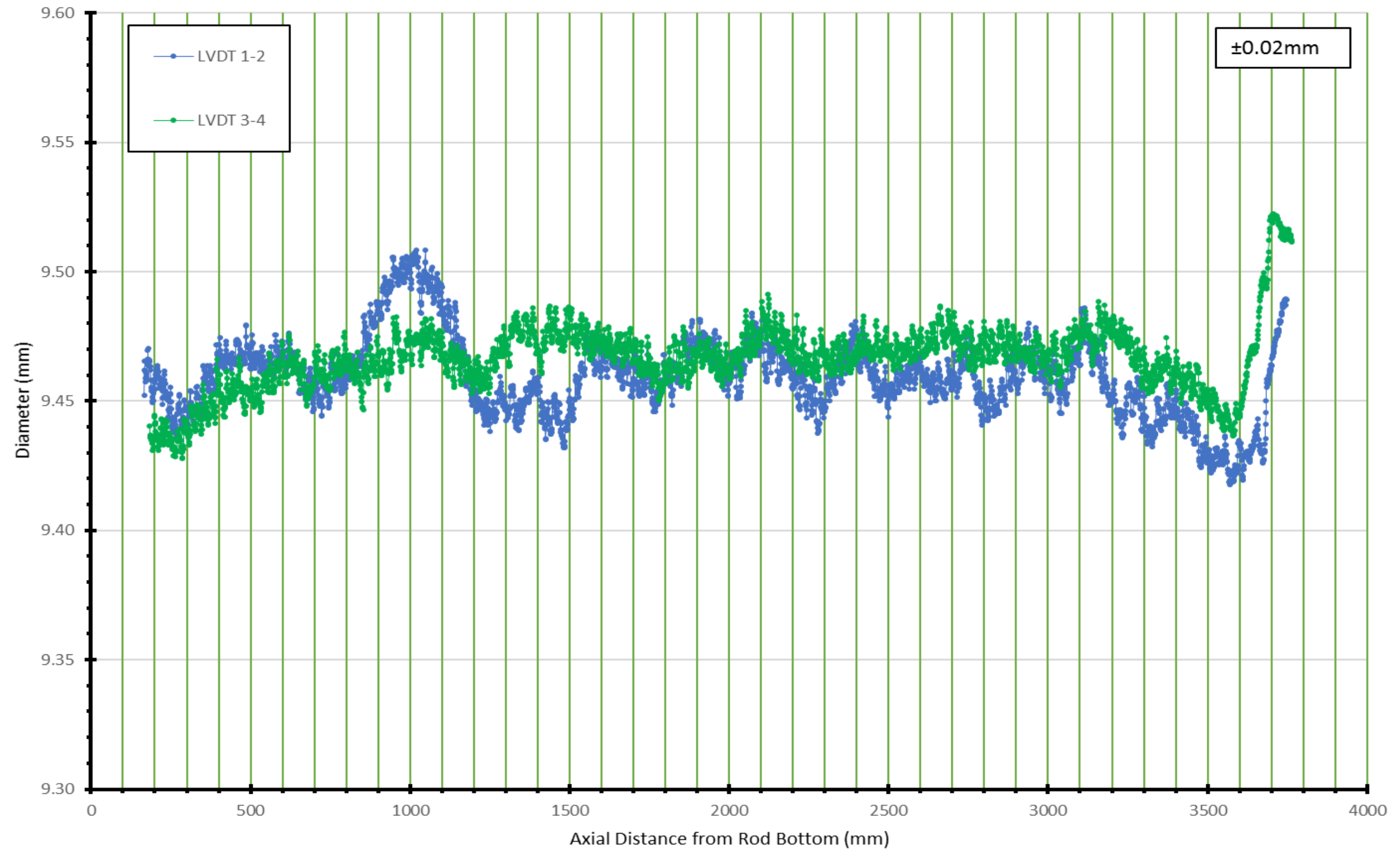


Figure 47 Individual LVDT Measurements for Rod 30AG09 Illustrating the Difference in Measurements for the Two Pairs between 900 and 1,600 mm.

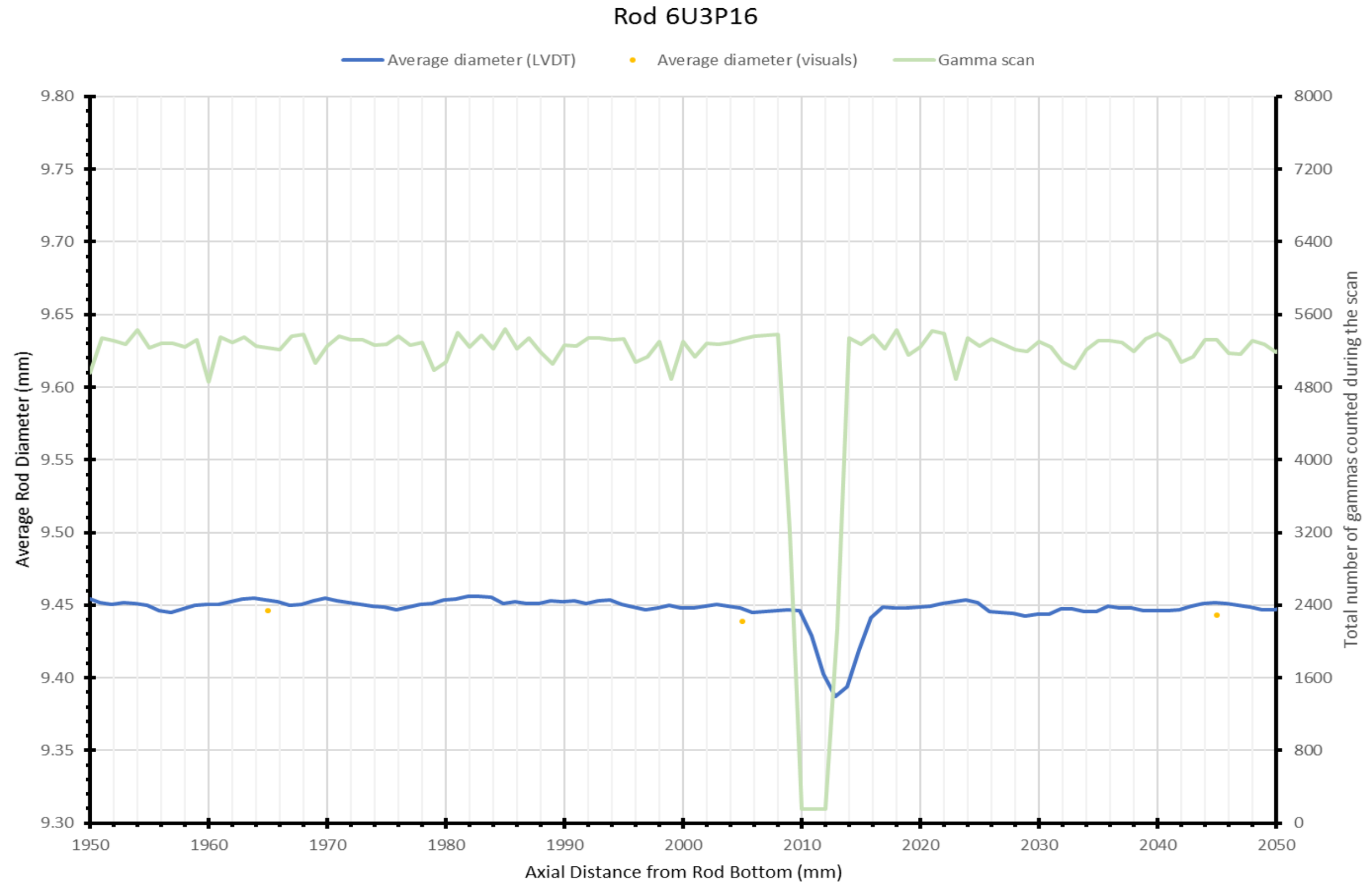


Figure 48. Average Diameter Reduction in Rod 6U3P16; This Reduction Nearly Aligns with the Pellet Stack Gap Noted in the Gamma Scan.

Rod F35K13

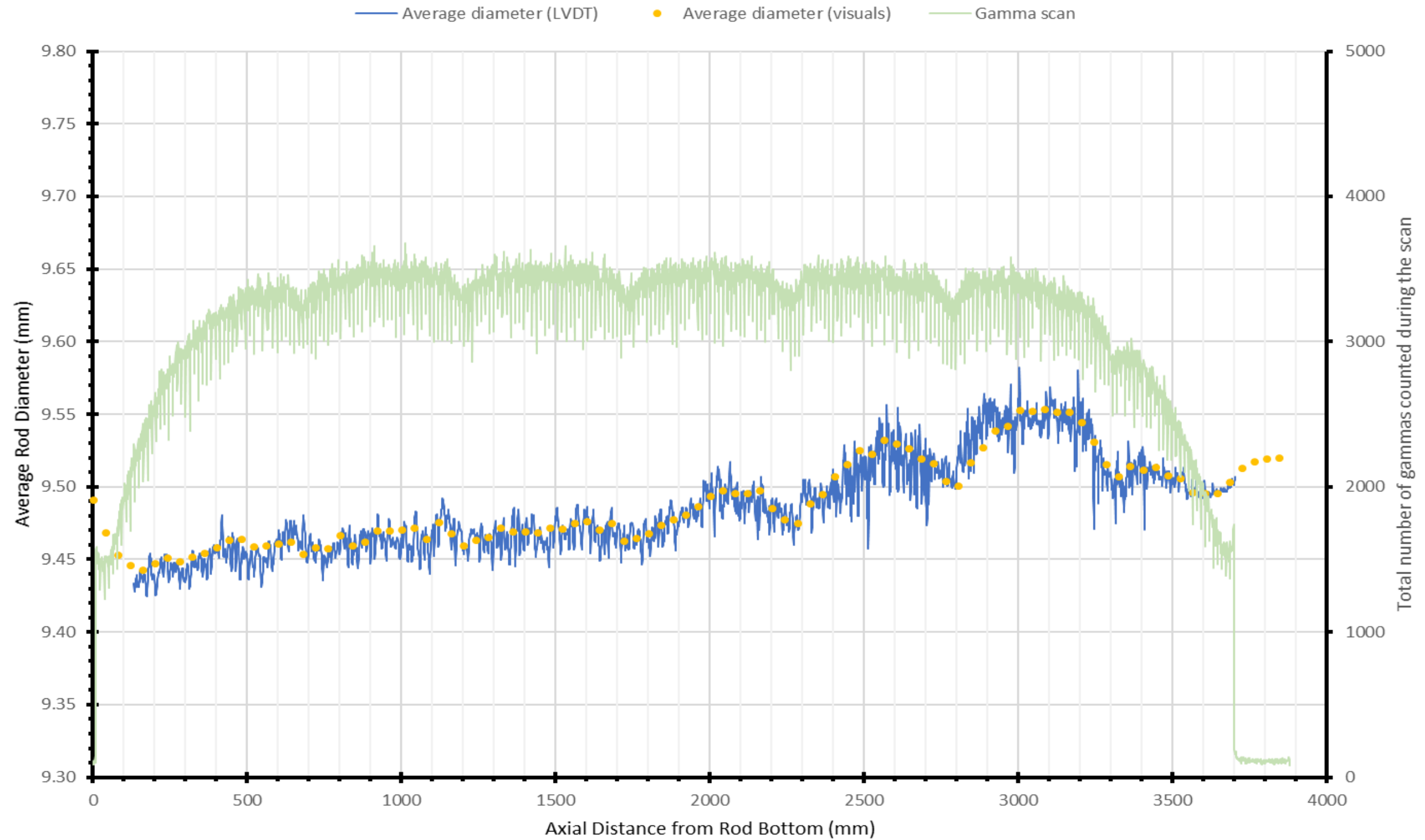


Figure 49. Example of LVDT Measurements and Visuals Diameter Measurements as Compared with Features Indicated by the Gamma Scans for Rod F35K13.

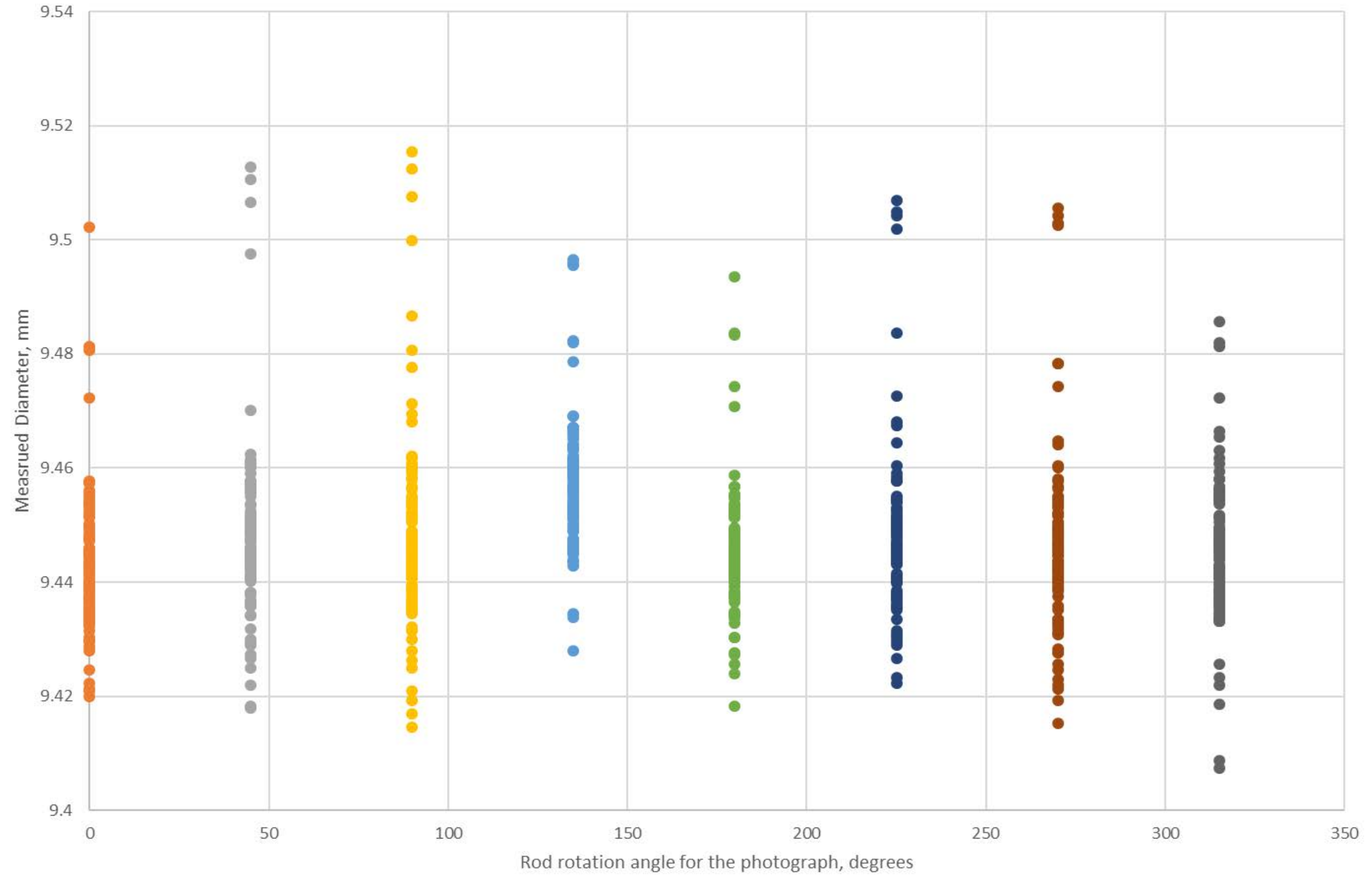


Figure 50. Observed Sinusoidal Trend in Visual Profilometry Data with Angle of Rod Rotation.

4. REFERENCES

1. EPRI. *High Burnup Dry Storage Cask Research and Development Project: Final Test Plan*. Contract No.: DE-NE-0000593. Electric Power Research Institute, Palo Alto, California, 2014.
2. Montgomery, R. A. et al. *Post-irradiation Examination Plan for High Burnup Demonstration Project Sister Rods*, SFWD-SFWST-2017-000090 ORNL/SR-2016/708, Oak Ridge National Laboratory, Oak Ridge, Tennessee, December 30, 2016.
3. Joseph, R., A. Myers, J. Jarrell, K. Banerjee, and J. Peterson. *SNF Data Visualization on the Centralized Used Fuel Resource for Information Exchange (CURIE) Website*, Transactions of the American Nuclear Society, Vol. 116, San Francisco, California, June 11–15, 2017, 225–228.
4. Smith, S. K., A. Nicholson, S. Croft, and G. Nutter. *Measurement of Pressurized Water Reactor Spent Nuclear Fuel Rods by High-Resolution Gamma Spectroscopy for Burnup Code Verification*, ORNL/SPR-2017/381, 2017.
5. Rooney, B., S. Garner, P. Felsher, and P. Karpus. PeakEasy 4.91 [Computer Program], Los Alamos National Laboratory, Los Alamos, NM, Release LA-CC-13-040. Available: <https://PeakEasy.lanl.gov>, 2015.
6. Broadhead, B. and C. F. Weber. “Validation of Inverse Methods Applied to Forensic Analysis of Spent Fuel,” 51st Annual Meeting of the Institute of Nuclear Materials Management, Baltimore, MD, 2010.
7. Chu, S. Y. F, L. P. Ekström, and R. B. Firestone. *WWW Table of Radioactive Isotopes, database version 1999-02-28*. Accessible from URL <http://nucleardata.nuclear.lu.se/toi/>, 1999.
8. IAEA, *Safeguards Techniques and Equipment: 2011 Edition*, IAEA, http://www-pub.iaea.org/MTCD/Publications/PDF/nvs1_web.pdf, Vienna, 2011.

Appendix A

Traces for Both LVDT pairs

Figure A.1 through Figure A.25 show the individual LVDT diameter measurements for the rods. They consist of two sets of LVDT measurements with each pair of LVDTs 90° apart. The rod's angular orientation is random, so there is no information that can be related back to a specific grid direction.

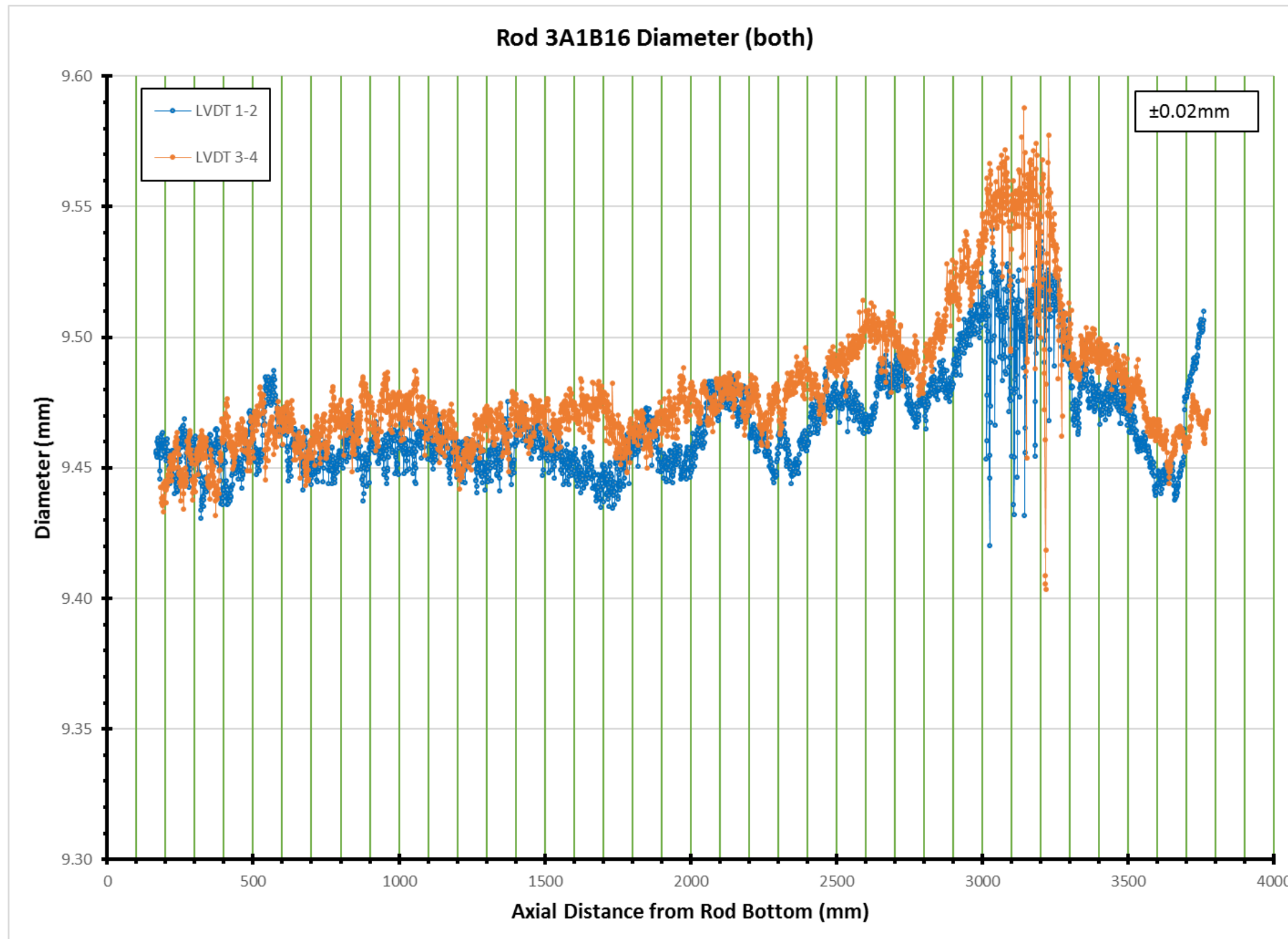


Figure A.1. Rod 3A1B16 LVDT Diameter Measurements.

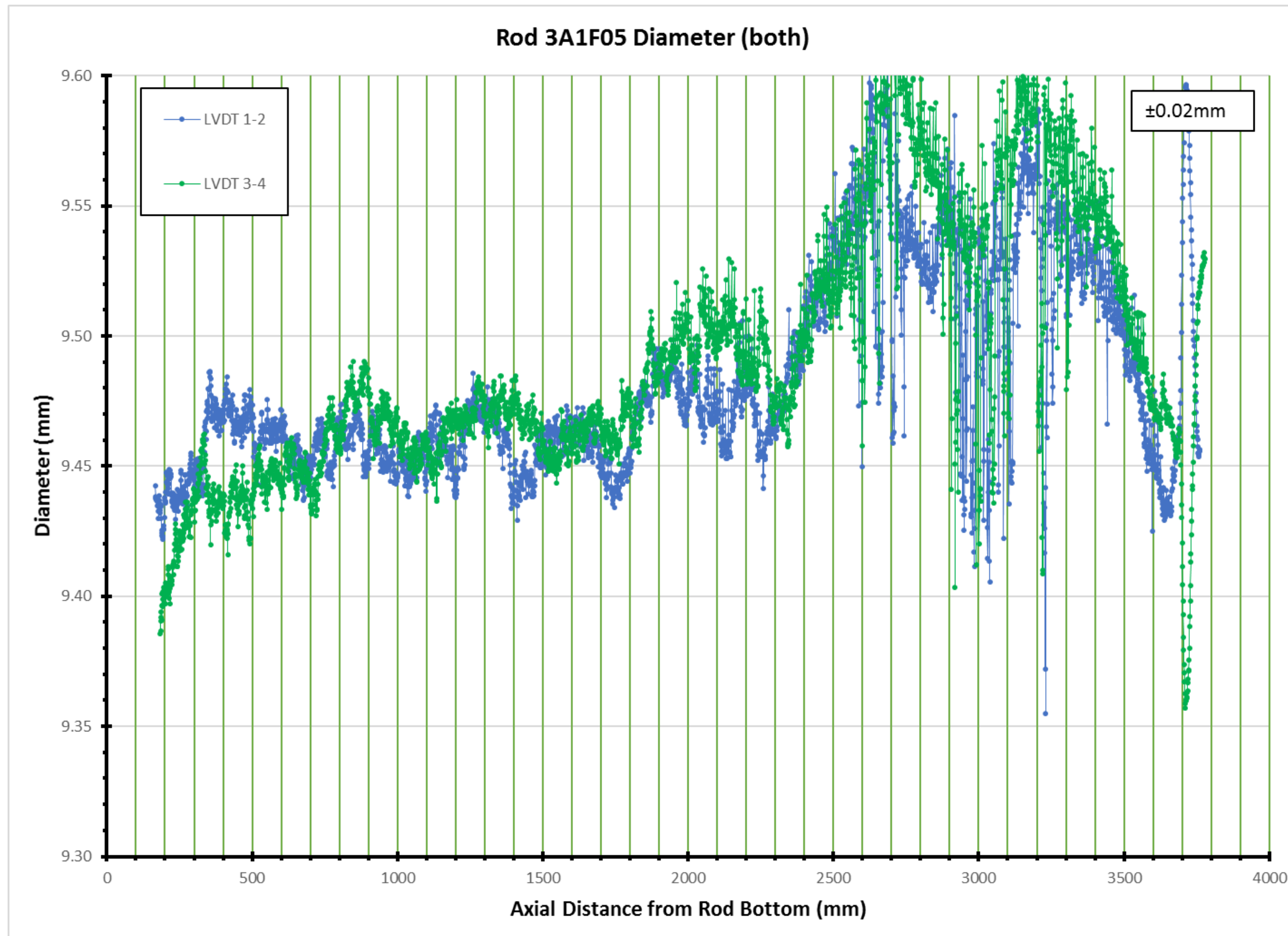


Figure A.2. Rod 3A1F05 LVDT Diameter Measurements.

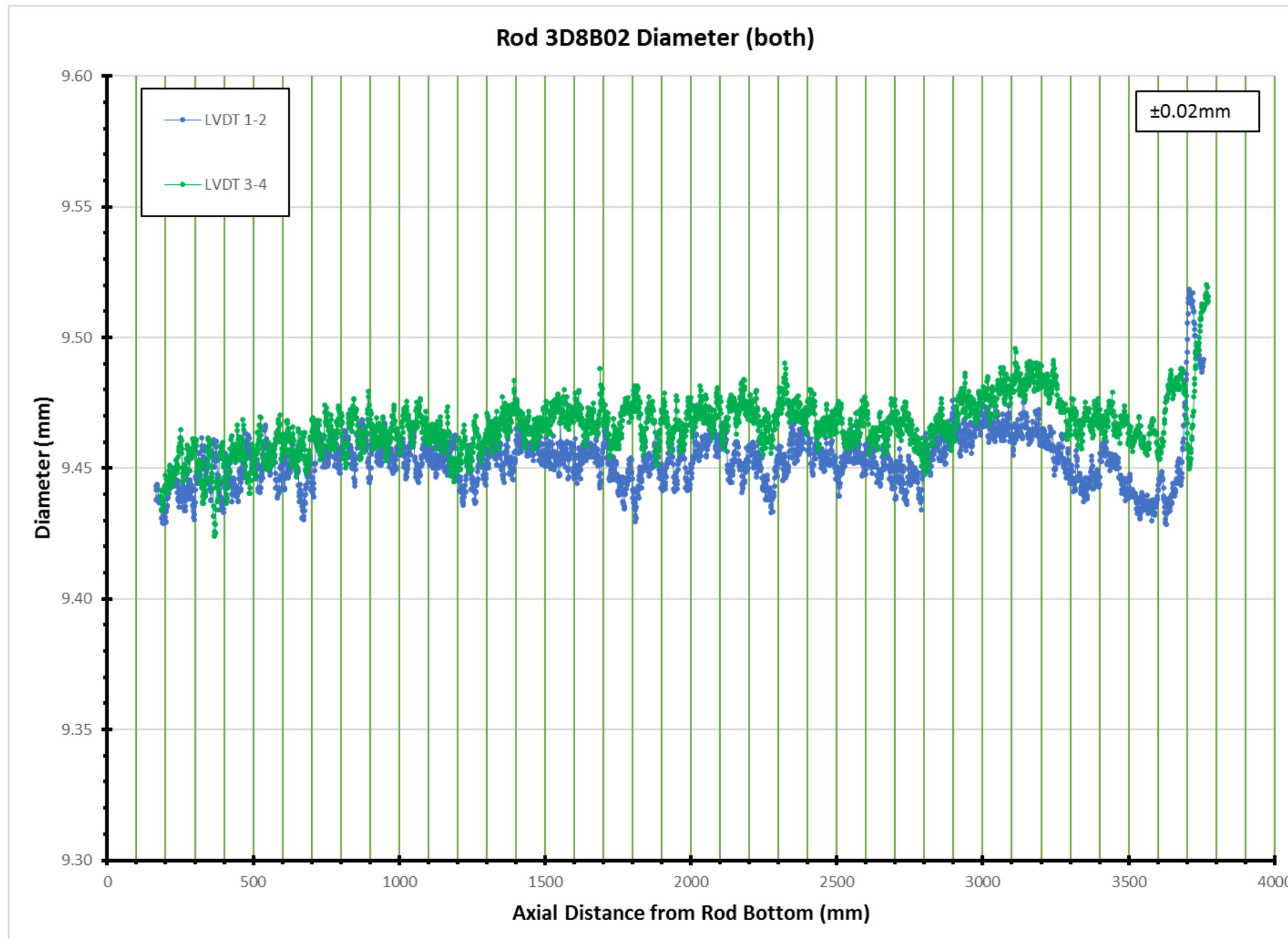


Figure A.3. Rod 3D8B02 LVDT Diameter Measurements.

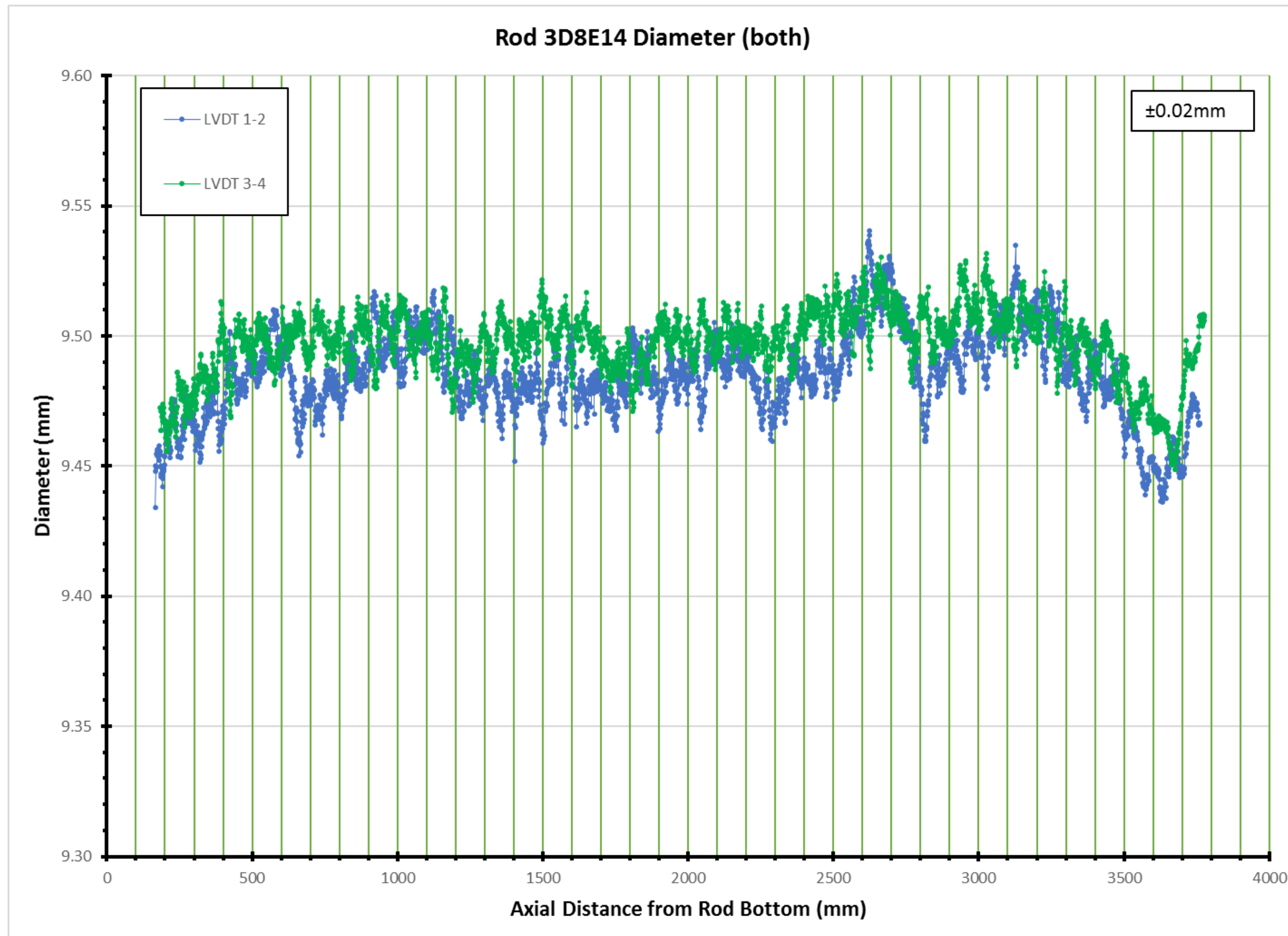


Figure A.4. Rod 3D8E14 LVDT Diameter Measurements.

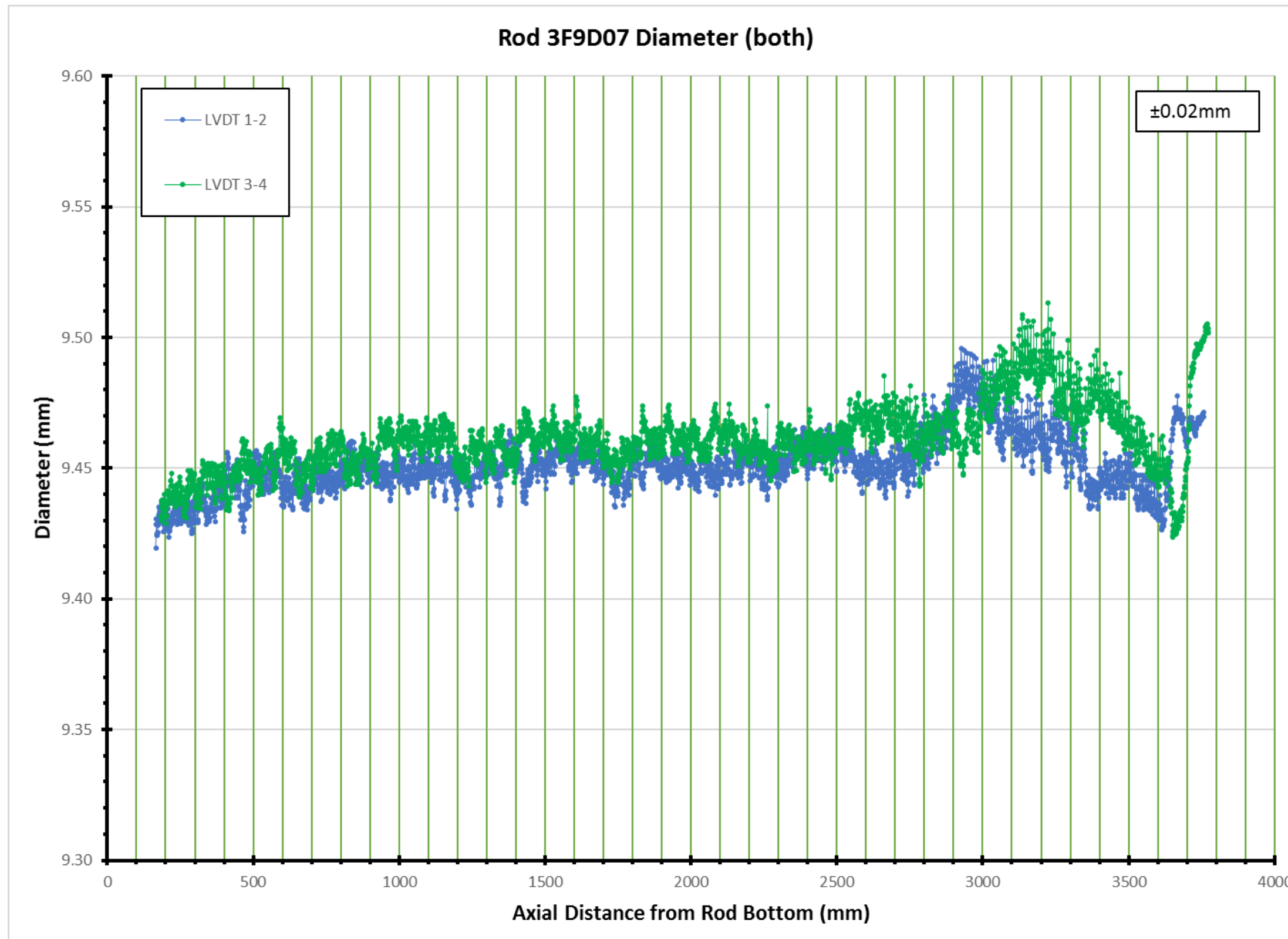


Figure A.5. Rod 3F9D07 LVDT Diameter Measurements.

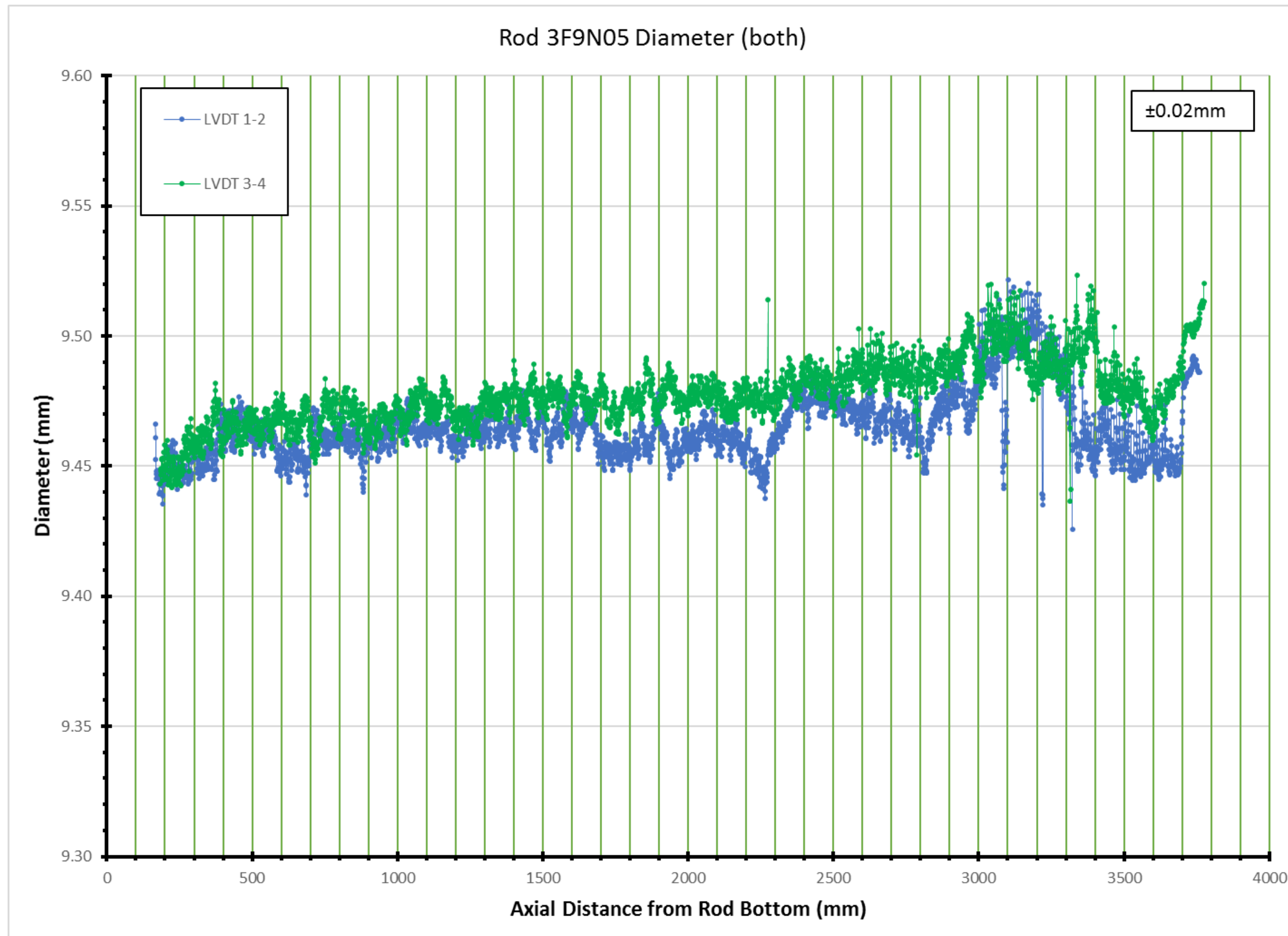


Figure A.6. Rod 3F9N05 LVDT Diameter Measurements.



Figure A.7. Rod 3F9P02 LVDT Diameter Measurements.

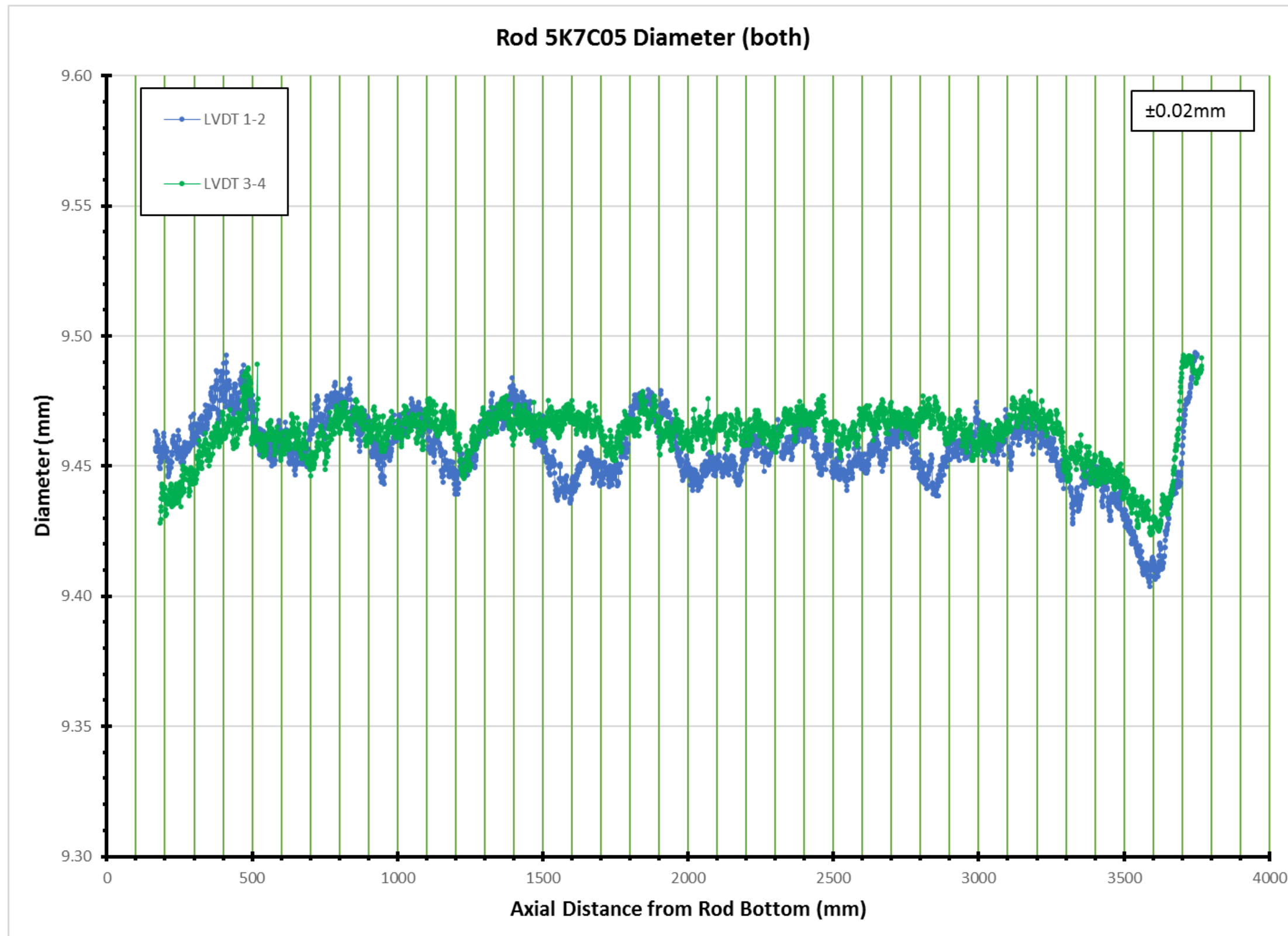


Figure A.8. Rod 5K7C05 LVDT Diameter Measurements.

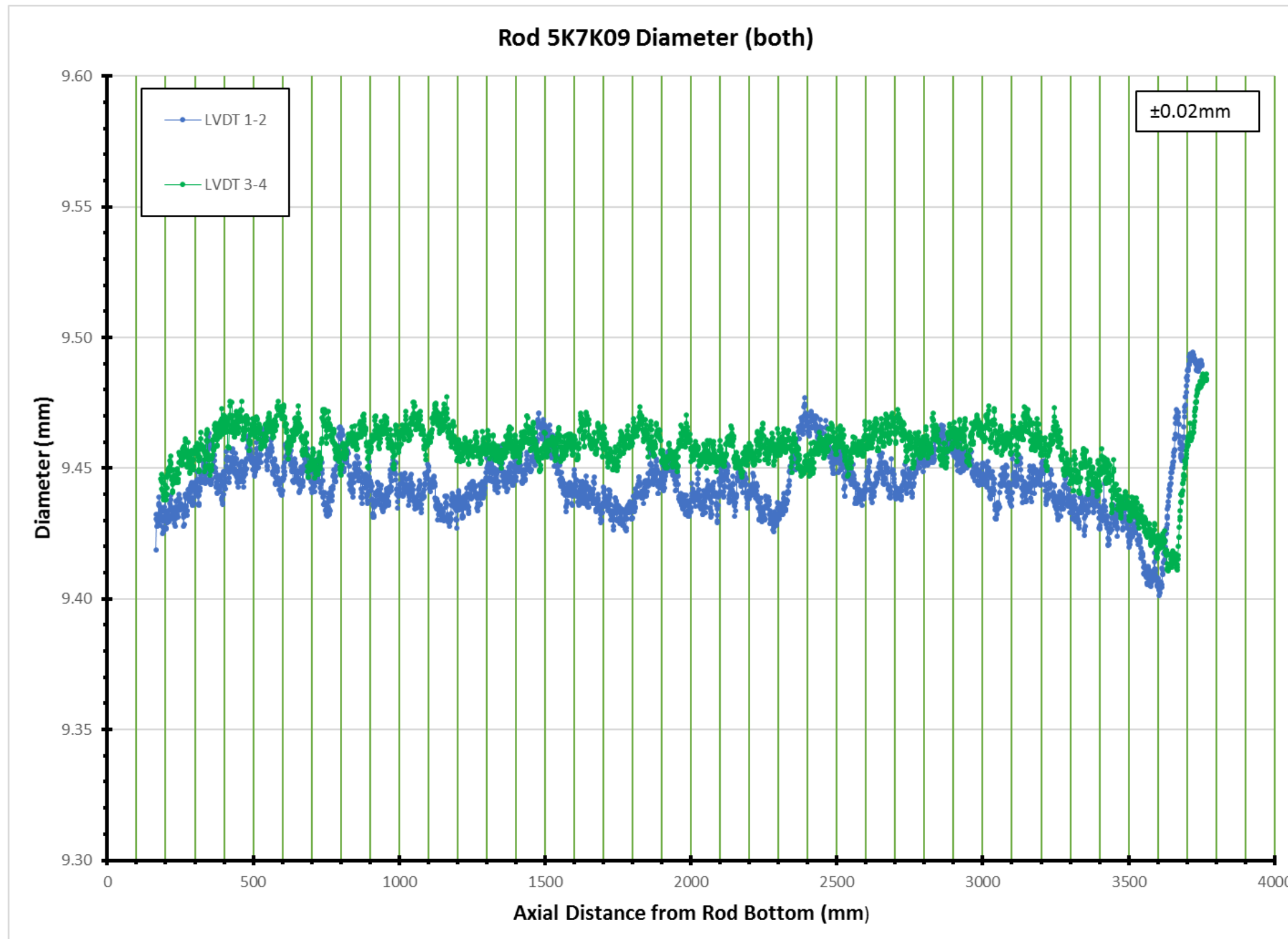


Figure A.9. Rod 5K7K09 LVDT Diameter Measurements.

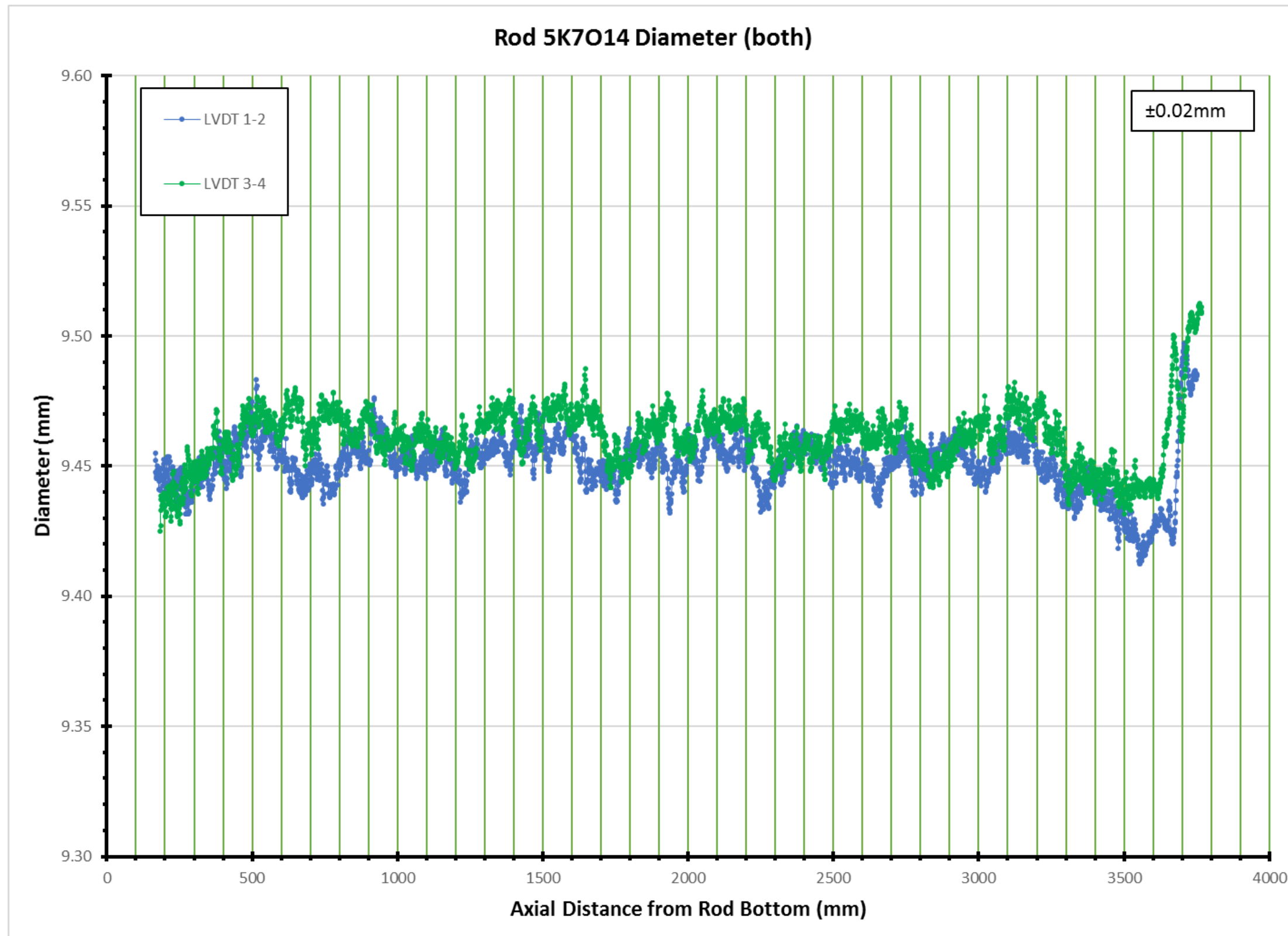


Figure A.10. Rod 5K7014 LVDT Diameter Measurements.

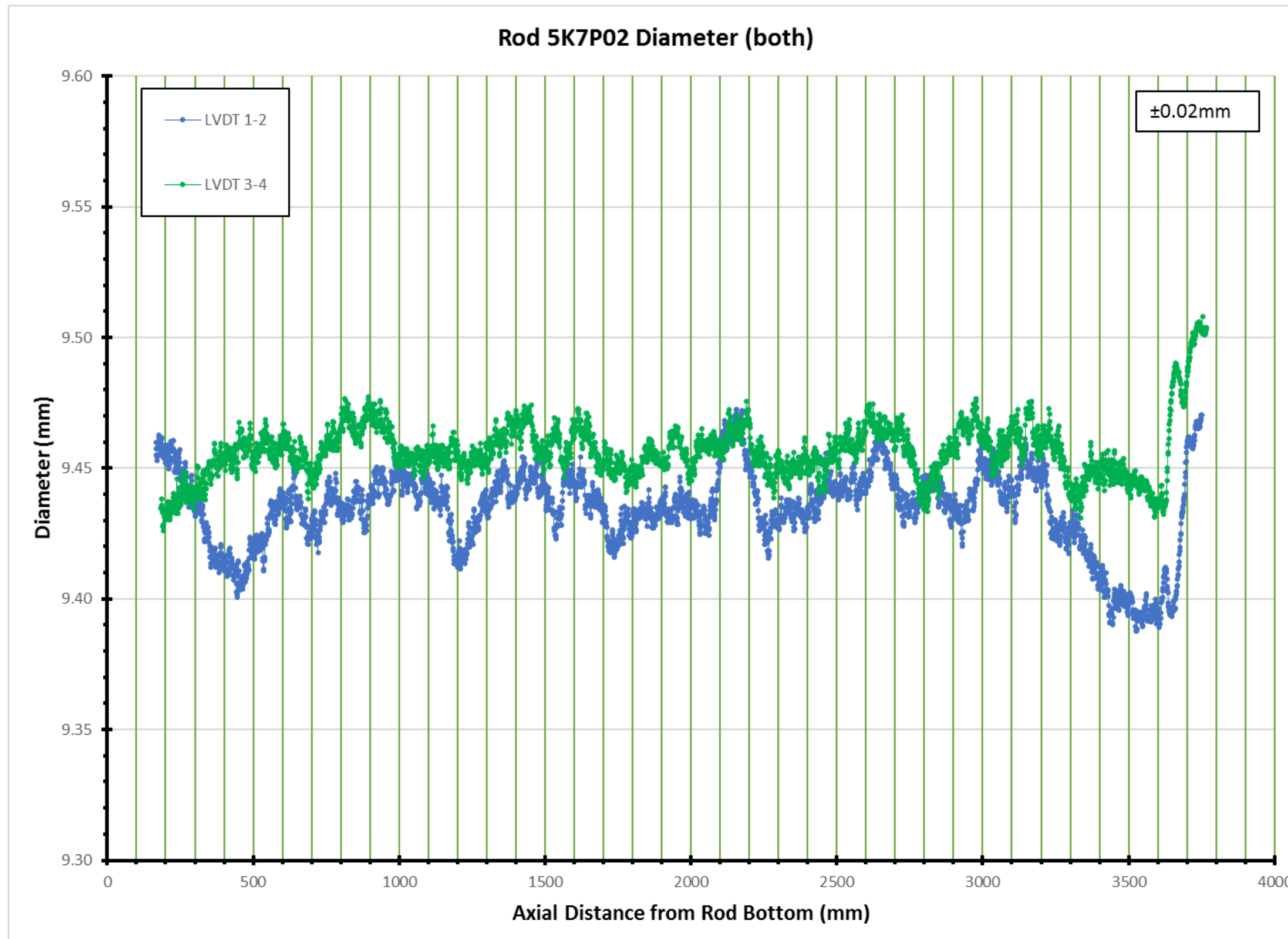


Figure A.11. Rod 5K7P02 LVDT Diameter Measurements.

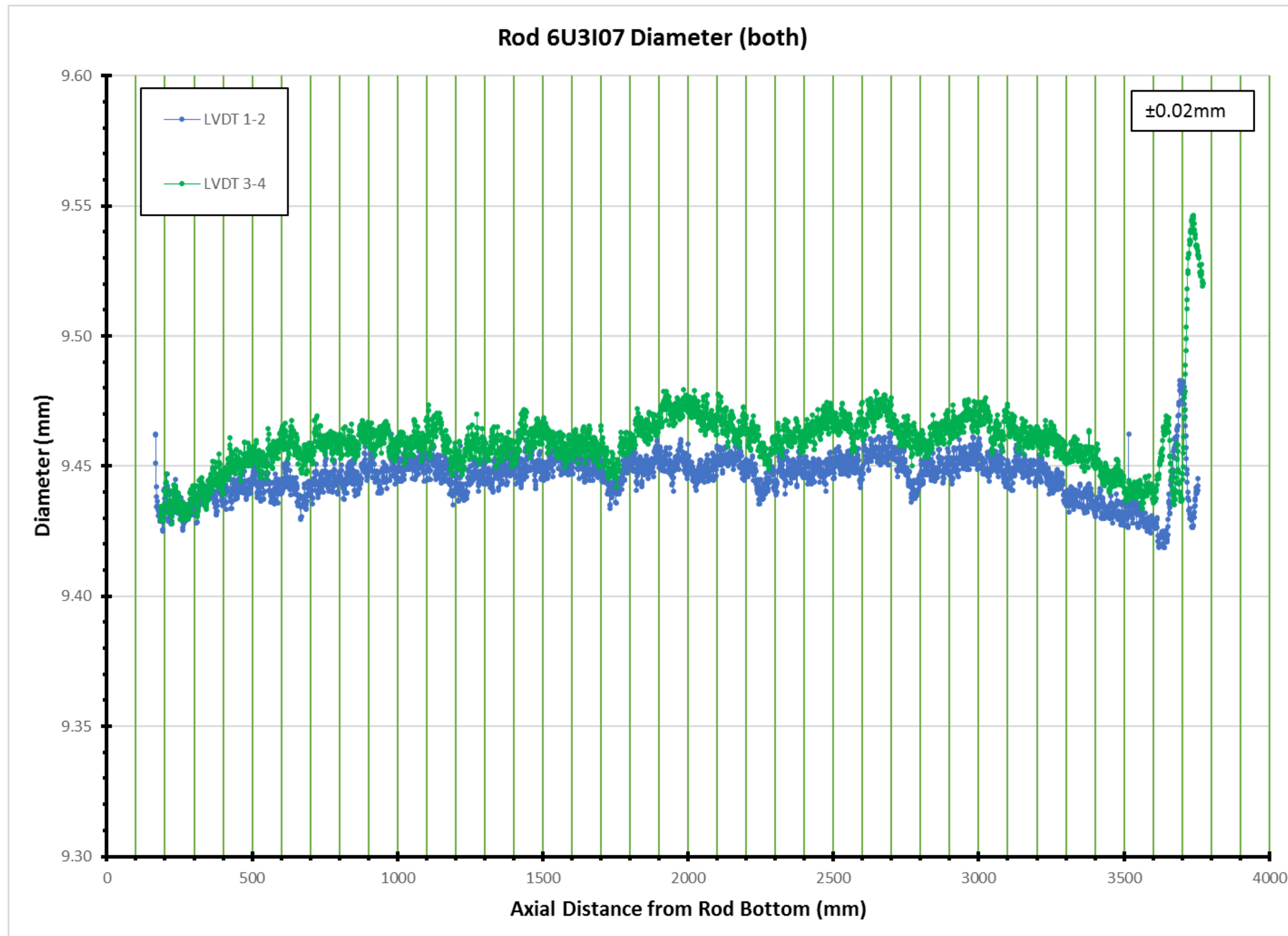


Figure A.12. Rod 6U3I07 LVDT Diameter Measurements.

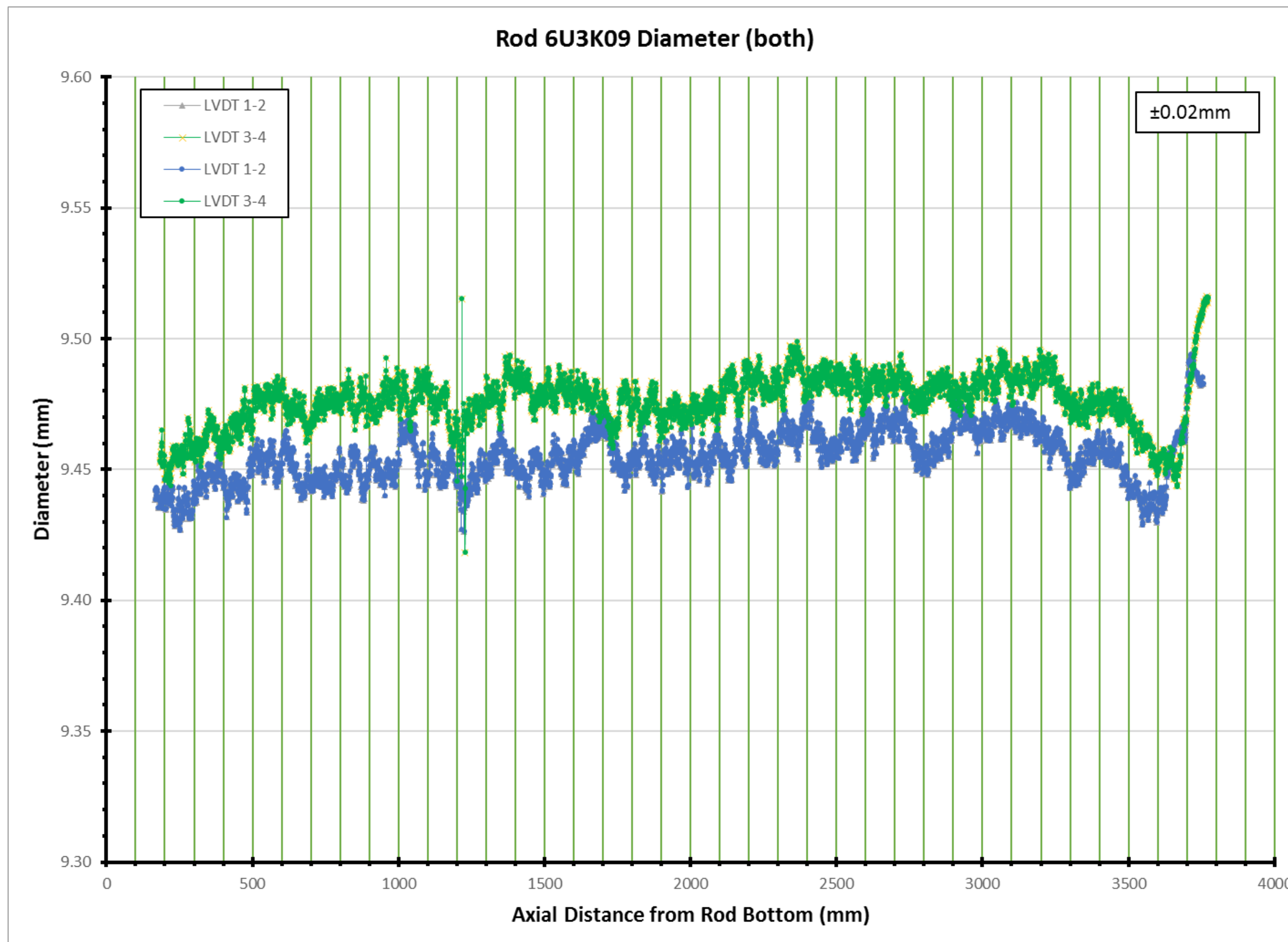


Figure A.13. Rod 6U3K09 LVDT Diameter Measurements.

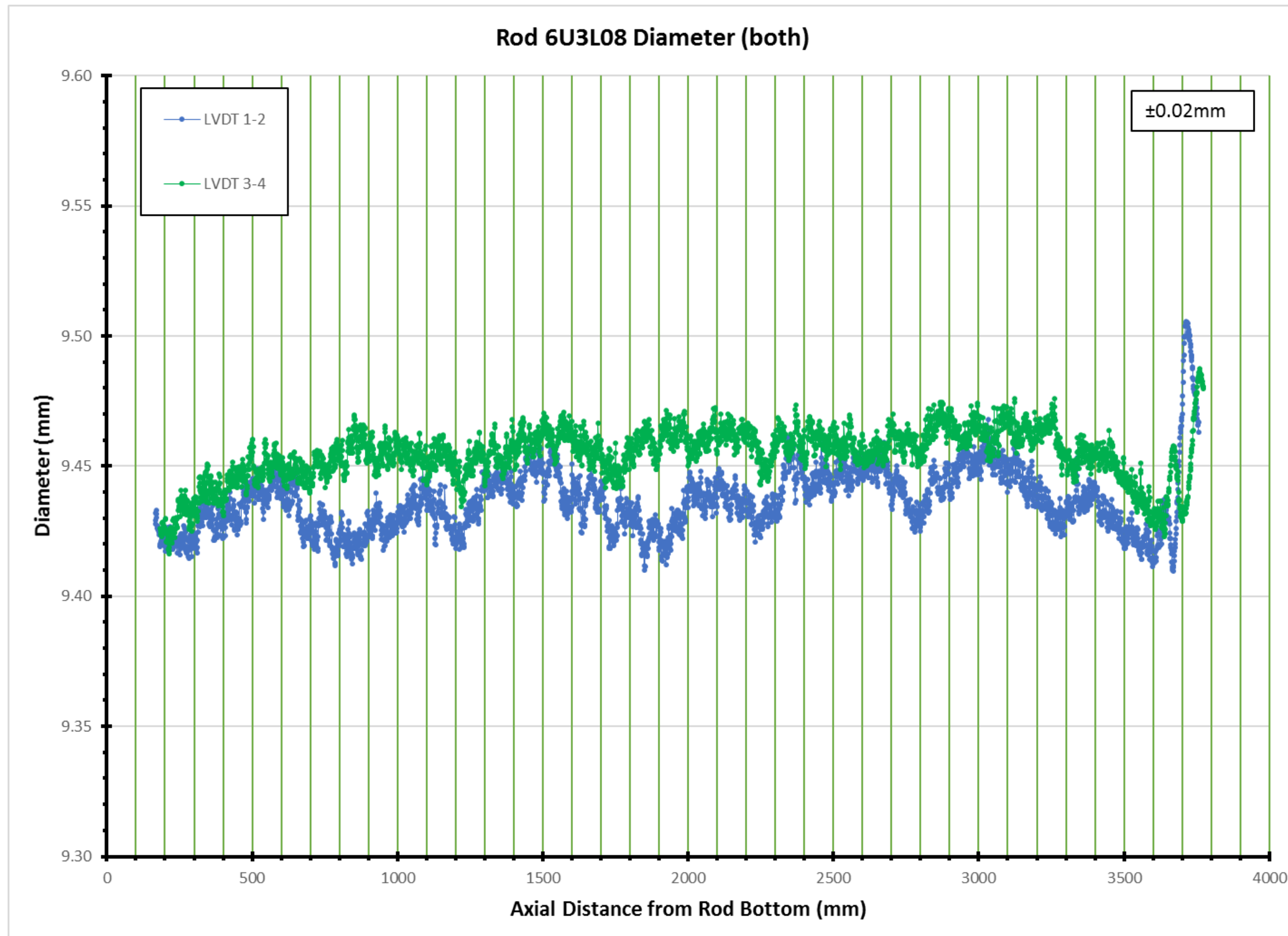


Figure A.14. Rod 6U3L08 LVDT Diameter Measurements.

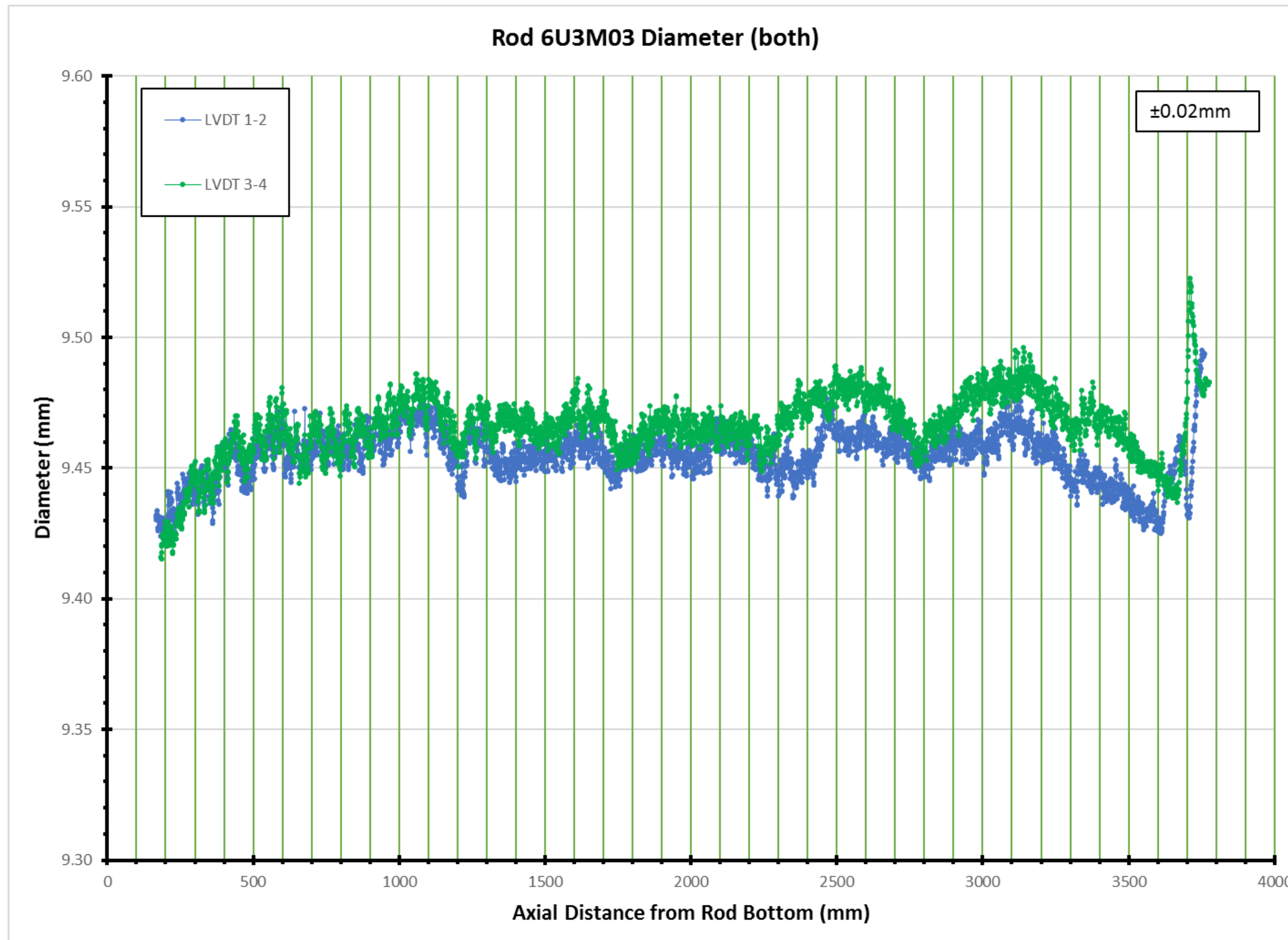


Figure A.15. Rod 6U3M03 LVDT Diameter Measurements.

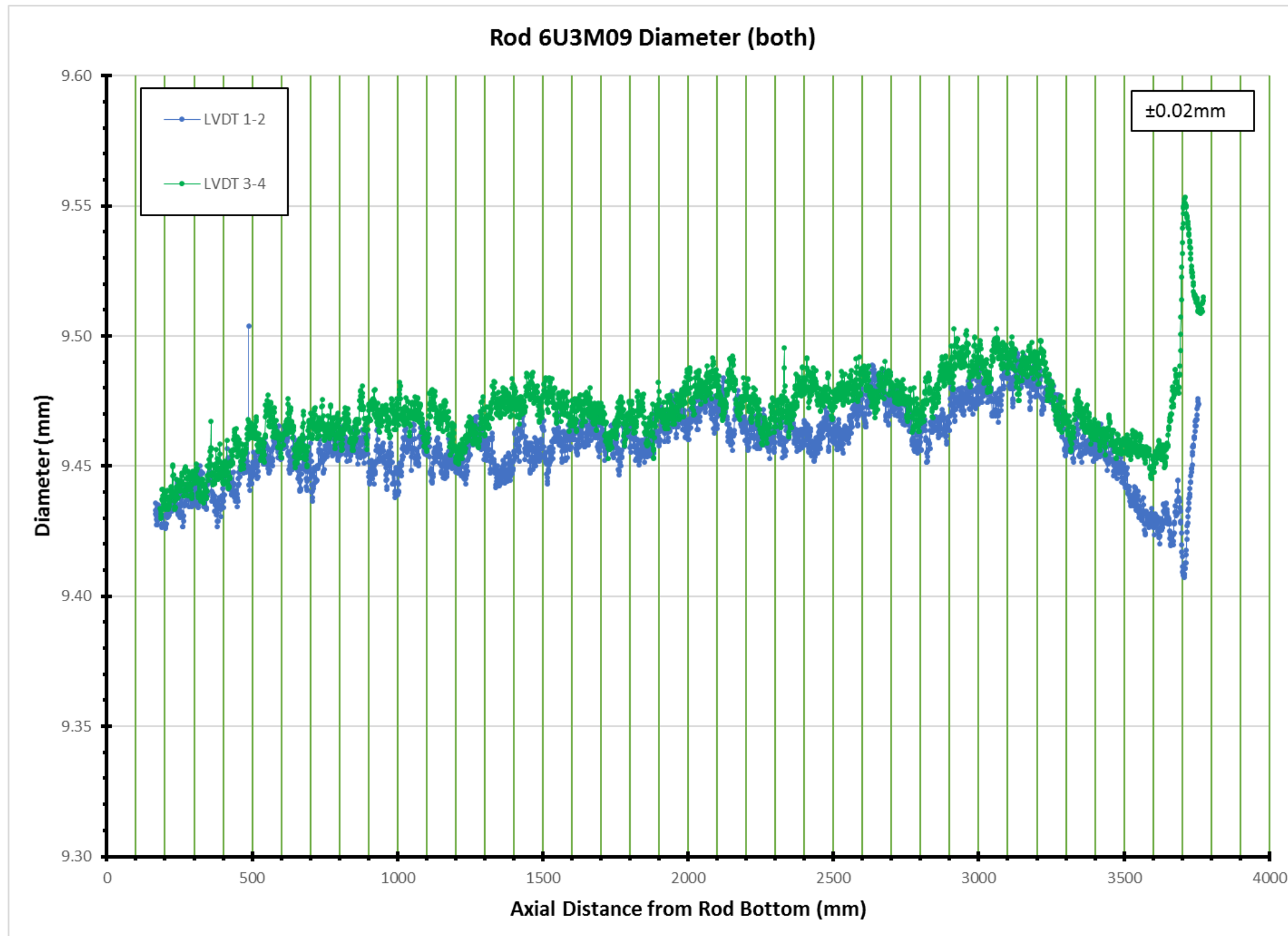


Figure A.16. Rod 6U3M09 LVDT Diameter Measurements.

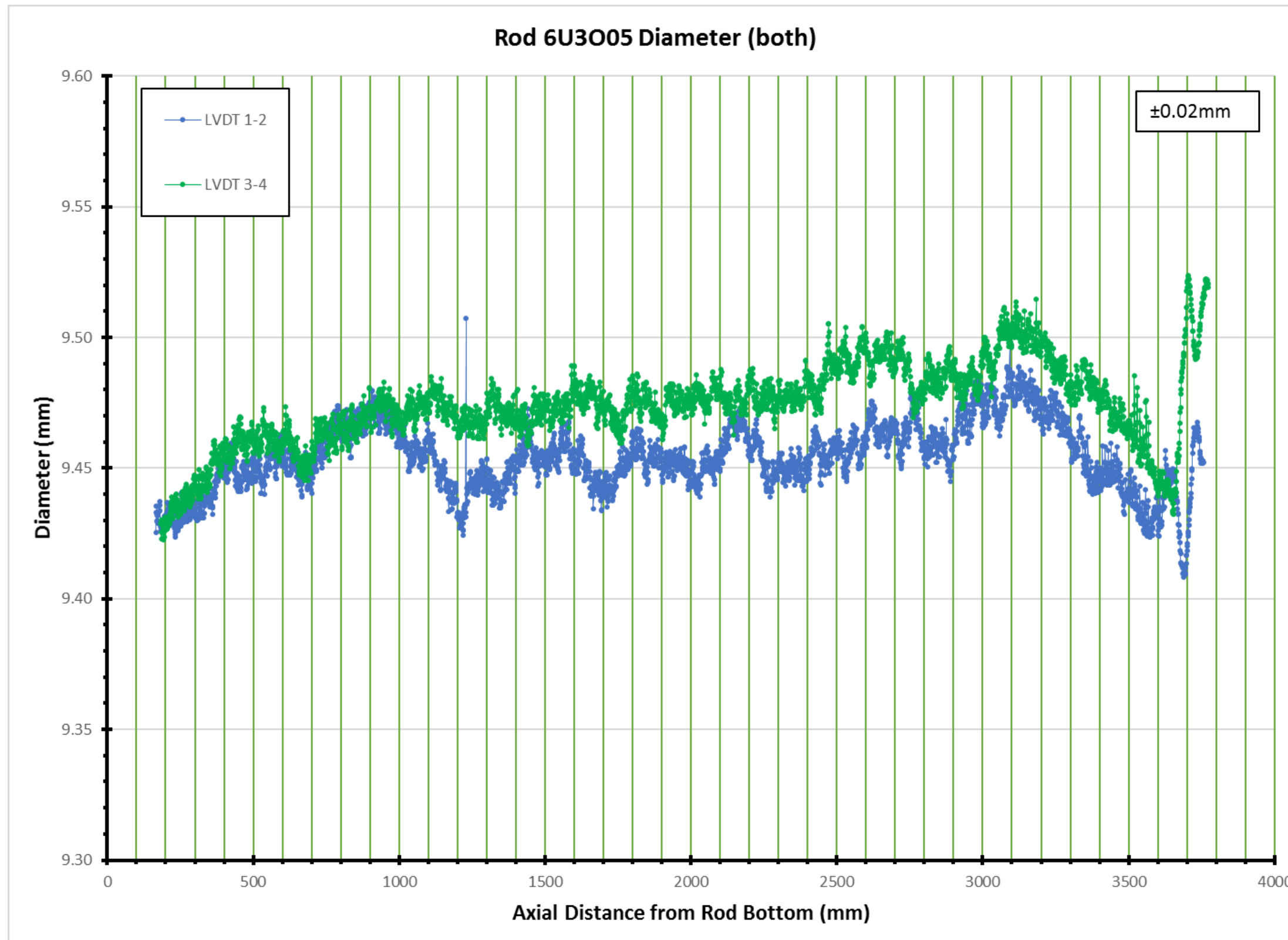


Figure A.17. Rod 6U3005 LVDT Diameter Measurements.

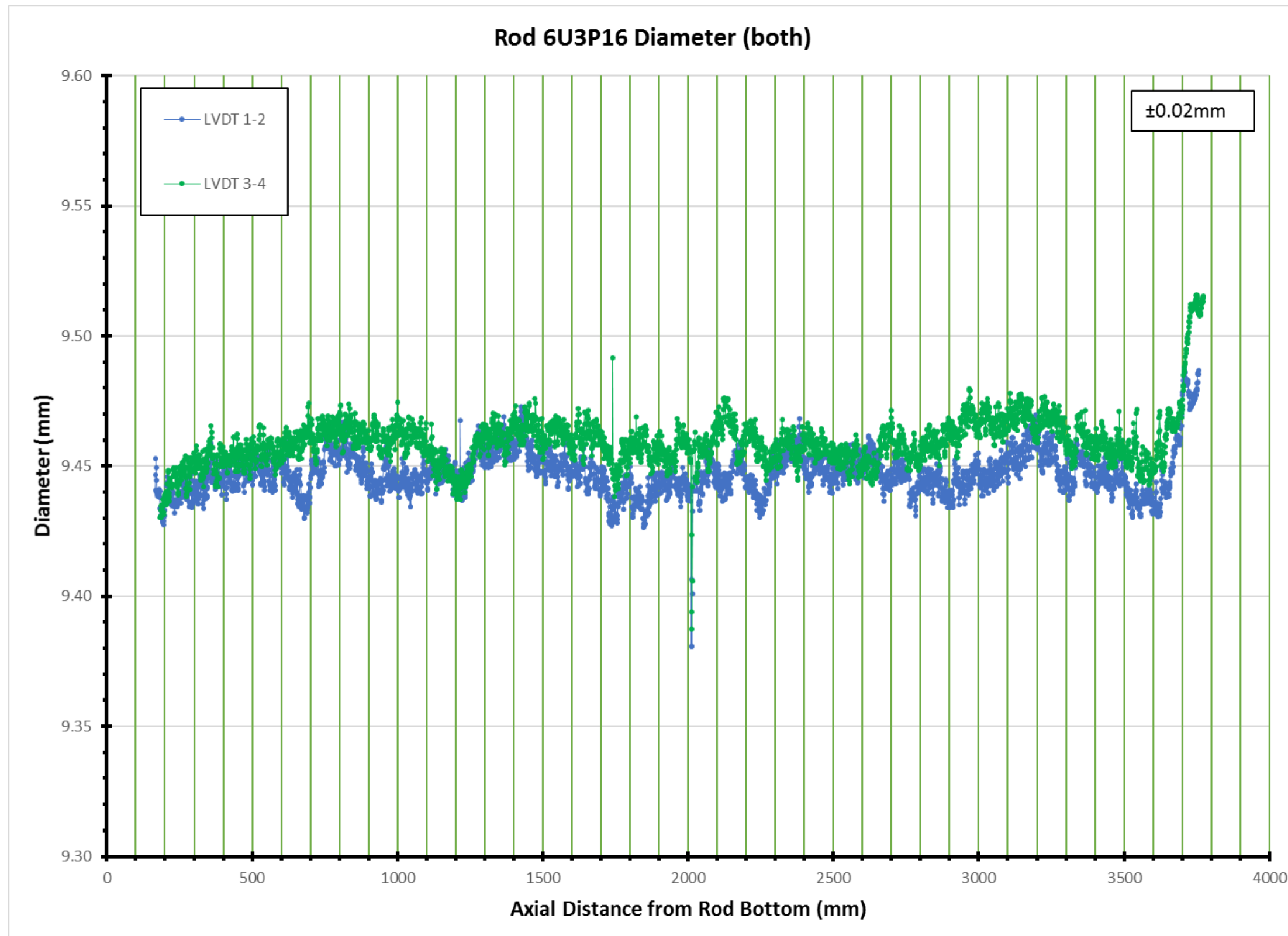


Figure A.18. Rod 6U3P16 LVDT Diameter Measurements.



Figure A.191 Rod 30AD05 LVDT Diameter Measurements.

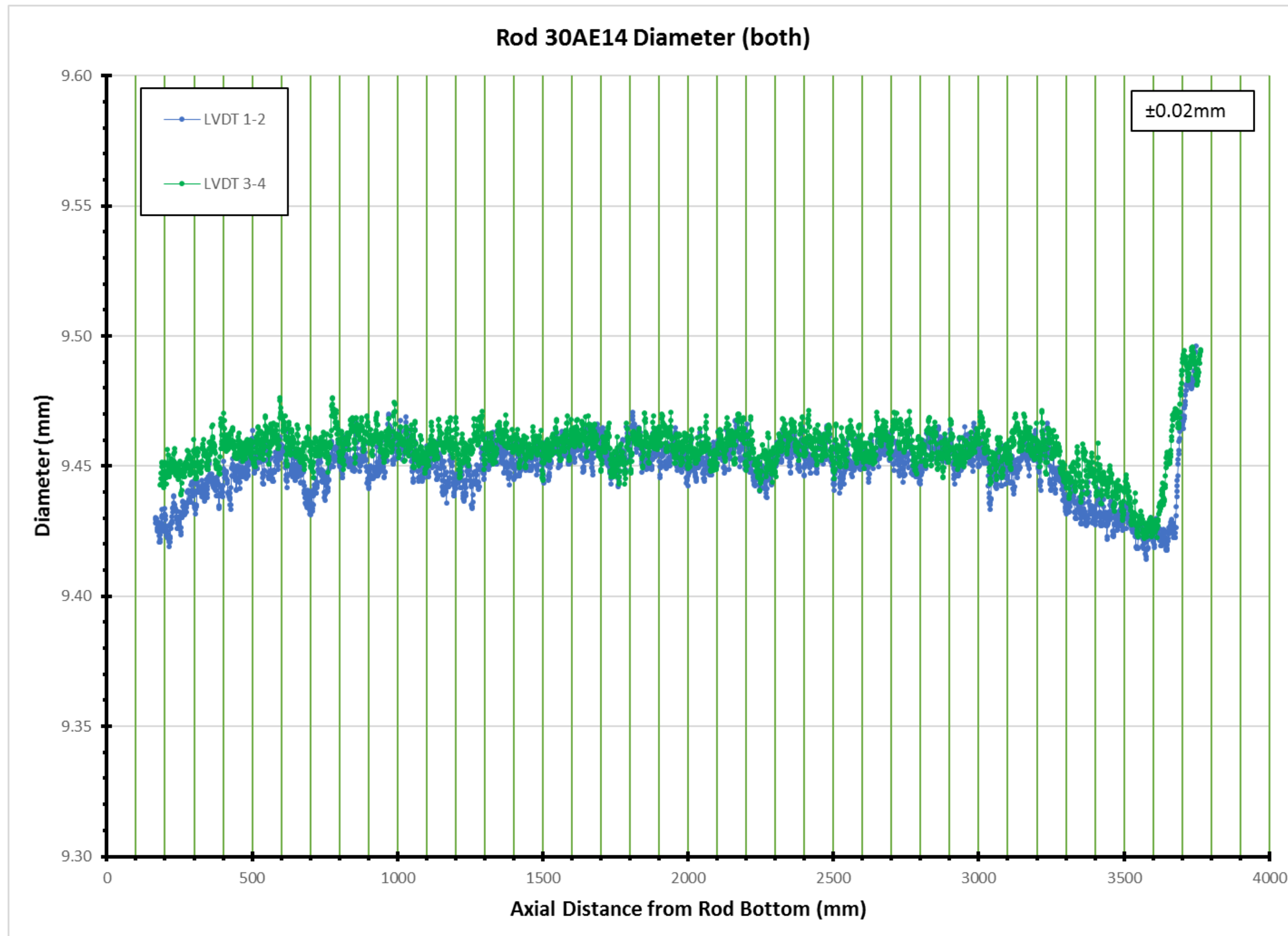


Figure A.20. Rod 30AE14 LVDT Diameter Measurements.



Figure A.21. Rod 30AG09 LVDT Diameter Measurements.

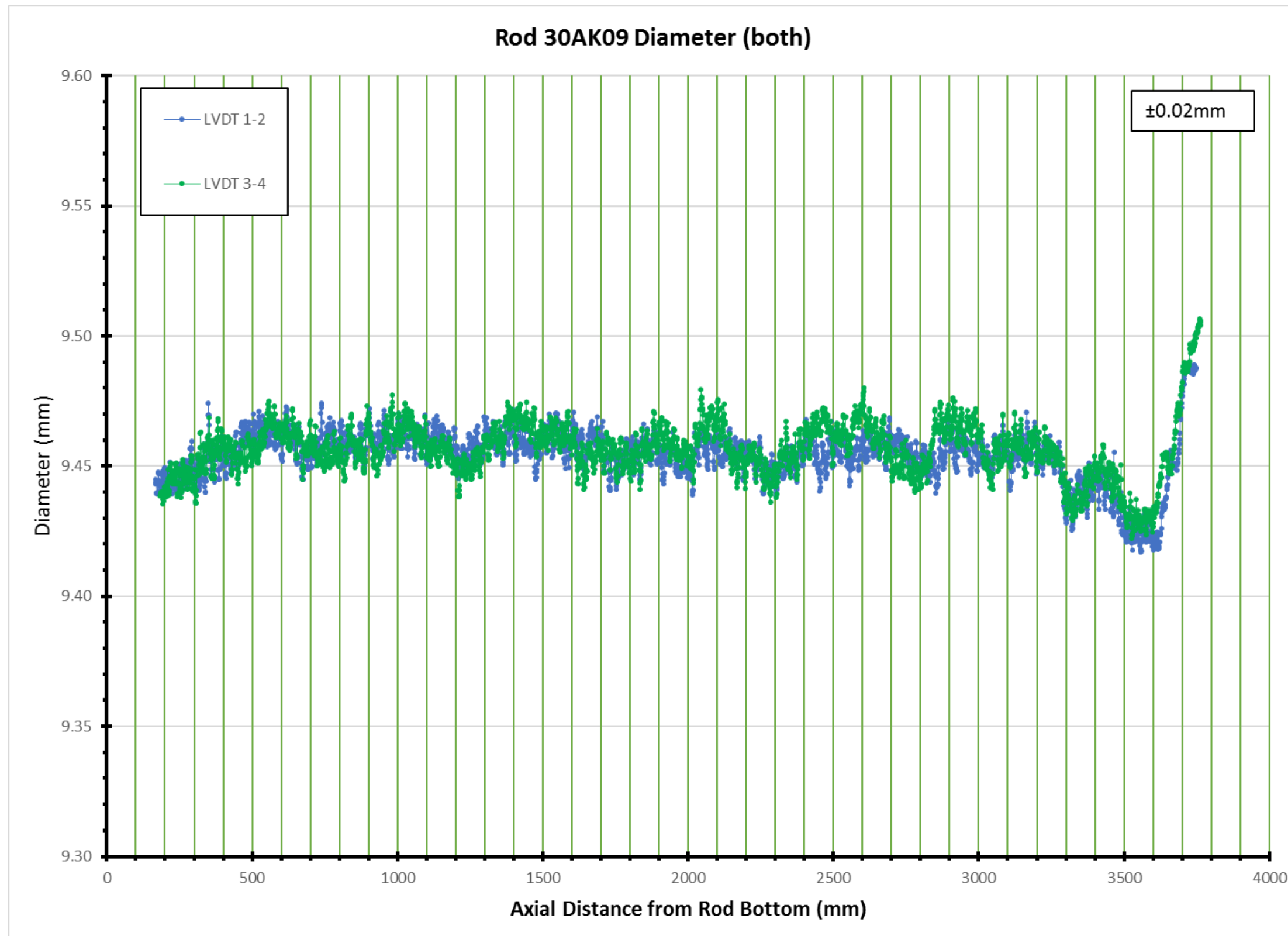


Figure A.22. Rod 30AK09 LVDT Diameter Measurements.

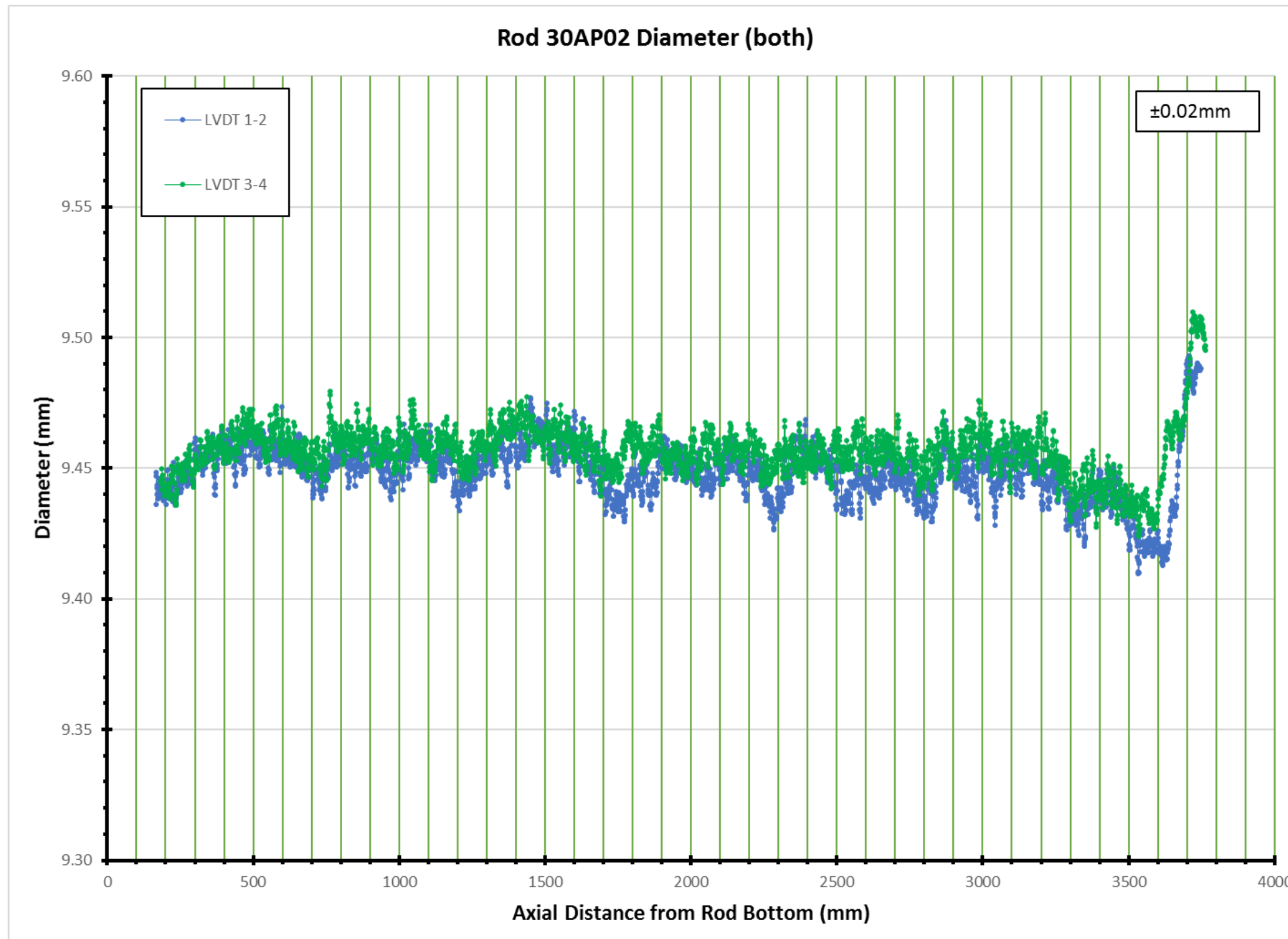


Figure A.23. Rod 30AP02 LVDT Diameter Measurements.

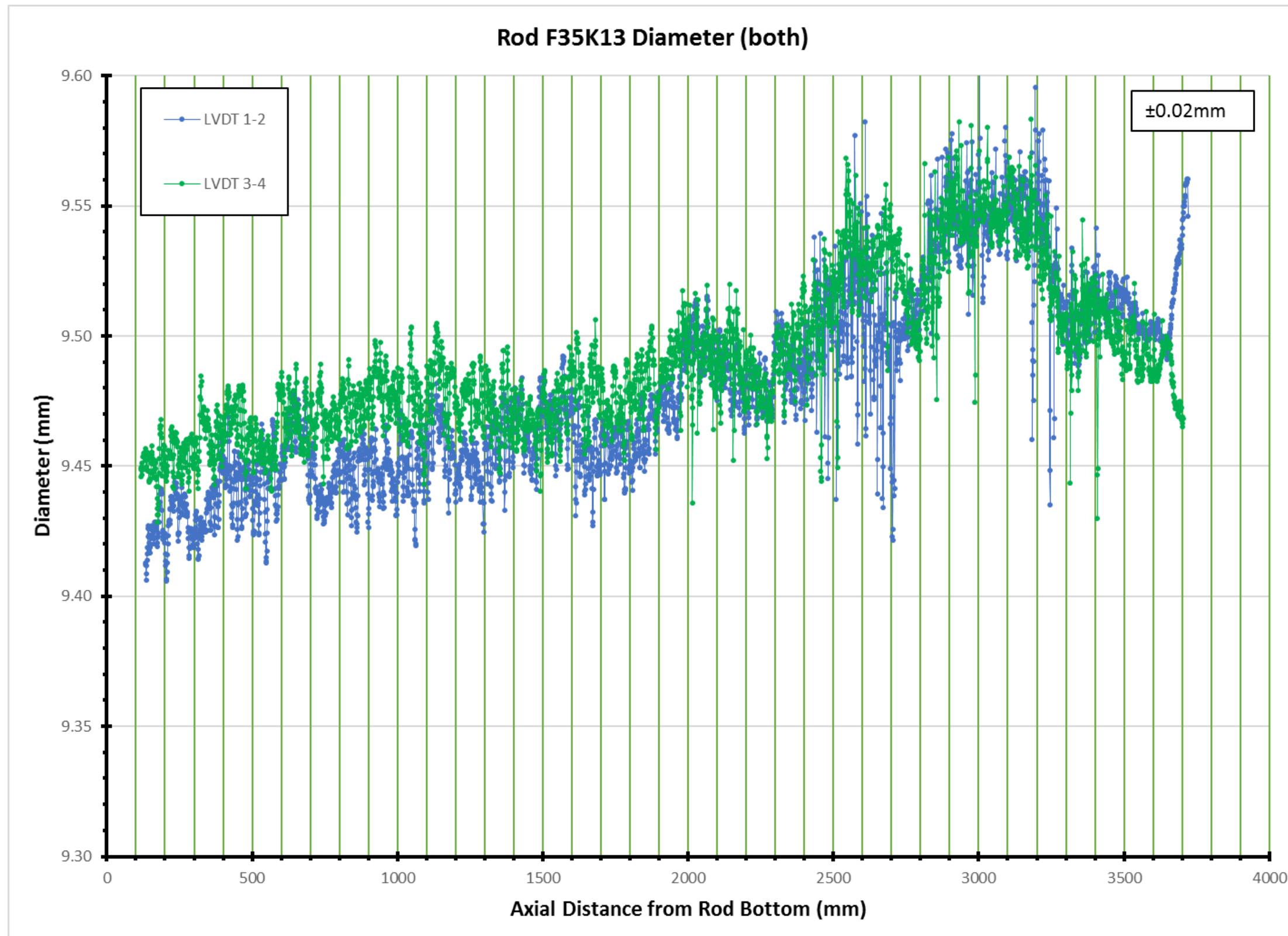


Figure A.24. Rod F35K13 LVDT Diameter Measurements.

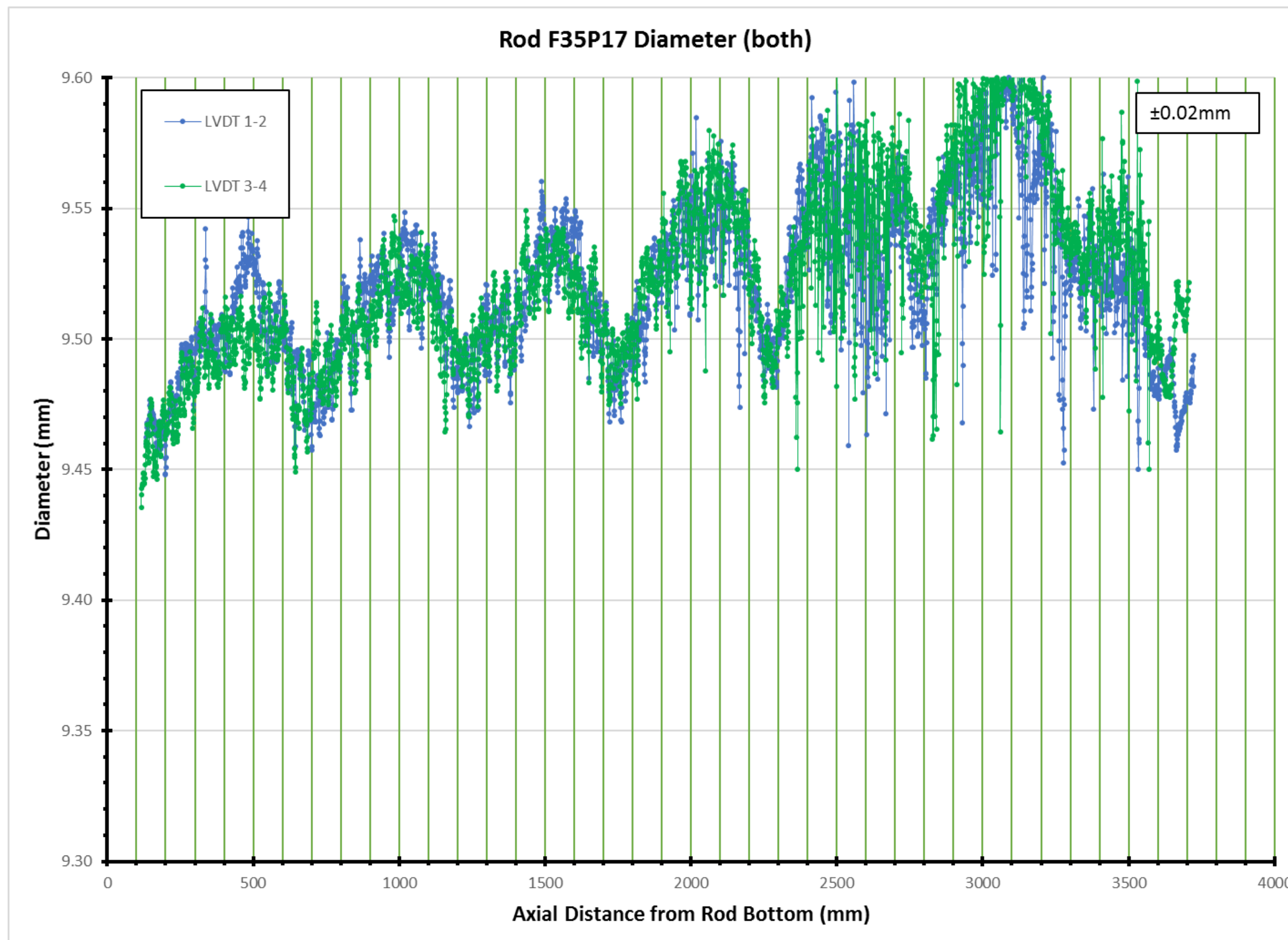


Figure A.25. Rod F35P17 LVDT Diameter Measurements.

Appendix B

Gamma Scan, Average LVDT Profilometry, and Visual Profilometry Feature Comparison

Figures B-1 through B-25 show the overlay of gamma scan data with the LVDT average diameter measurements and visually derived diameter measurements for each rod. Rod angular orientation is random, so there is no information that can be related back to a specific operational rod orientation in its fuel assembly.

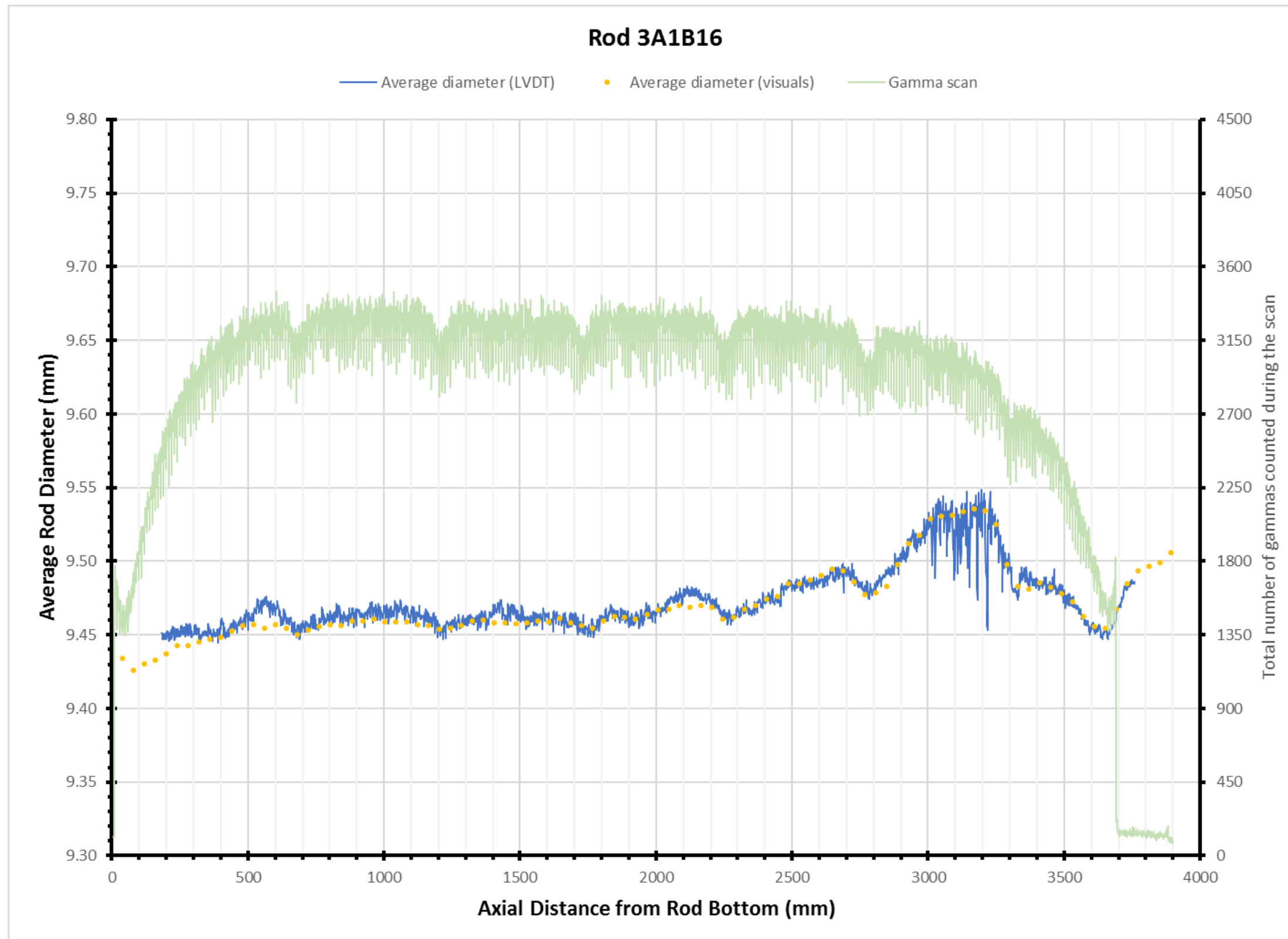


Figure B.1. Rod 3A1B16 LVDT Profilometry, Visual Profilometry, and Gamma Scan Data.

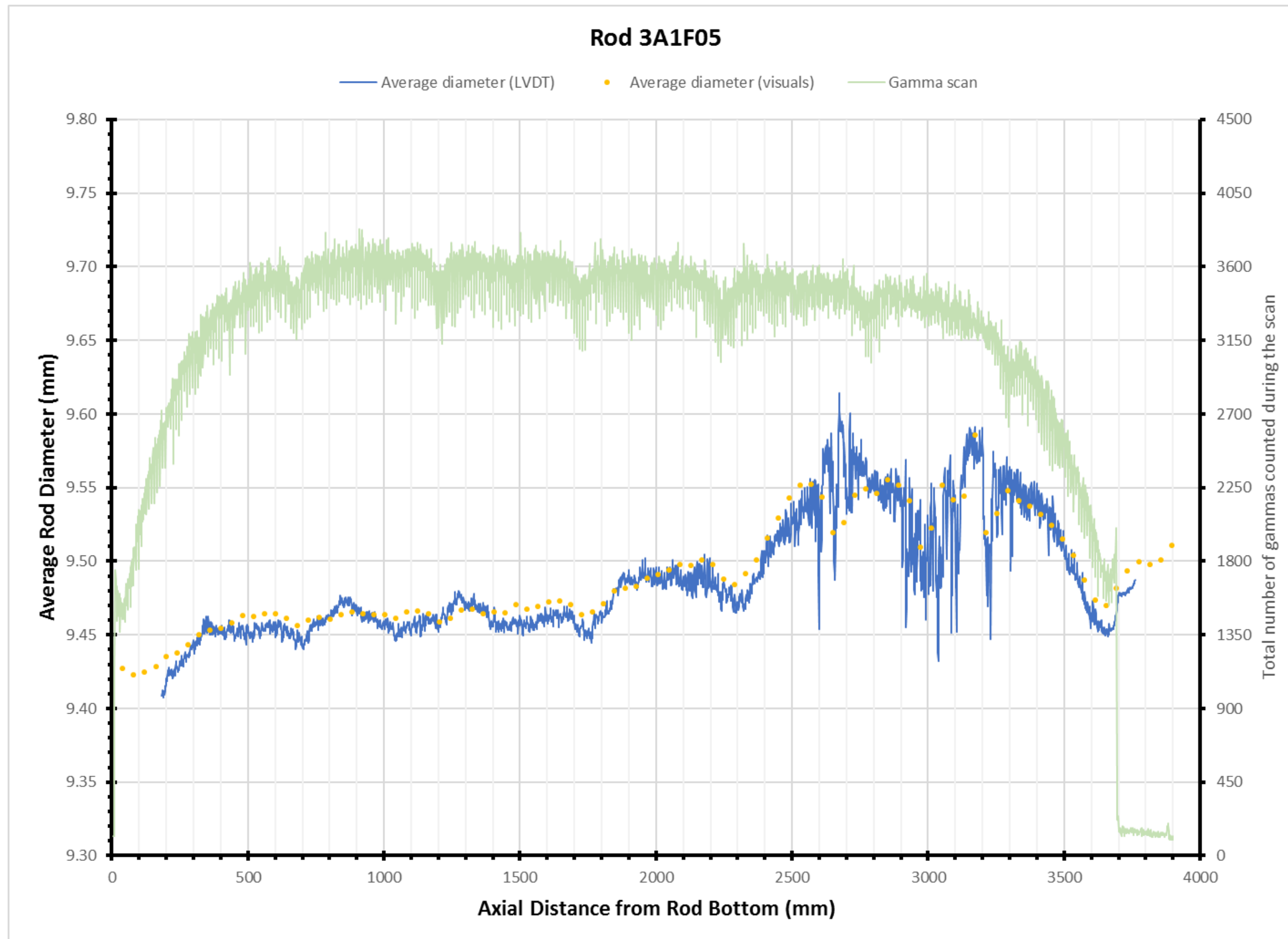


Figure B.2. Rod 3A1F05 LVDT Profilometry, Visual Profilometry, and Gamma Scan Data.

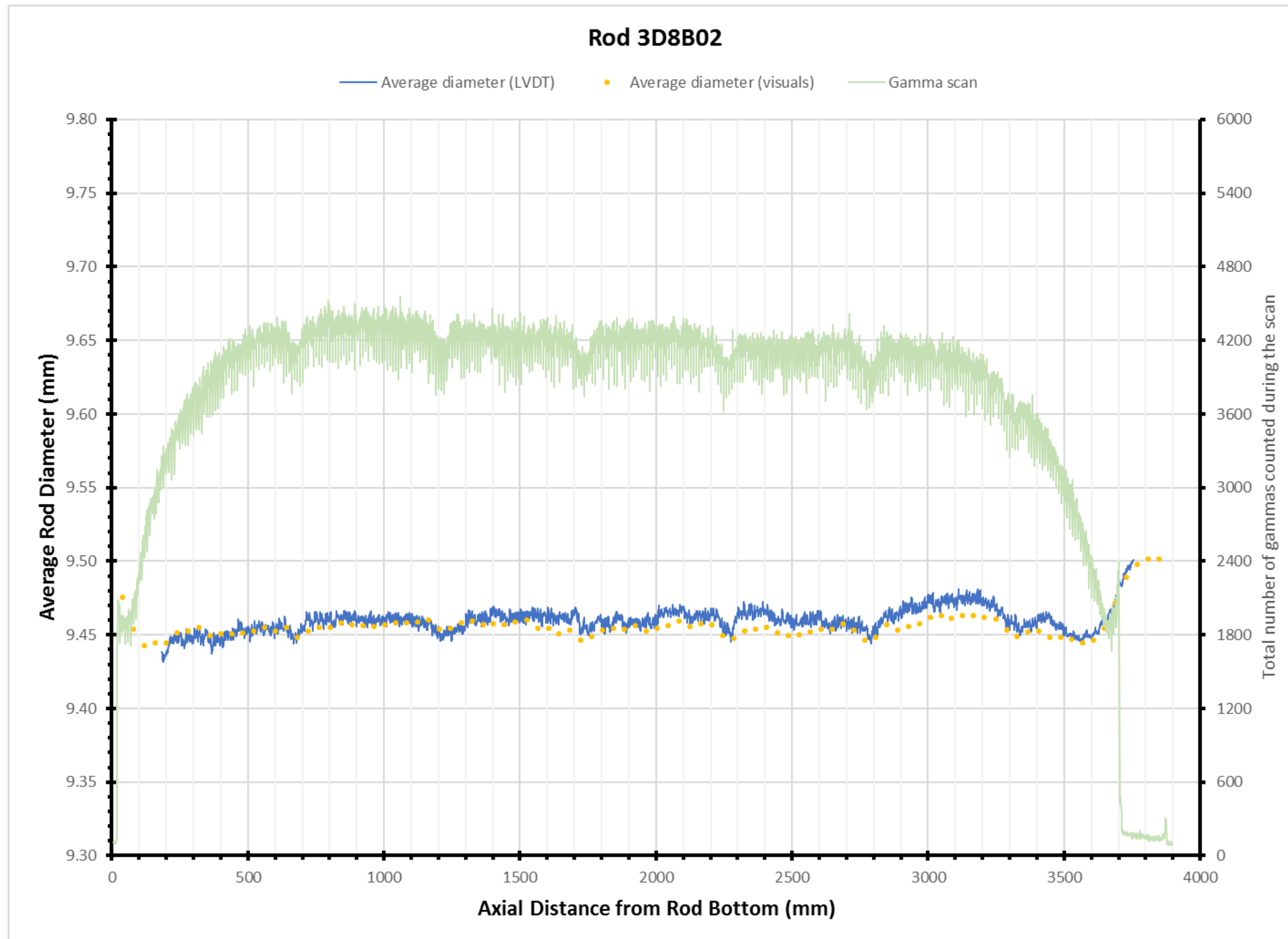


Figure B.3. Rod 3D8B02 LVDT Profilometry, Visual Profilometry, and Gamma Scan Data.

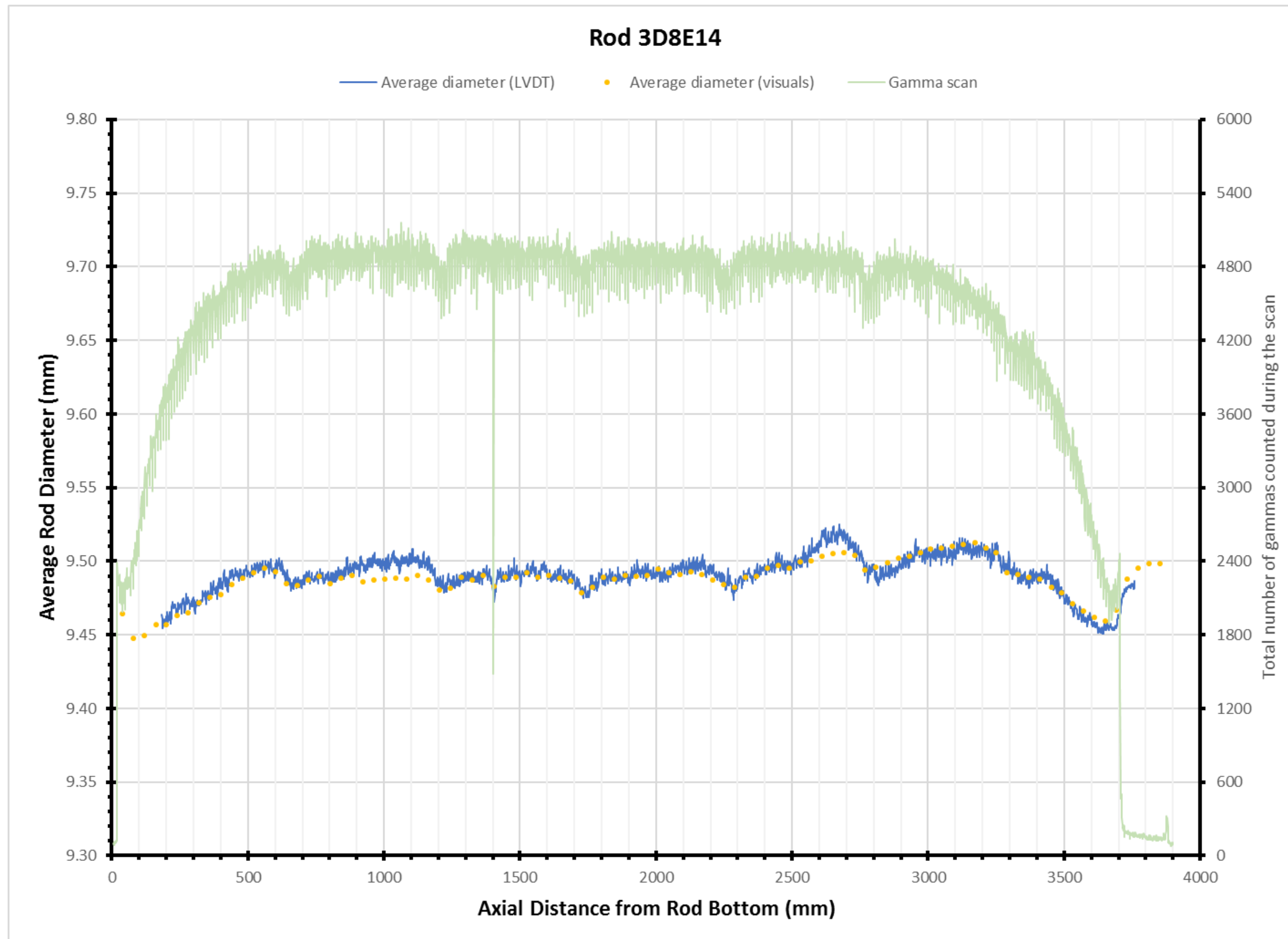


Figure B.4. Rod 3D8E14 LVDT Profilometry, Visual Profilometry, and Gamma Scan Data.

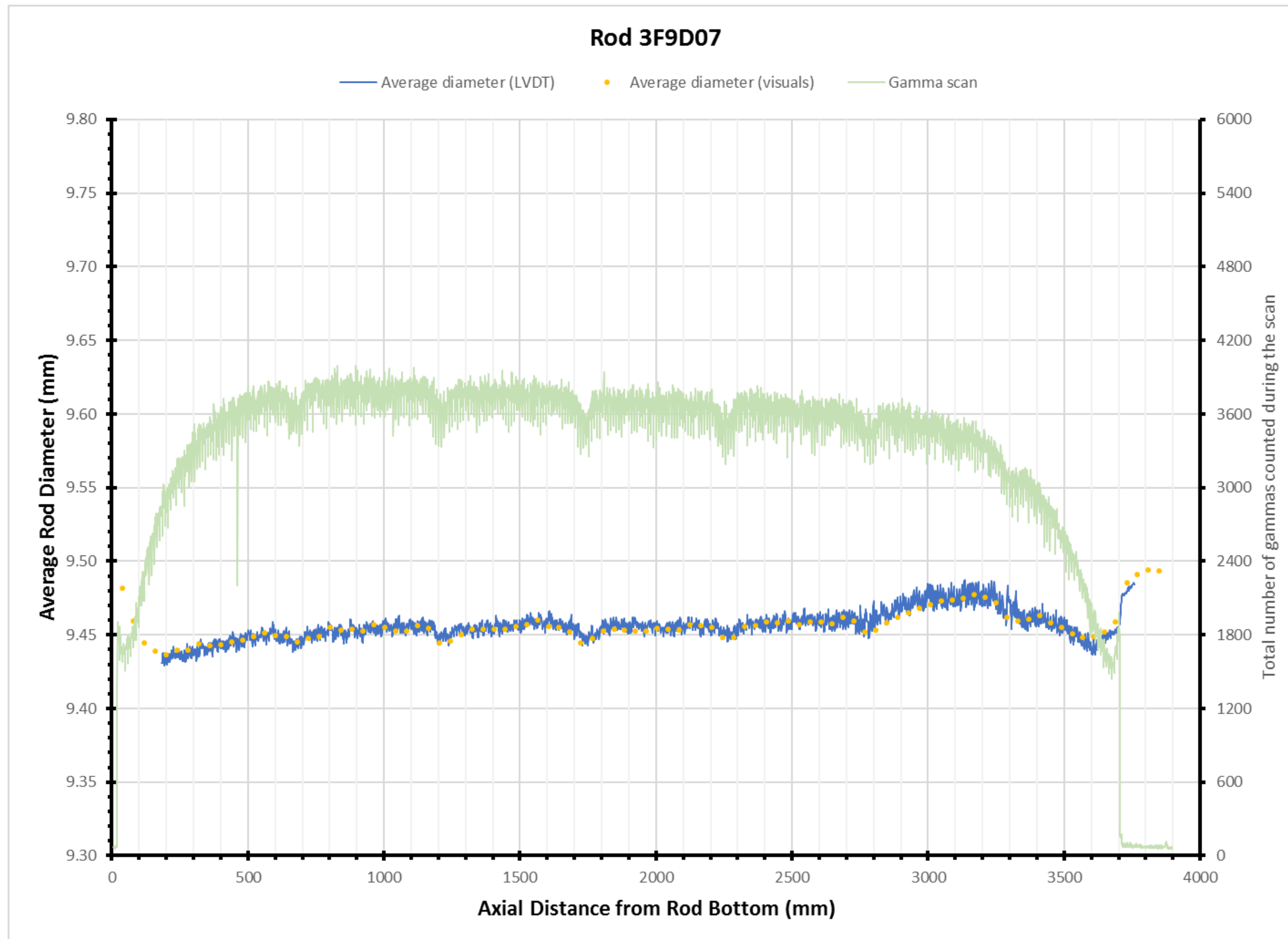


Figure B.5. Rod 3F9D07 LVDT Profilometry, Visual Profilometry, and Gamma Scan Data.

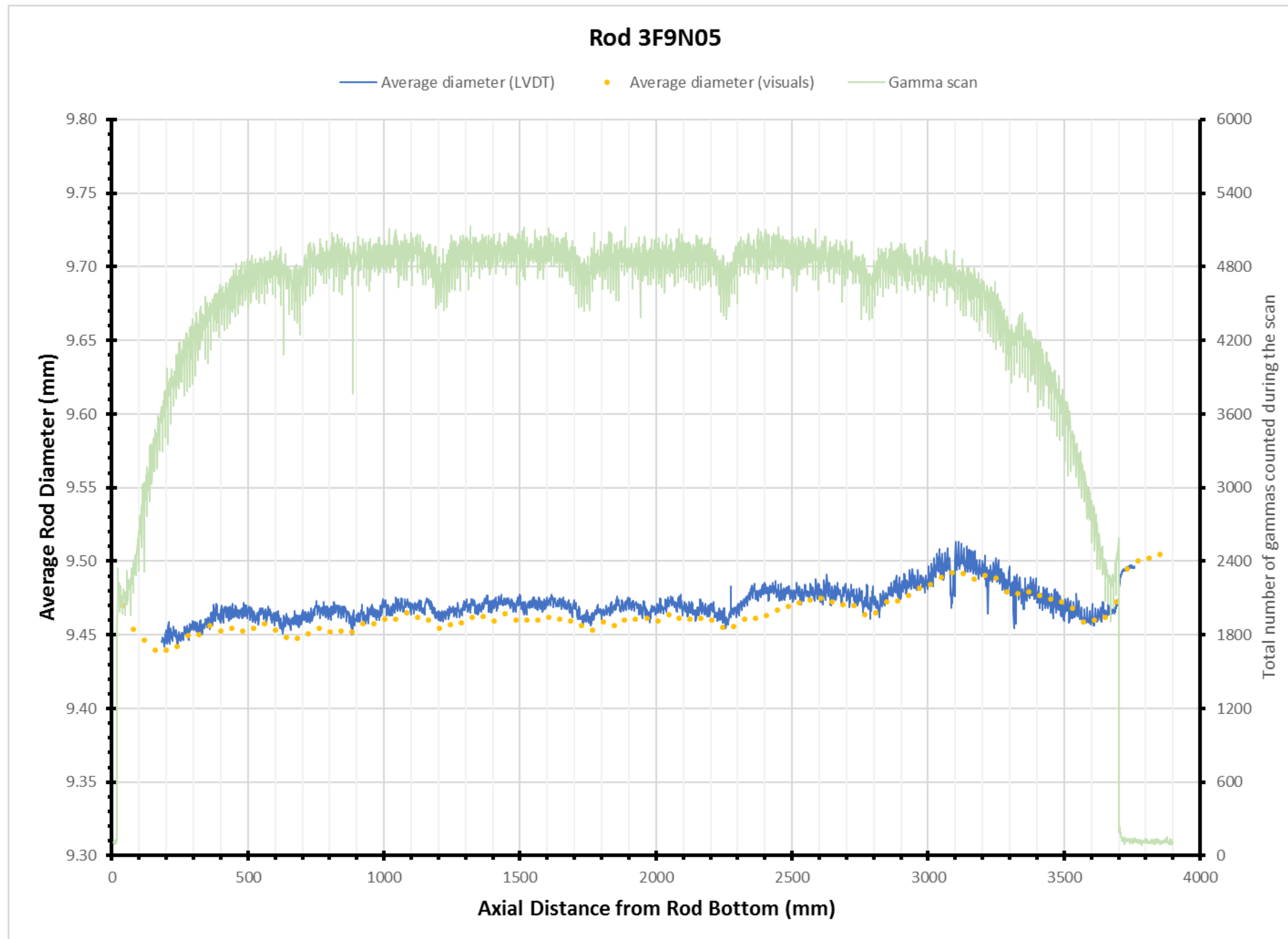


Figure B.6. Rod 3F9N05 LVDT Profilometry, Visual Profilometry, and Gamma Scan Data.

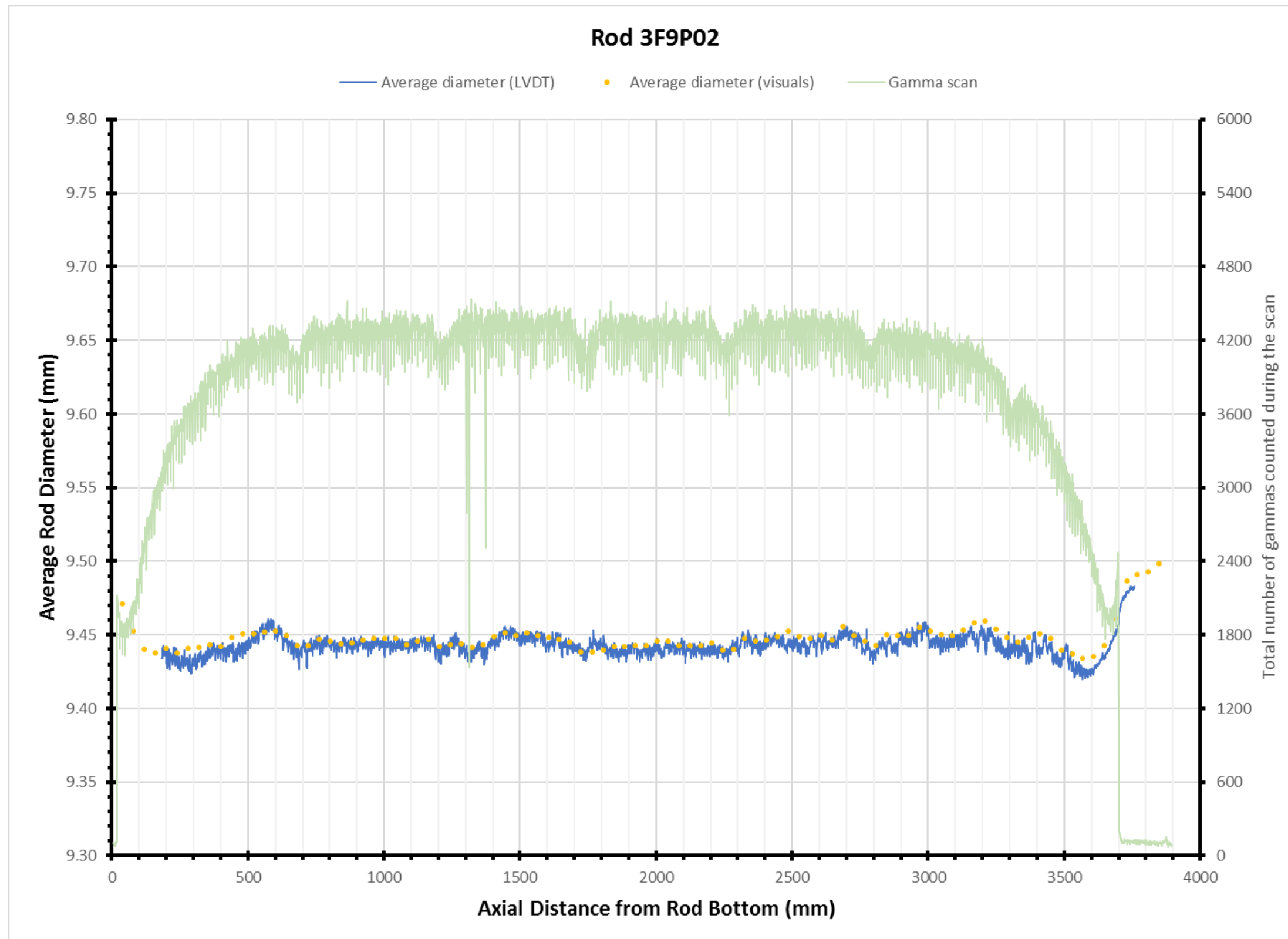


Figure B.7. Rod 3F9P02 LVDT Profilometry, Visual Profilometry, and Gamma Scan Data.

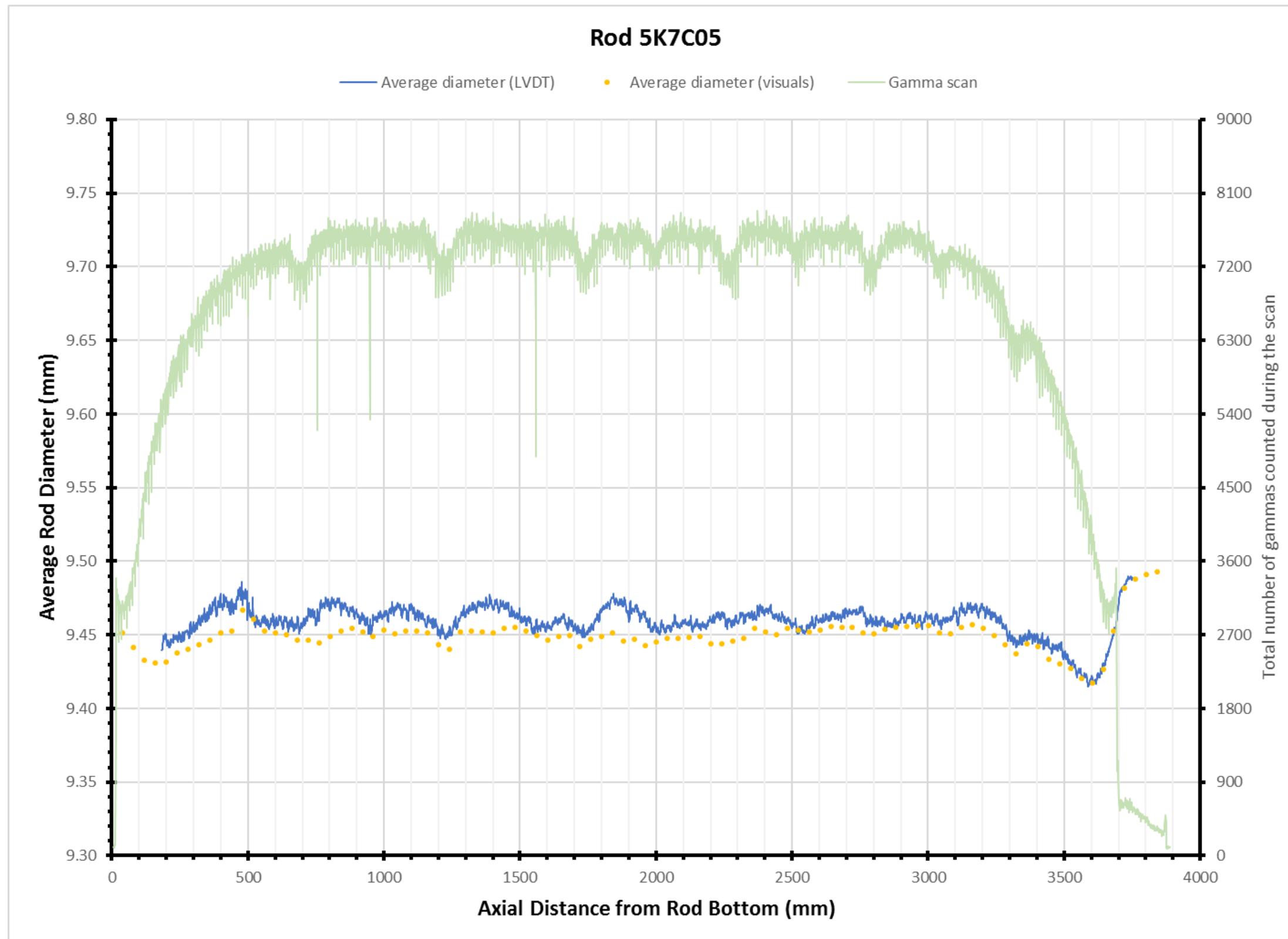


Figure B.8. Rod 5K7C05 LVDT Profilometry, Visual Profilometry, and Gamma Scan Data.

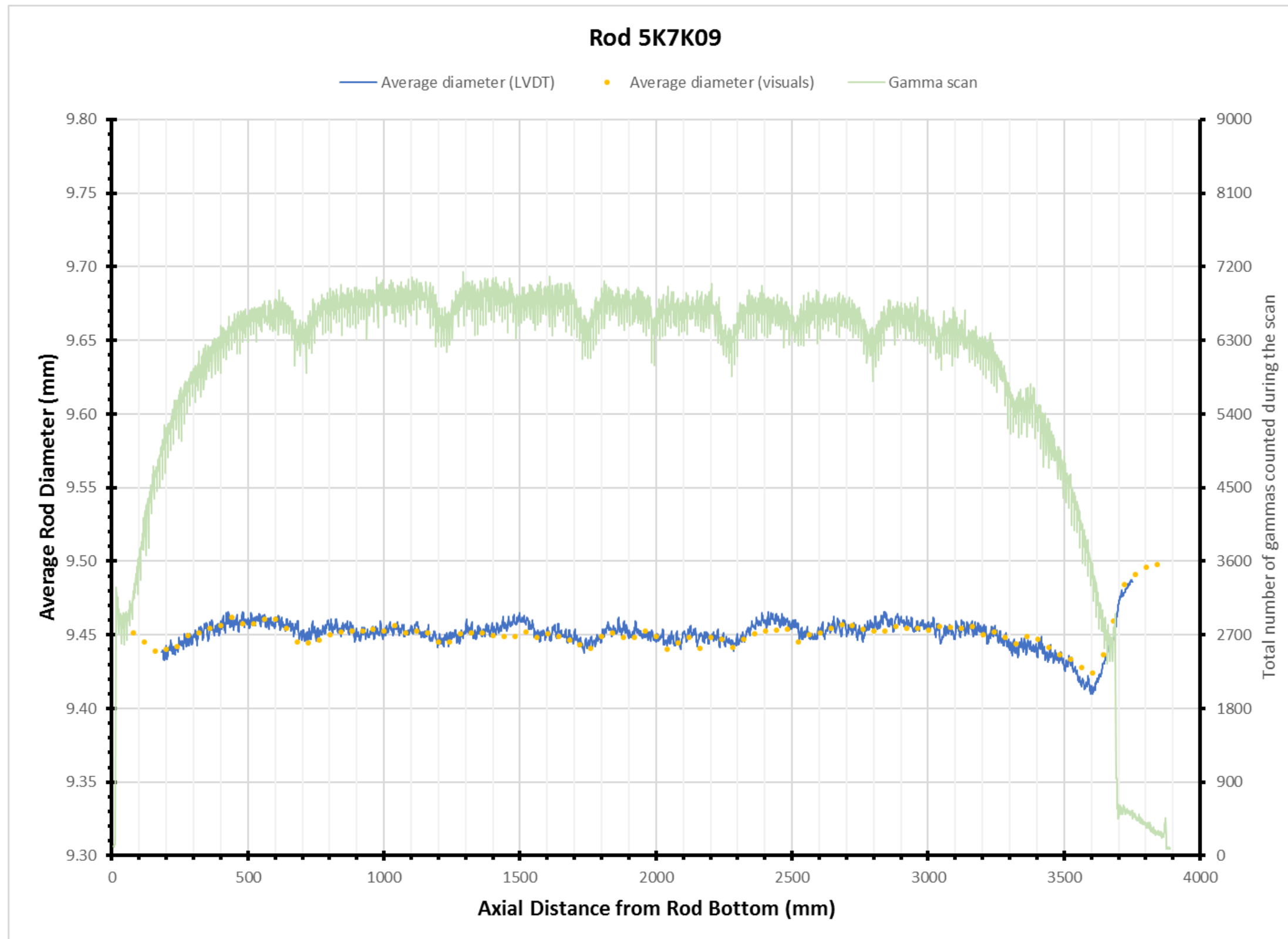


Figure B.9. Rod 5K7K09 LVDT Profilometry, Visual Profilometry, and Gamma Scan Data.

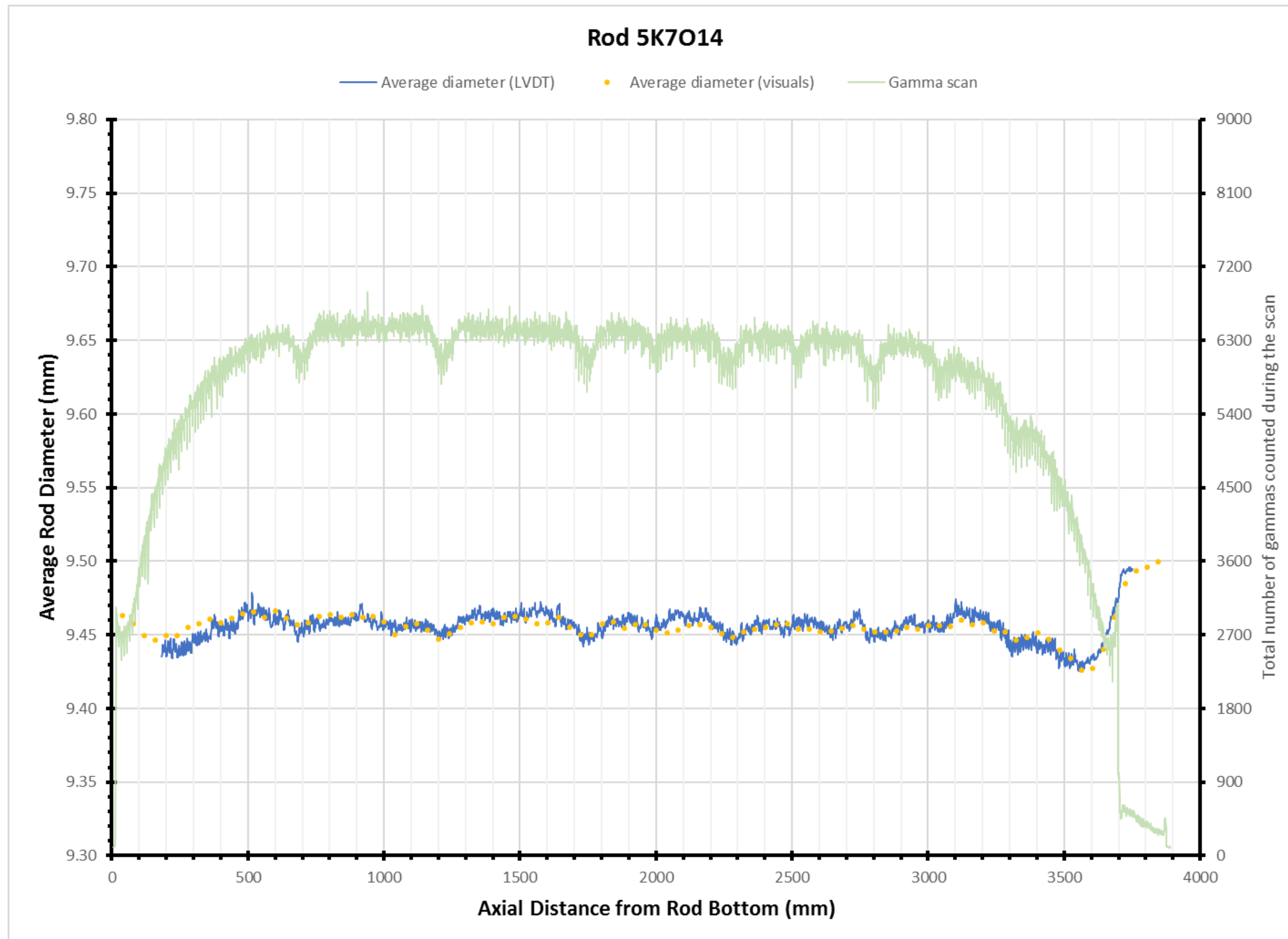


Figure B.10. Rod 5K7014 LVDT Profilometry, Visual Profilometry, and Gamma Scan Data.

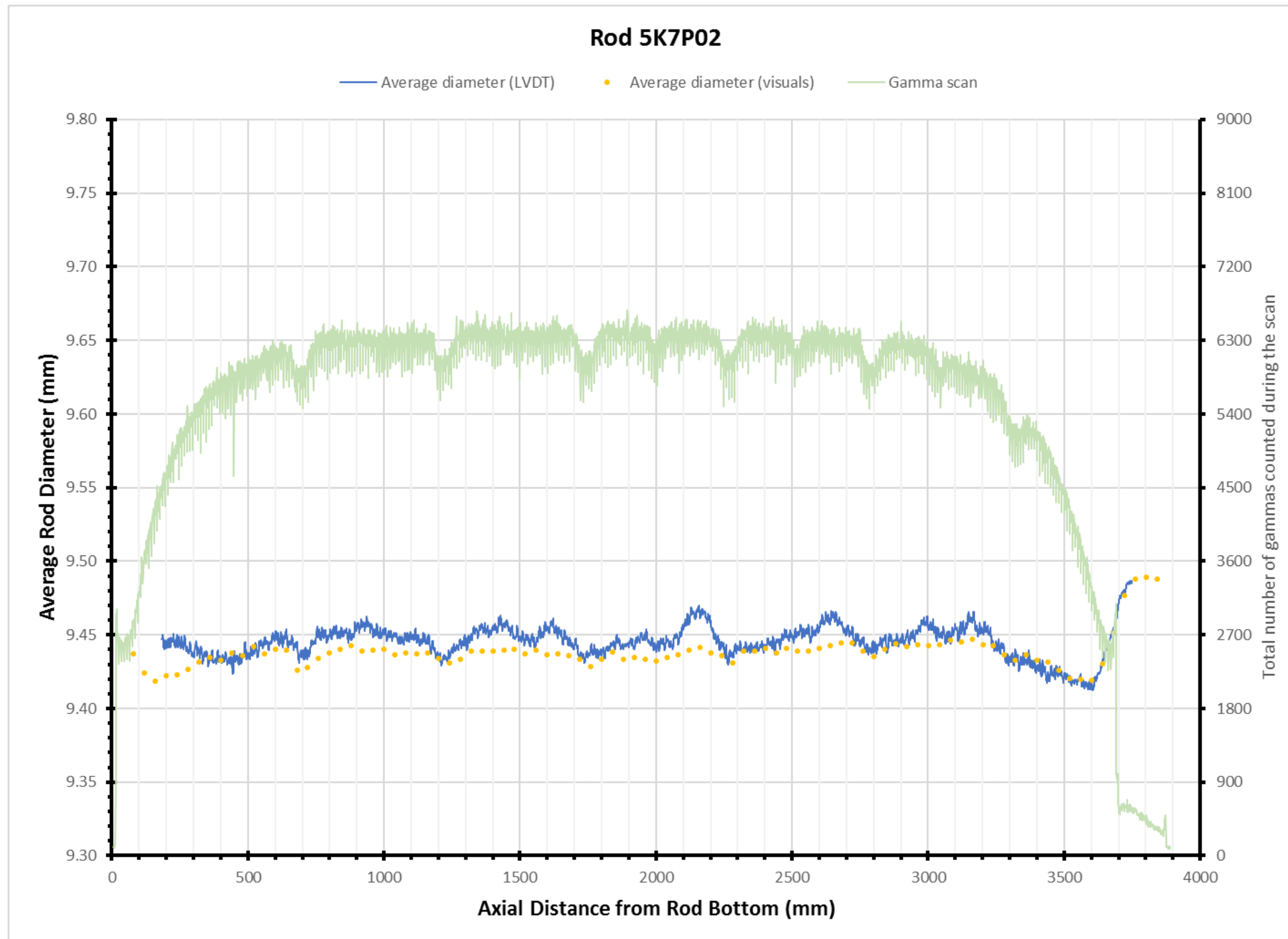


Figure B.11. Rod 5K7P02 LVDT Profilometry, Visual Profilometry, and Gamma Scan Data.

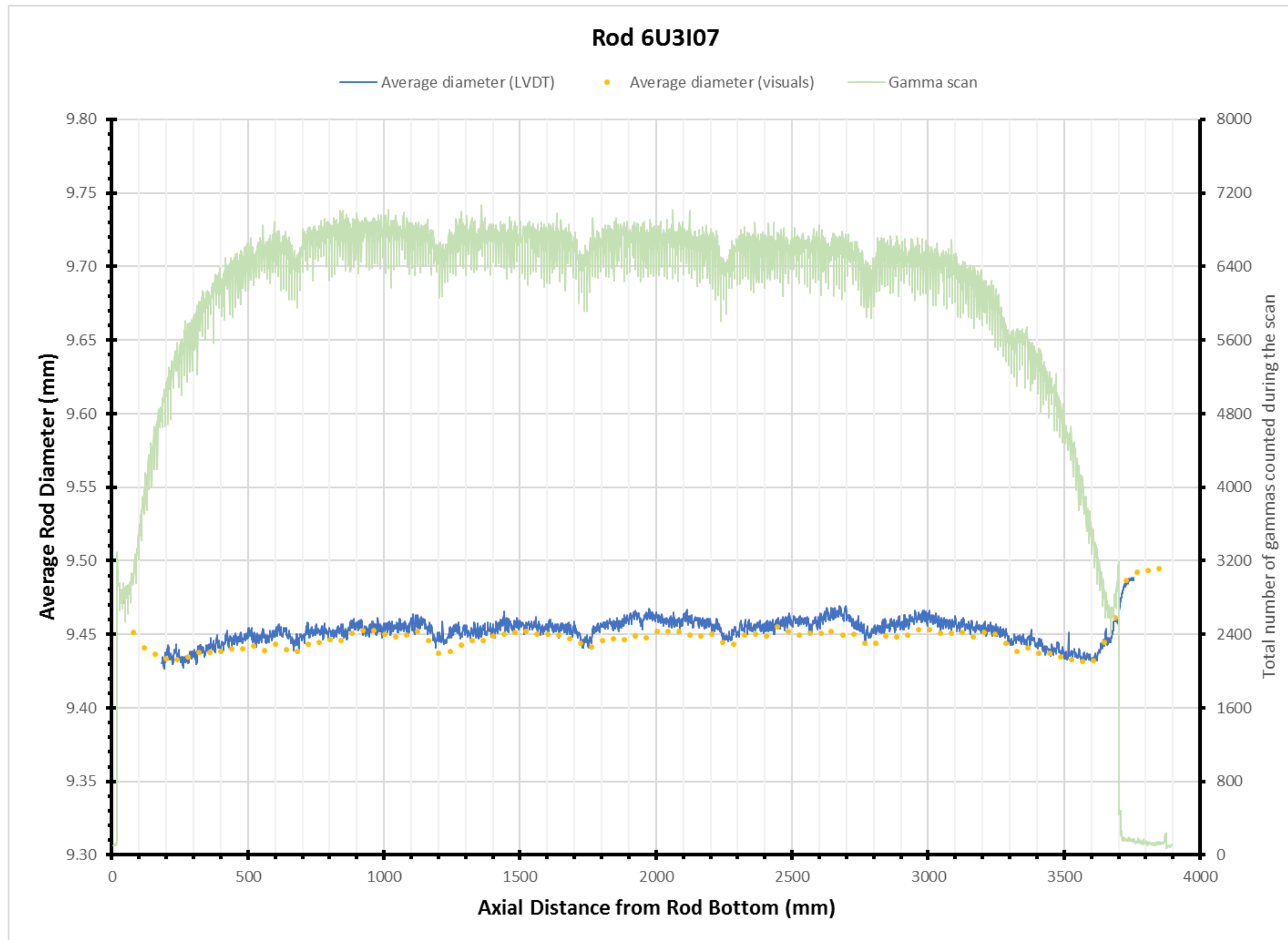


Figure B.12. Rod 6U3I07 LVDT Profilometry, Visual Profilometry, and Gamma Scan Data.

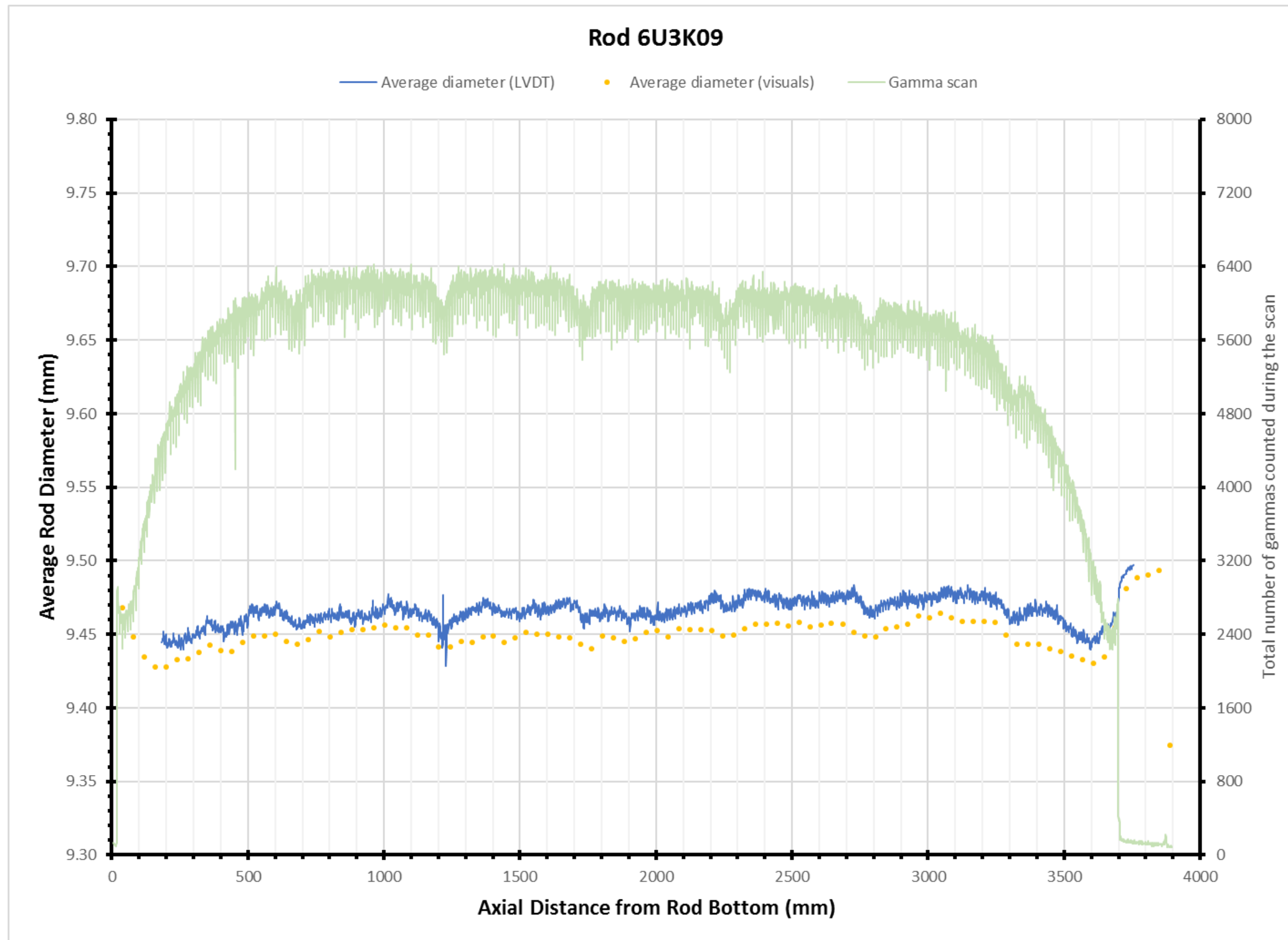


Figure B.13. Rod 6U3K09 LVDT Profilometry, Visual Profilometry, and Gamma Scan Data.

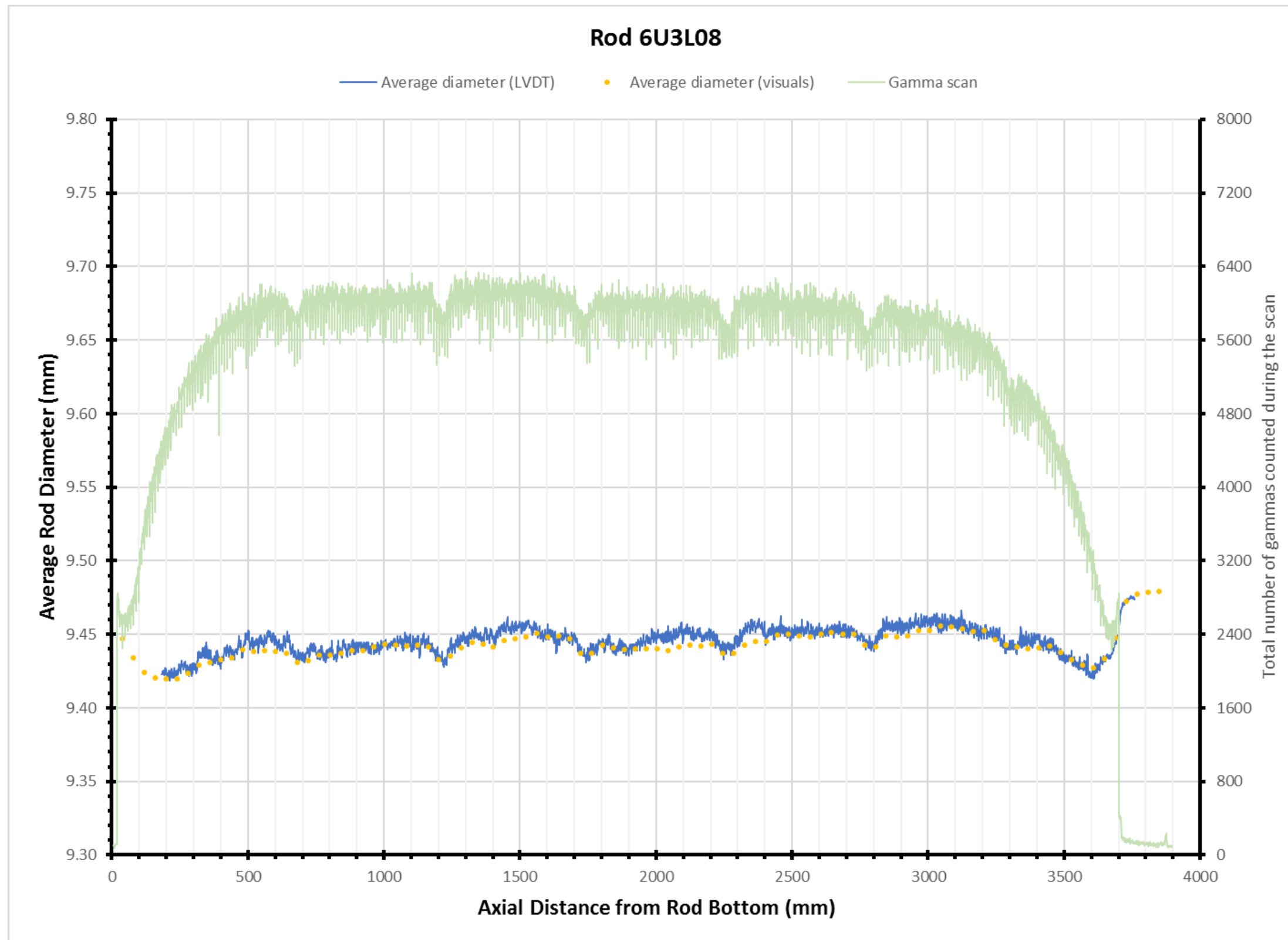


Figure B.14. Rod 6U3L08 LVDT Profilometry, Visual Profilometry, and Gamma Scan Data.

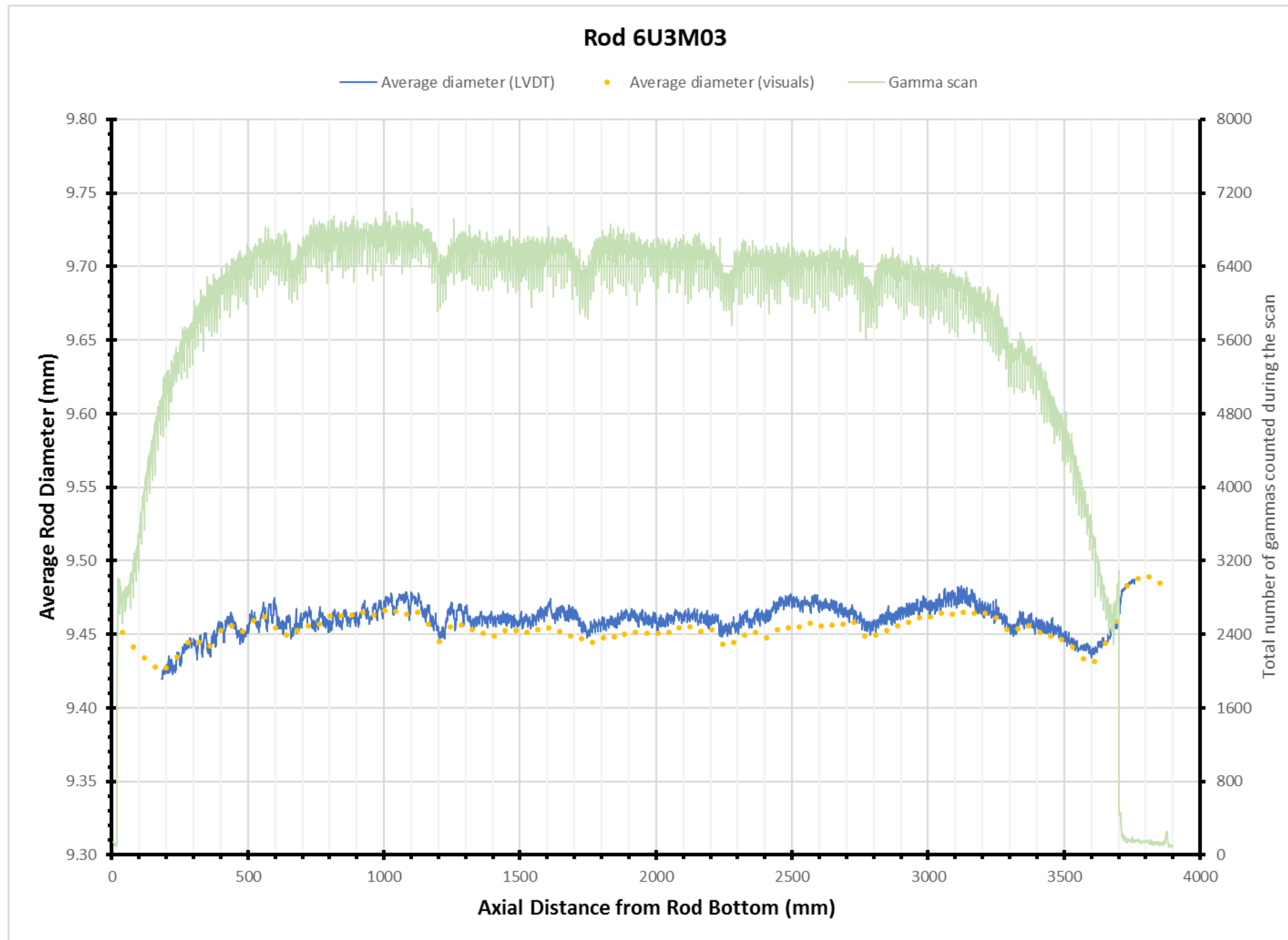


Figure B.15. Rod 6U3M03 LVDT Profilometry, Visual Profilometry, and Gamma Scan Data.

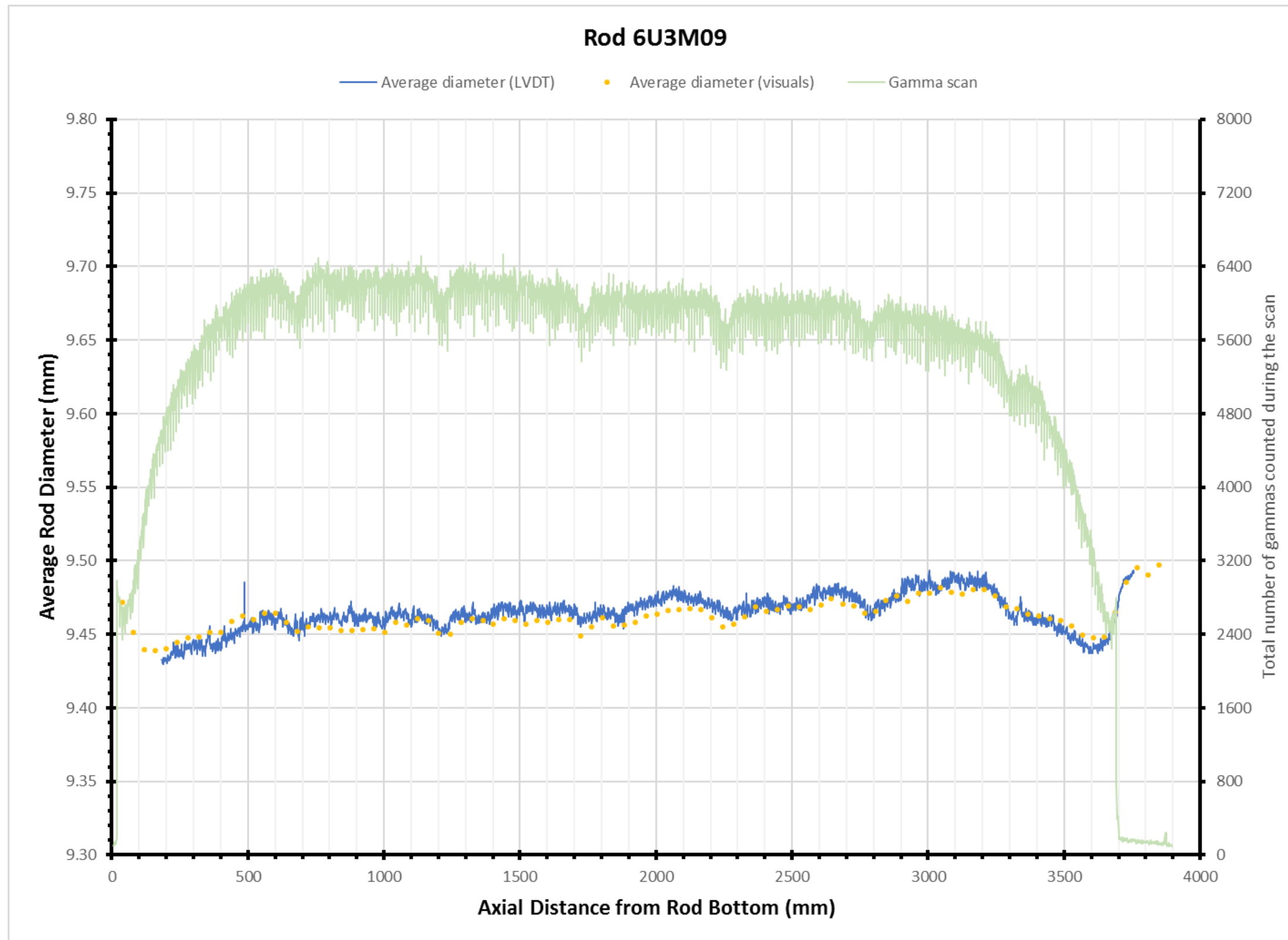


Figure B.16. Rod 6U3M09 LVDT Profilometry, Visual Profilometry, and Gamma Scan Data.

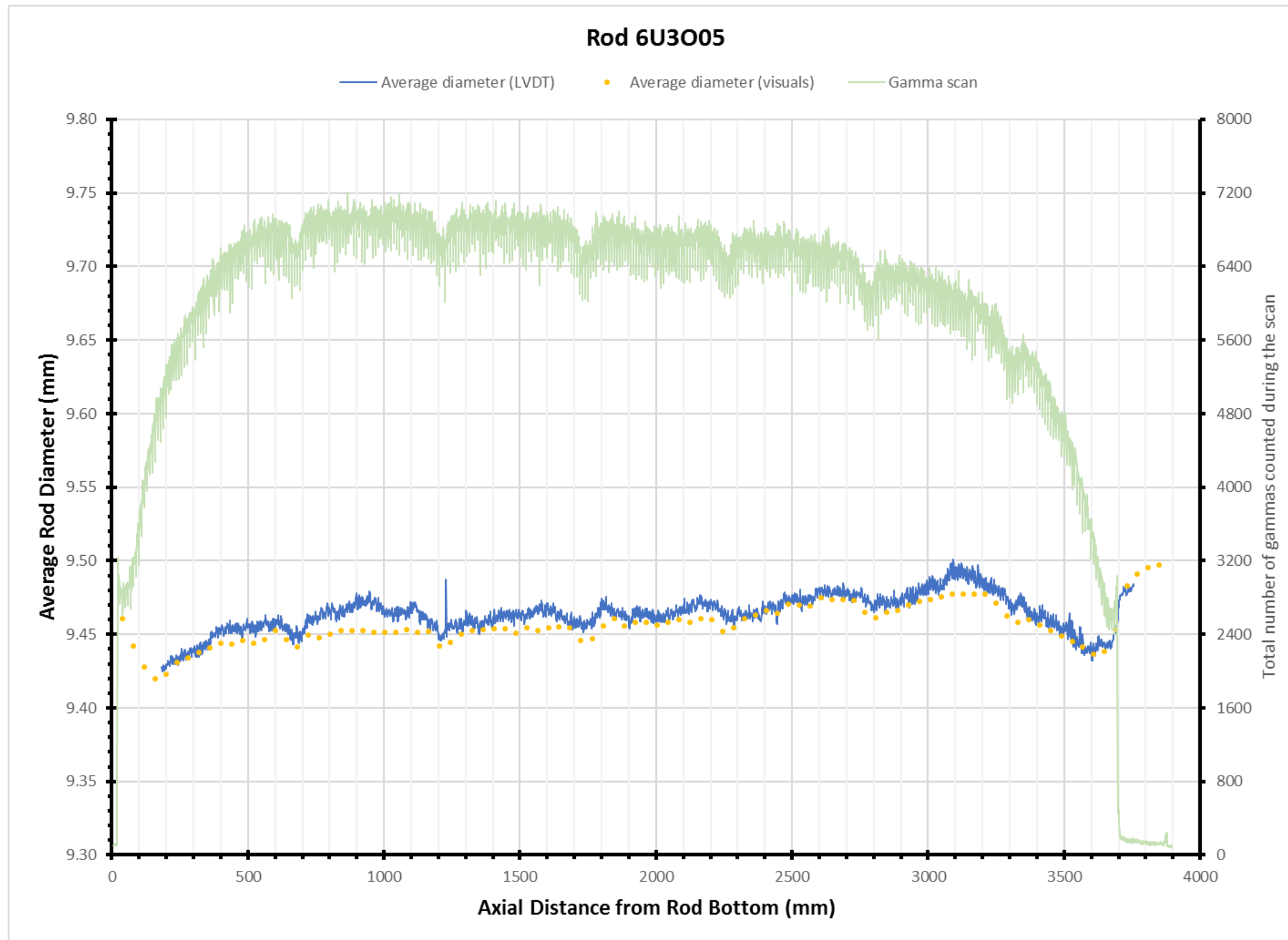


Figure B.17. Rod 6U3005 LVDT Profilometry, Visual Profilometry, and Gamma Scan Data.

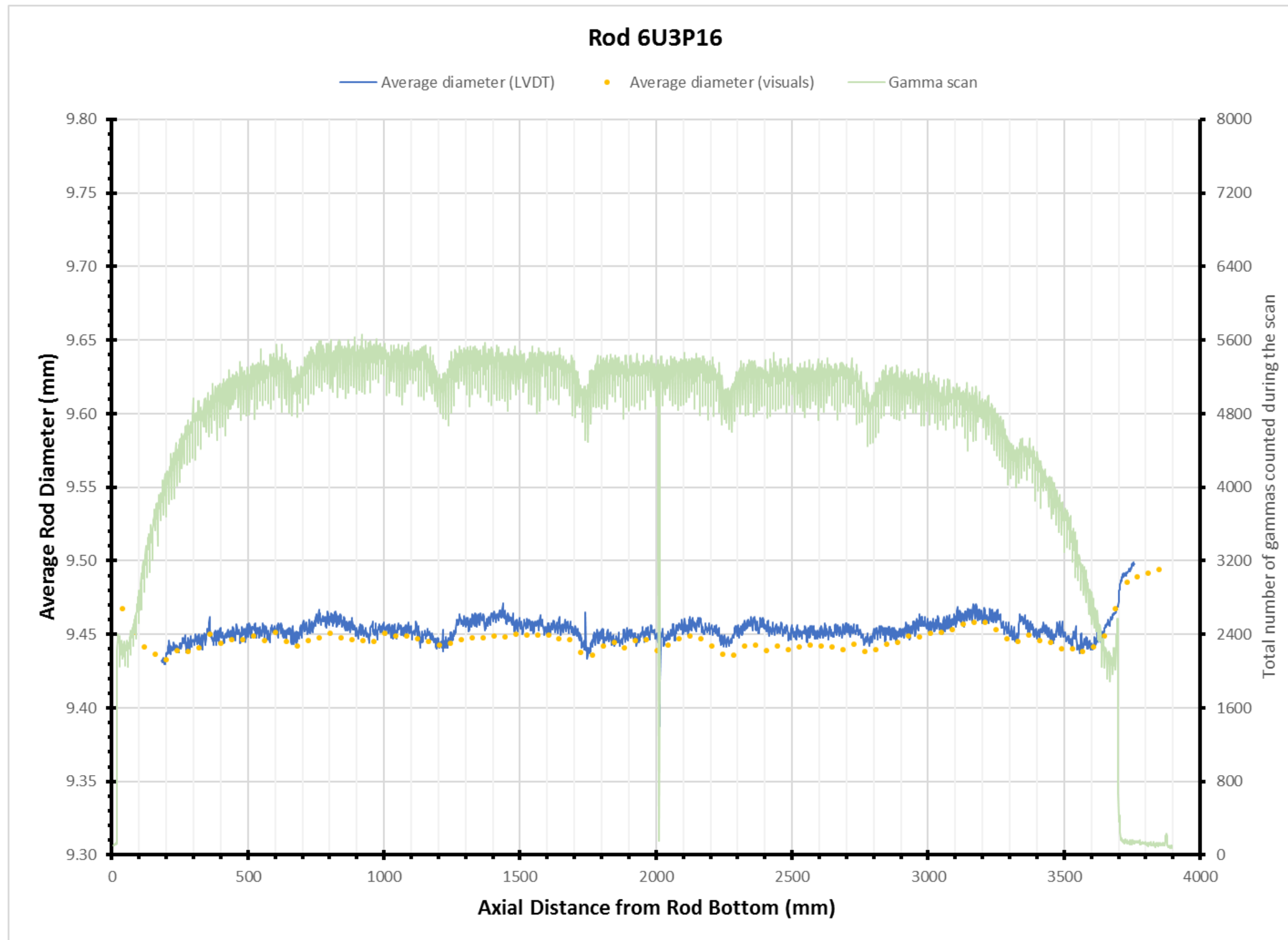


Figure B.18. Rod 6U3P16 LVDT Profilometry, Visual Profilometry, and Gamma Scan Data.

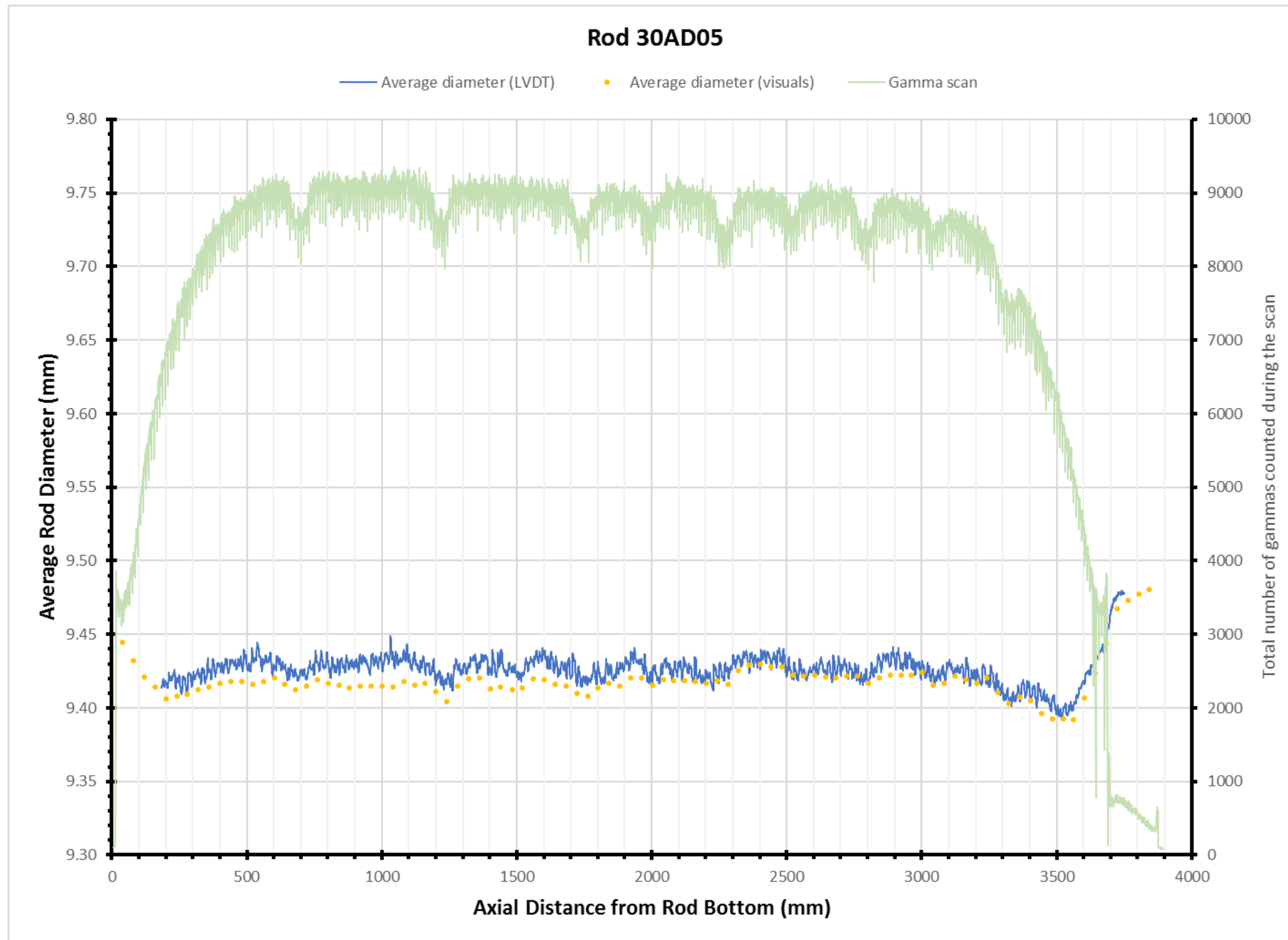


Figure B.19. Rod 30AD05 LVDT Profilometry, Visual Profilometry, and Gamma Scan Data.

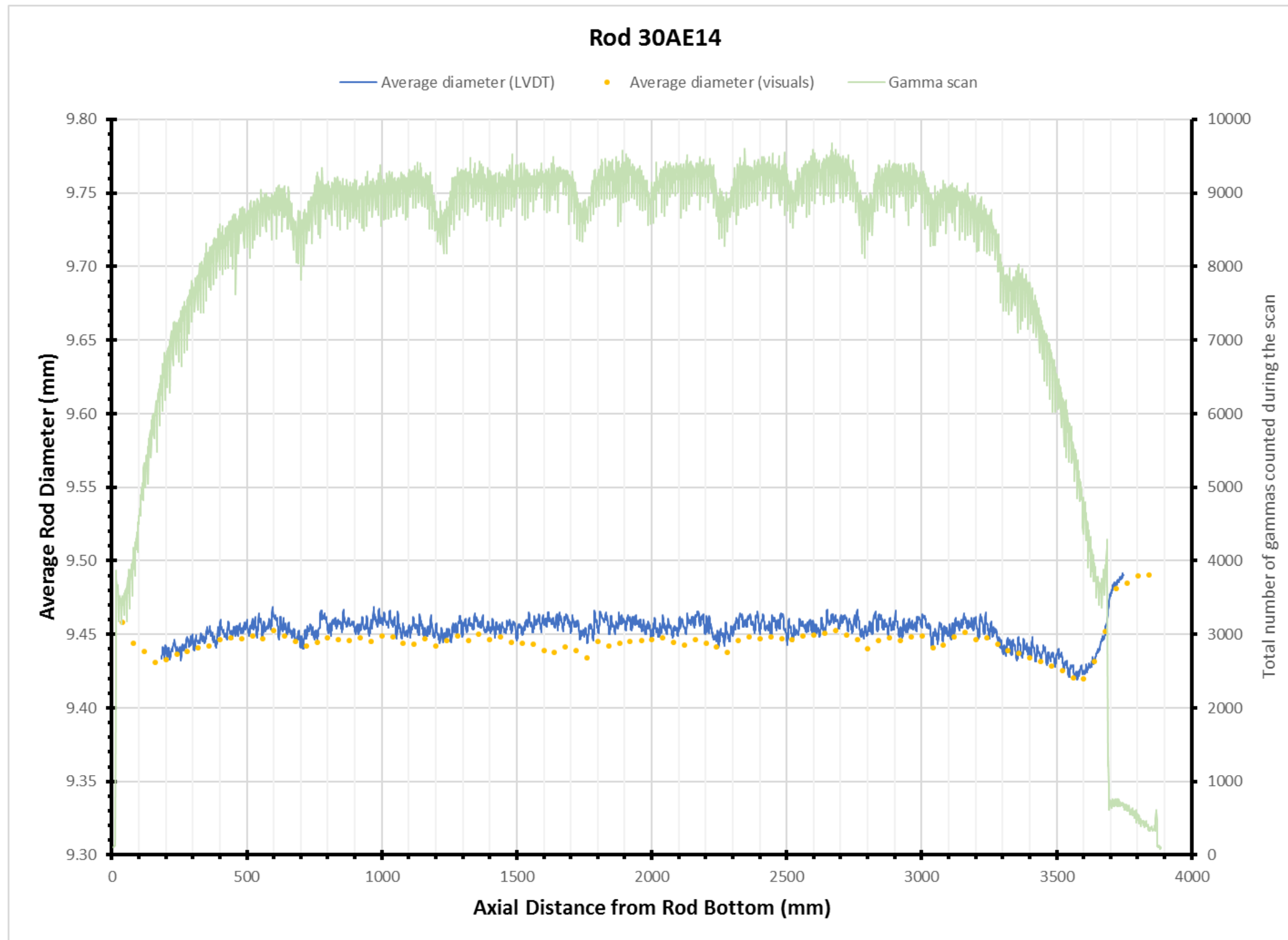


Figure B.20. Rod 30AE14 LVDT Profilometry, Visual Profilometry, and Gamma Scan Data.

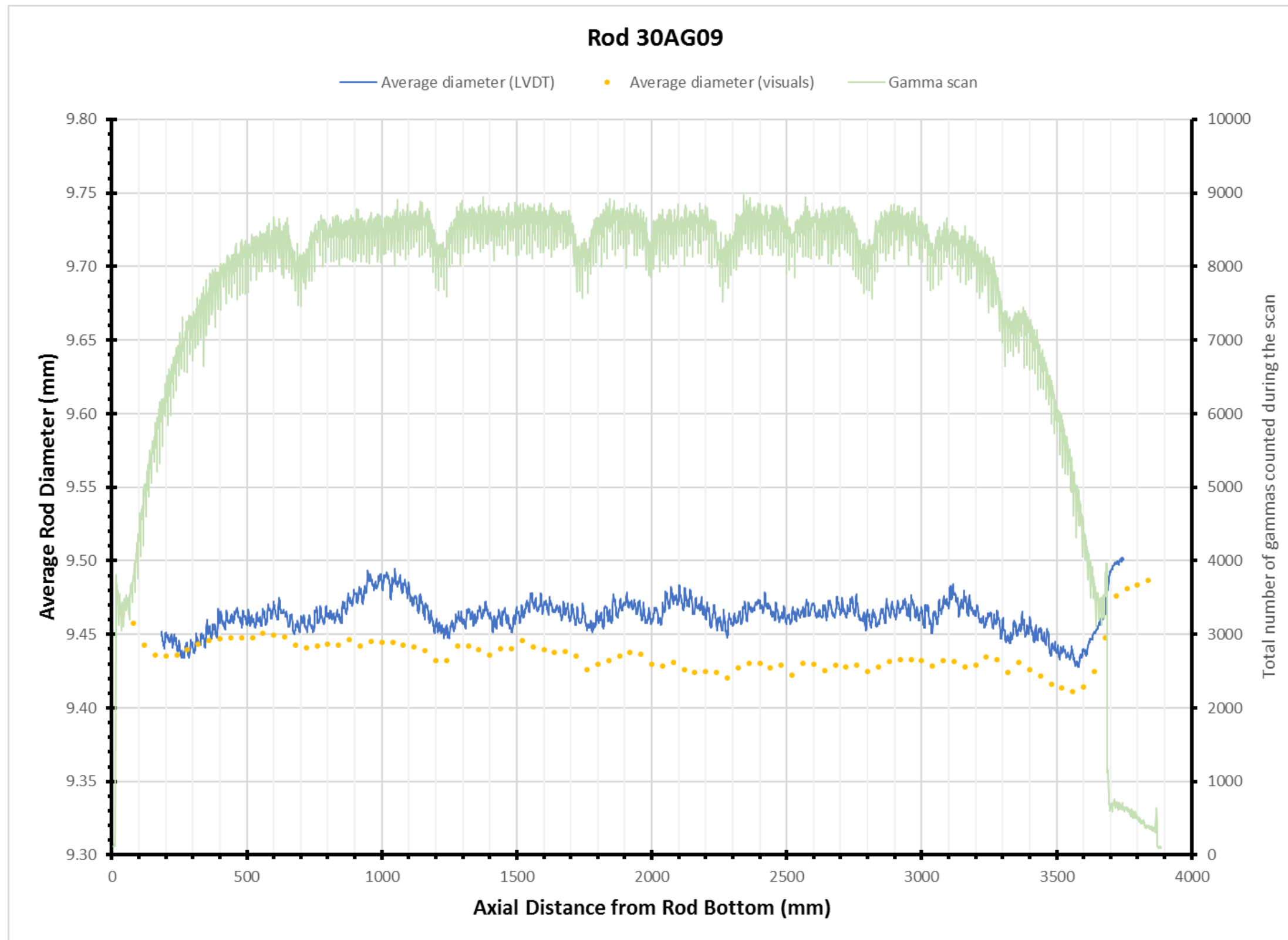


Figure B.21. Rod 30AG09 LVDT Profilometry, Visual Profilometry, and Gamma Scan Data.

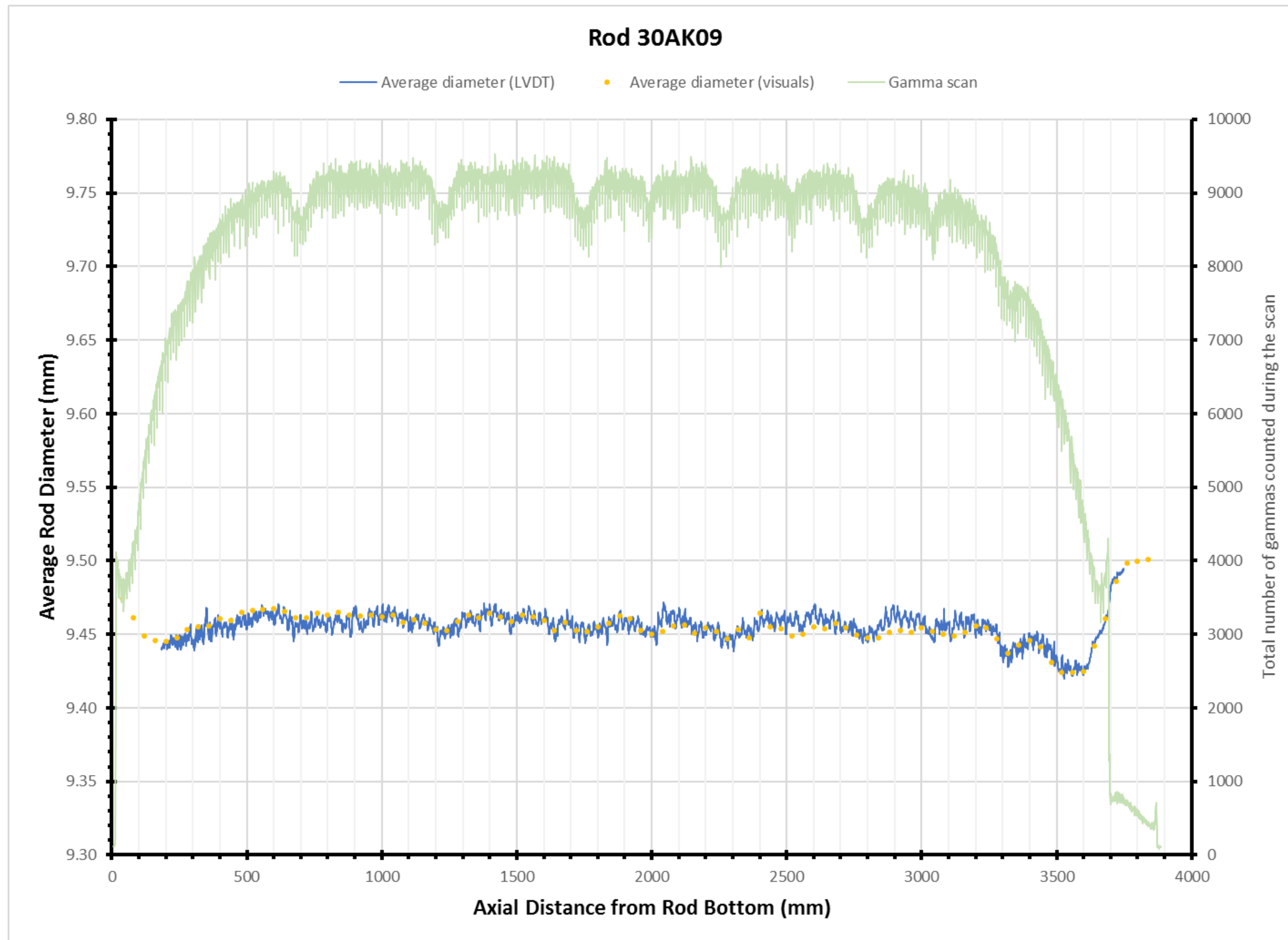


Figure B.22. Rod 30AK09 LVDT Profilometry, Visual Profilometry, and Gamma Scan Data.

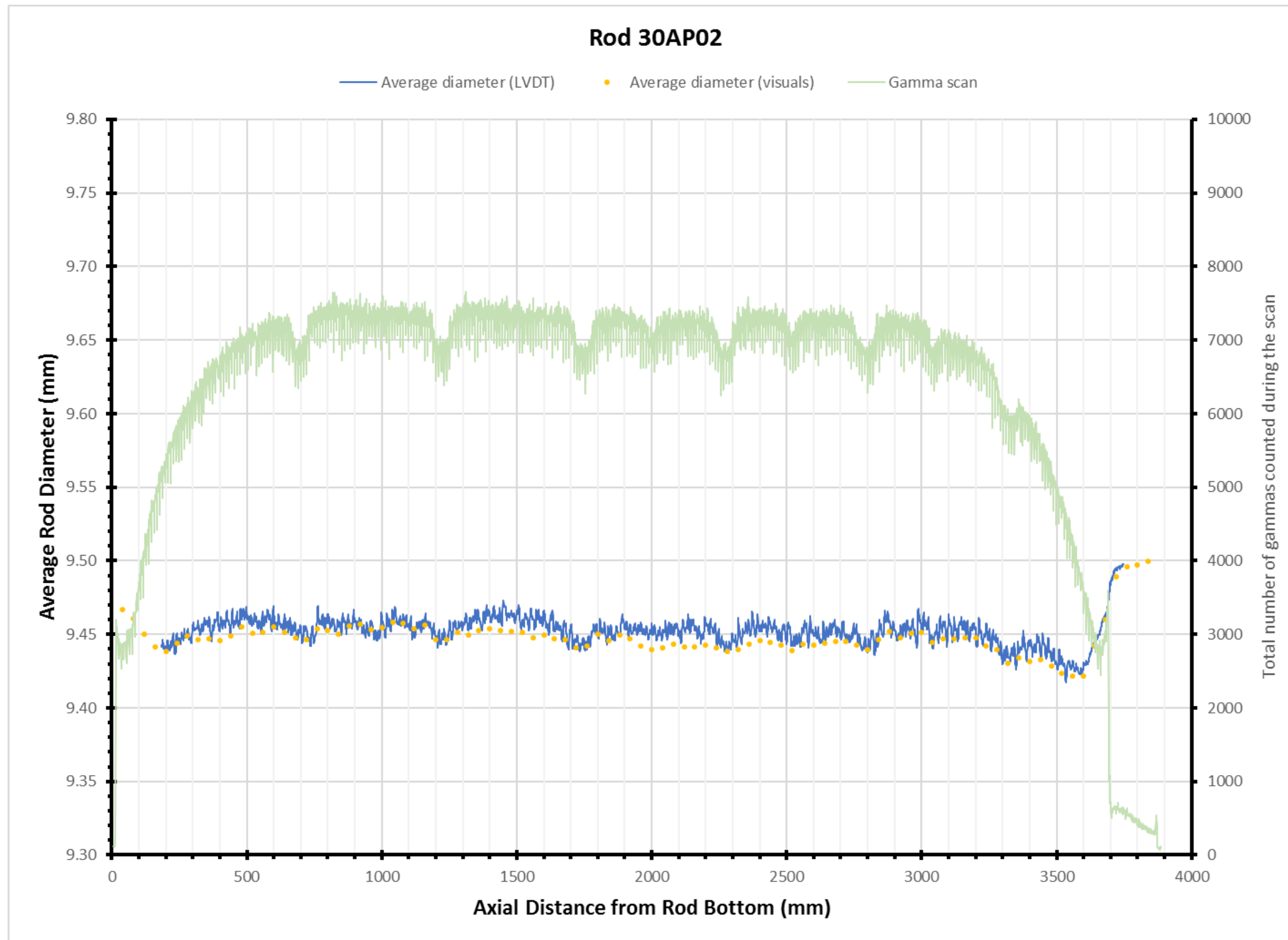


Figure B.23. Rod 30AP02 LVDT Profilometry, Visual Profilometry, and Gamma Scan Data.

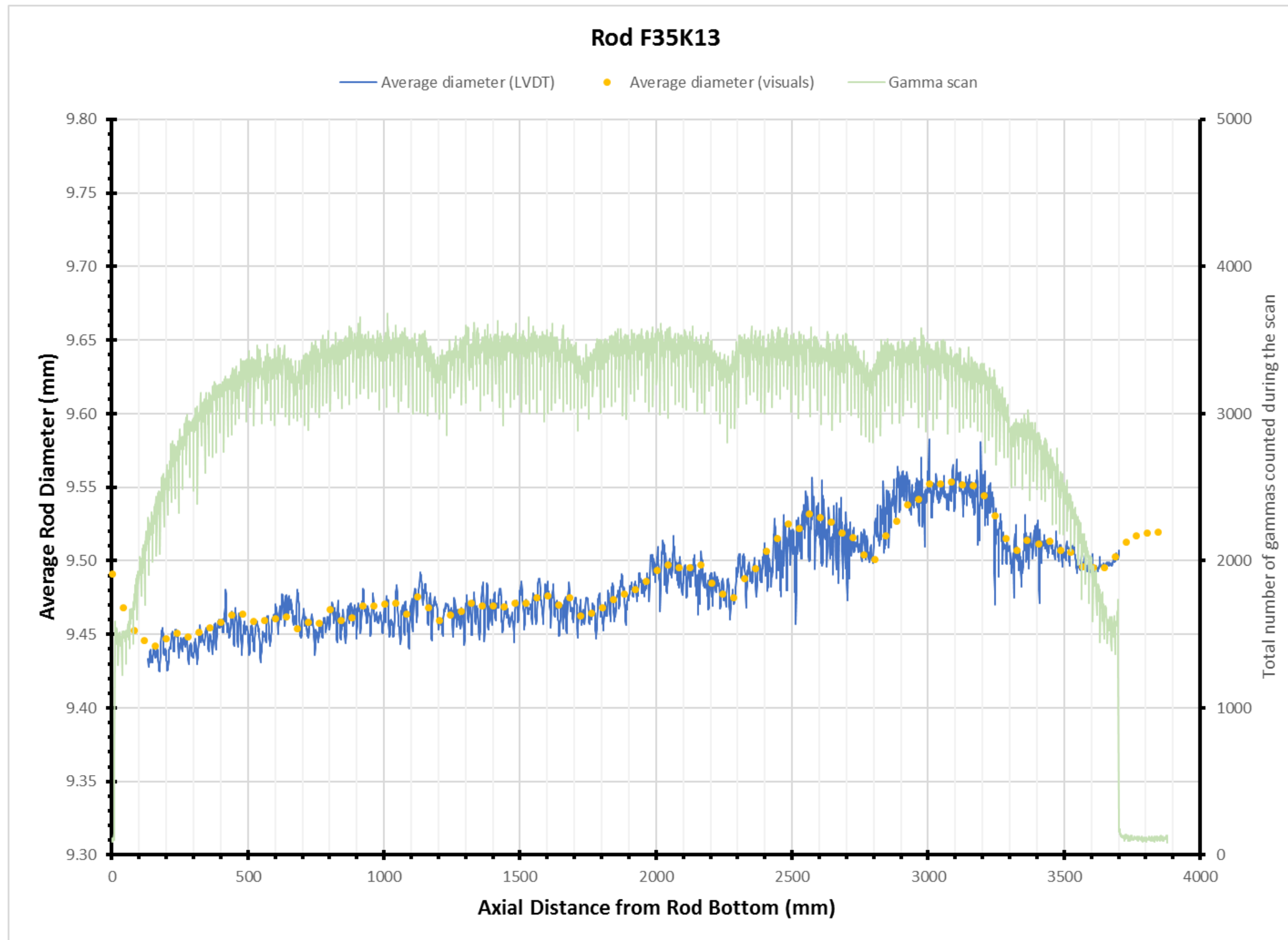


Figure B.24. Rod F35K13 LVDT Profilometry, Visual Profilometry, and Gamma Scan Data.

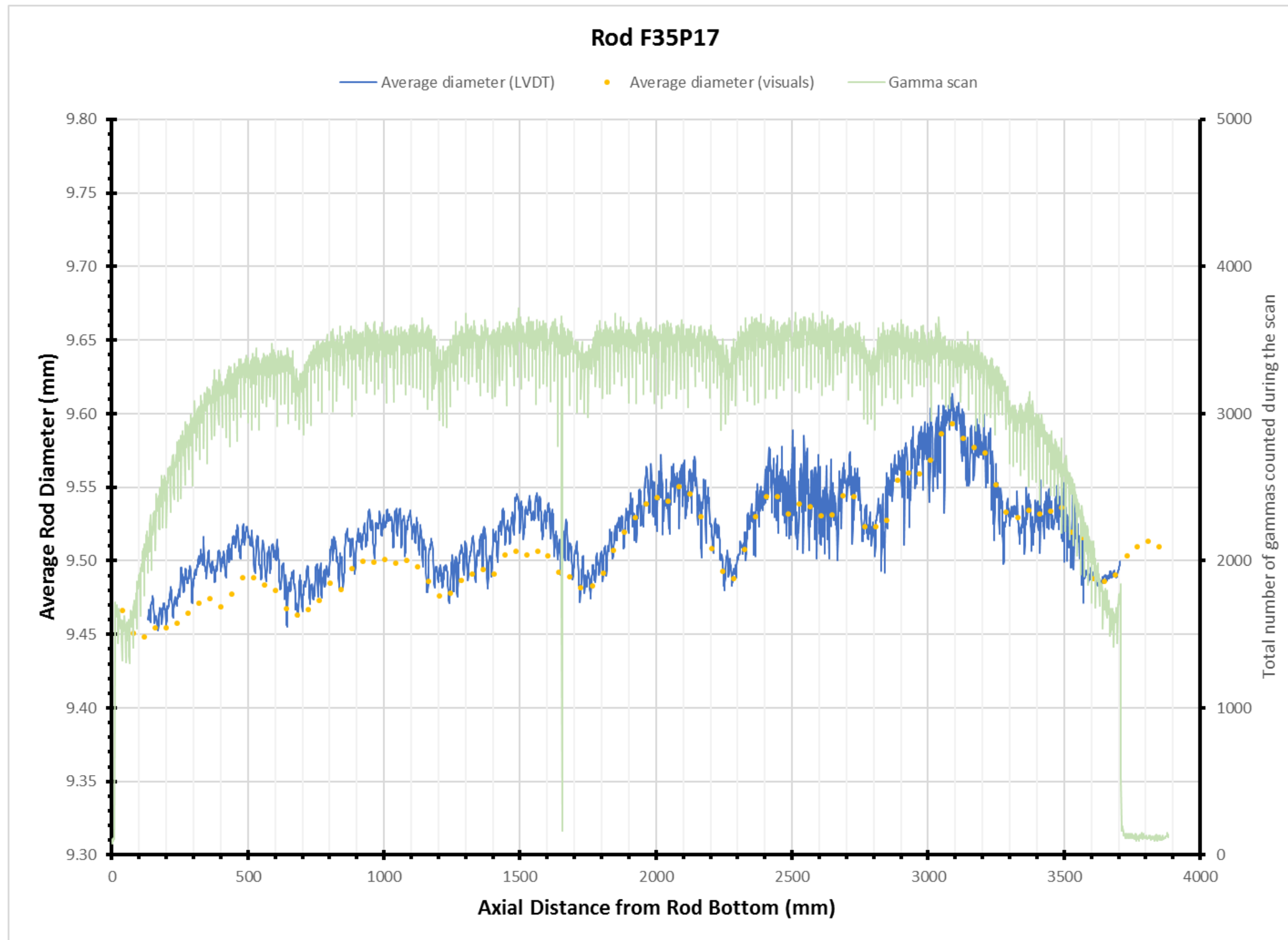


Figure B.25. Rod F35P17 LVDT Profilometry, Visual Profilometry, and Gamma Scan Data.